Modeling of high-frequency coding for single cortical cells and precisely manipulating action-potential timing in vivo

D I S S E R T A T I O N

zur Erlangung des akademischen Grades

Doctor rerum naturalium
(Dr. rer. nat)
im Fach Physik
Spezialisierung: Theoretische Physik
eingereicht an der
Mathematisch-Naturwissenschaftlichen Fakultät
Humboldt-Universität zu Berlin

von

M. Sc. Jens Peter Doose

Präsidentin der Humboldt-Universität zu Berlin:
Prof. Dr.-Ing. Dr. Sabine Kunst

Dekan der Mathematisch-Naturwissenschaftlichen Fakultät:
Prof. Dr. Elmar Kulke

Gutachter:
1.Benjamin Lindner
2.Martin Falcke
3.Fred Wolf
Tag der mündlichen Prüfung: 19.04.2018

Zusammenfassung

Die Kodierung von Signalen und Informationen in neuronalen Systemen basiert auf der Aktivität einzelner Nervenzellen, die, anhand von Sequenzen aus Aktionspotentialen (Pulszügen), miteinander in Wechselwirkung treten. Diese Pulszüge sind somit das zentrale Objekt für die Untersuchung der neuronalen Funktionsweise. Die Erforschung des Einflusses der experimentellen Manipulation solcher Pulszüge auf das Verhalten des Organismus sowie die theoretische Analyse der Eigenschaften mathematischer Neuronenmodelle stellen daher zentrale Aspekte in der aktuellen Forschung dar.

Diese Arbeit beschäftigt sich sowohl mit der experimentell motivierten Fragestellung nach der Kontrolle der Einzelzellaktivität kortikaler Neurone sowie mit der theoretischen Beschreibung der neuronalen Dynamik und ihrer Transfereigenschaften anhand einfacher Neuronenmodelle. Hierfür werden in-vivo Daten, die mit Hilfe der juxtazellulären Stimulation mit weißem bandpass limitiertem Gaußschem Rauschen erhoben wurden, verwendet. Diese Daten werden im Hinblick auf die Verlässlichkeit, mit der Pulszüge hervorgerufen werden können, sowie auf die Transfereigenschaften der einzelnen untersuchten Neuronen analysiert. Mit Parameterfits einfacher Neuronenmodelle werden die experimentell ermittelten Pulszugstatistiken sowie die präzisen Zeitpunkte der einzelnen Aktionspotentiale quantitativ reproduziert.

Diese Untersuchungen zeigen, dass mit dynamischen Rauschstimuli in juxtazellulärer Stimulation verlässlich und reproduzierbar Pulszüge in einzelnen kortikalen Neuronen hervorgerufen werden können. Hierbei ist die Kontrolle über die neuronalen Aktivitätsmuster vergleichbar mit der, die für intrazelluläre Stimulation erreicht wird. Weiterhin offenbart die Analyse der Daten die Eigenschaft der untersuchten Neurone frequenzunabhängig, bishin zu Vielfachen der Feuerrate des Neurons, Information über Signalkomponenten zu transferieren. Diese Eigenschaft steht im Widerspruch zum Verhalten der einfachsten (und populärsten) integrate-and-fire Modelle, die die Zelle ohne Auflösung ihrer räumlichen Struktur näherungsweise beschreiben. Die Erweiterung solcher Ein-Kompartiment Modelle auf ein Zwei-Kompartiment Modell und die damit eingeführte Unterscheidung zwischen Soma und Dendrit ermöglicht es, für einzelne Neuronen sämtliche experimentell erhobenen Statistiken, einschließlich des Hochfrequenz-Transfers, quantitativ zu reproduzieren. Dies zeigt, dass der Einfluss der räumlichen Struktur in einigen Situationen einen wichtigen (strukturellen) Mechanismus mit Einfluss auf die neuronale Dynamik darstellt.

Zusätzlich zu den obigen Untersuchungen wird eine Methode vorgestellt, um, anhand von Input-Output Statistiken konkreter Neurone, Gaußsche Stimuli zu berechnen, die in der jeweiligen Zelle einen vorgeschriebenen Pulszug hervorrufen. In Experimenten und Simulationen wird gezeigt, dass diese vorgeschriebenen Pulszüge mit einer Verlässlichkeit erzeugt werden können, die in etwa der intrinsischen Verlässlichkeit des untersuchten Neurons entspricht. Derartige Methoden ermöglichen neuartige Untersuchungen des Einflusses der Aktivität einzelner Neurone auf das Verhalten des Organismus.

Abstract

In neuronal systems, signals and information are encoded in the activity of individual neurons that interact with each other using sequences of action potentials (spike trains). These spike trains are the fundamental object in the task of examining the functioning of neuronal systems. Thus, a key role in today's neuroscience is to investigate how experimental manipulations of spike trains affect the behavior or state of an organism and to theoretically analyze the properties of neuron models.

This work elaborates on the question to which extent experimental control about the activity of single cortical neurons can be achieved and deals with the theoretical description of the neuronal dynamics and the transfer properties of simple neuron models. To this end, in-vivo data that have been recorded from juxtacellular experiments in cortical neurons under white noise stimulation, are used. These data are analyzed with respect to the reliability and precision with which spike trains can be evoked, and to the transfer properties of the particular neurons under investigation. By means of parameter optimization, simple neuron models are fitted in order to quantitatively reproduce the measured spike train statistics and specific action potential timings.

The analysis reveals that dynamic noise-stimuli can be used in juxtacellular stimulation to reliably generate reproducible spike trains in single cortical neurons. The extent of the control of the neuronal dynamics turns out to be comparable to that observed for intracellular stimulation. The analysis also reveals that the cells show a marked broadband coding of information, up to frequencies that are multiples of the firing rate of the respective neuron. This is in contrast to what is known for the simplest (and most popular) integrate-and-fire models, for which the cellular dynamics are described by a single space-independent variable. The extension of these one-compartment models to two-compartment models introduces a spatially distinction between soma and dendrite and we could show that for particular neurons it is sufficient to quantitatively reproduce all experimentally measured spike-train and input-output statistics, including the high-frequency information-transfer. Therefore, the effect of the spatial structure can be an important (structural) mechanism that can have influence on the neuronal dynamics.

Additionally to the above considerations, by means of input-output statistics of particular neurons, we propose a method to compute Gaussian stimuli that are supposed to evoke prescribed spike trains in the respective neuron. Using experiments and simulations, we show that the prescribed spike trains can be evoked with a reliability that is comparable to the intrinsic reliability of the neuron under investigation. Such methods can open new opportunities in experiments to study the influence of single neuron activity on the state (behavior) of the organism.

Contents

Chapter 1.

Introduction

To gain understanding of the mechanisms that underlie the complex behavior of living systems, it is essential to identify fundamental properties of the functioning of the neuronal tissue. This neuronal tissue mainly consists of the glial cells and neurons that interact via electrical and chemical pathways. For many organisms the functioning of the neurons sets the basis for fast and complex interactions with the environment as well as for higher cognitive abilities.

Modern neuroscience addresses the question how information about the environment is stored and encoded in the structure and the activity of individual neurons and neuronal networks. Therefore, theoretical descriptions of the investigated systems are integral parts of neuroscience to gain understanding of the neuronal dynamics. However, because the complexity of a mathematical analysis increases with the biophysical accuracy of description, a detailed treatment is often not vital. In contrast, certain approximations are applied to replace the biophysical by simplified effective mechanisms. Depending on the level of simplification the resulting equations can be used to investigate the functional importance of certain elements and mechanisms either analytically or numerically. Because the elements of the neuronal system are subject to several sources of uncertainty (e.g. thermal fluctuations or input from the surrounding network) the equations for the deterministic dynamics are often disturbed by so called noise terms that account for this randomness. This leads to a description of the systems in terms of stochastic differential equations. Such (nonlinear) equations can develop a rich diversity of dynamics which is even enlarged by the stochasticity of the system. The development of such equations and their theoretical analysis require both, an insight into biophysical properties of neurons and a profound knowledge of mathematics and simulation methods. Therefore, theoretical neuroscience is a fruitful playground for physicists and mathematicians.

One part of this work will be to find a simple stochastic single-cell neuron-model that is able to reproduce basic information-transmission properties as we have observed in

experiments in vivo.

Besides the theoretical investigations, in order to gain knowledge about the neuronal system, it is essential to develop experimental methods that allow for precise control of neuronal dynamics under physiological conditions. Nowadays, one of these methods, the so called patch clamp technique (Neher and Sakmann, 1976), sets the standard for time dependent measuring and manipulation of membrane voltages and action potentials (APs). Another, comparably new and less widespread technique to manipulate the neuronal dynamics is the juxtacellular stimulation technique (Houweling et al., 2010) that has been derived from the juxtacellular staining-technique (Pinault, 1996). One part of this work will be the analysis of experimental data that have been recorded using the juxtacellular technique and to propose a method to design stimuli in order to impose a predefined activity pattern (sequence of APs) on individual neurons.

All experiments that are analyzed in this work have been performed by Guy Doron[1] in the motor- and sensory cortices of anesthetized rats in vivo.

1.1. Thesis outline

This work is structured as follows: The remaining part of this chapter will briefly sketch the biophysical underpinnings that are most important for the investigated neuronal dynamics. Then, the class of neuron models that is used in this work will be introduced and important statistical measures and mathematical backgrounds are recalled. Finally, the juxtacellular stimulation technique that served Guy Doron to record the data is introduced briefly.

The second chapter contains the data analysis of juxtacellular recordings. The issue of spike extraction despite the background of superimposed large voltage fluctuations that arise from the juxtacellular stimulation is addressed. As in Houweling et al. (2010), we show that by juxtacellular stimulation control about the average firing rate can be achieved. We extend the firing-rate control substantially by the control of the precise timing of action potentials. We then present a data analysis that reveals the ability of the neurons to exhibit a sustained support of signal coding/transfer up to high frequencies (several firing rates).

In the third chapter, we introduce the two-compartment integrate-and-fire model and investigate its response properties to high-frequency inputs. We perform a parameter optimization to quantitatively reproduce the experimental statistics and show that the two-compartment model approximates the real neuron sufficiently well to account for the

[1]Guy Doron, NeuroCure Cluster of Excellence, Humboldt Universität zu Berlin, 10117 Berlin, Germany guy.doron@charite.de

statistics that we observed in experiments. In comparison to a one-compartment model, the two-compartment model outperforms the former in quantitatively reproducing the experimental results. In particular, we show that the presence of a dendritic compartment shapes the information-transfer characteristics from lowpass to bandpass.

In chapter four, we present a method to estimate a colored bandpass-limited Gaussian stimulus to reliably evoke prescribed spike trains in specific neurons. We demonstrate the success of this method in numerical simulations as well as in experiments.

Some of the results of this thesis are published in Doose et al. (2016) and Doose and Lindner (2017).

1.2. Neurophysiological backgrounds – Mathematical description of neurons

In this thesis, the object of investigation will be the single (pyramidal) neuron. Therefore, a brief introduction on its structure and basic properties is presented here.

Neurons are specialized cells that are able to transmit electric signals by altering their membrane potential due to the opening and closing of membrane proteins which mediate the flux of specific ions across the membrane. These membrane-potential dynamics are believed to be the carrier of information in the neuronal system and are the quantity that we want to study by mathematical neuron models.

Depending on their particular shape and purpose several types of neurons (e.g. pyramidal cells, Purkinje cells, interneurons) are distinguished. In Fig.1.1, the reconstruction of a pyramidal neuron is given. By means of this simplistic image, we can see that the neuron has several structurally (blue) and functionally (red) separated regions. In vivo a neuron is connected to many other neurons via synaptic connections. Some of these neurons (the postsynaptic neurons) receive its output while others (the presynaptic neurons) give input to this cell. The flow of a signal is therefore unidirectional and typically migrates across the neuron as follows: i) From the terminals of the dendritic tree (tuft, apical and basal dendrite) the synaptic input from the presynaptic neurons is conducted into the soma. Depending on the type of the synapses a dendritic input can be excitatory or inhibitory, which results in either more depolarized or more hyperpolarized membrane potential. ii) In the soma all the inputs are integrated and iii) cause a change of the membrane voltage in the axon initial segment (AIS). When the summed dendritic input is large enough, voltage-dependent ion channels in the AIS are activated and lead to an active avalanche like process that creates a stereotype membrane-potential pulse, the so called action po-

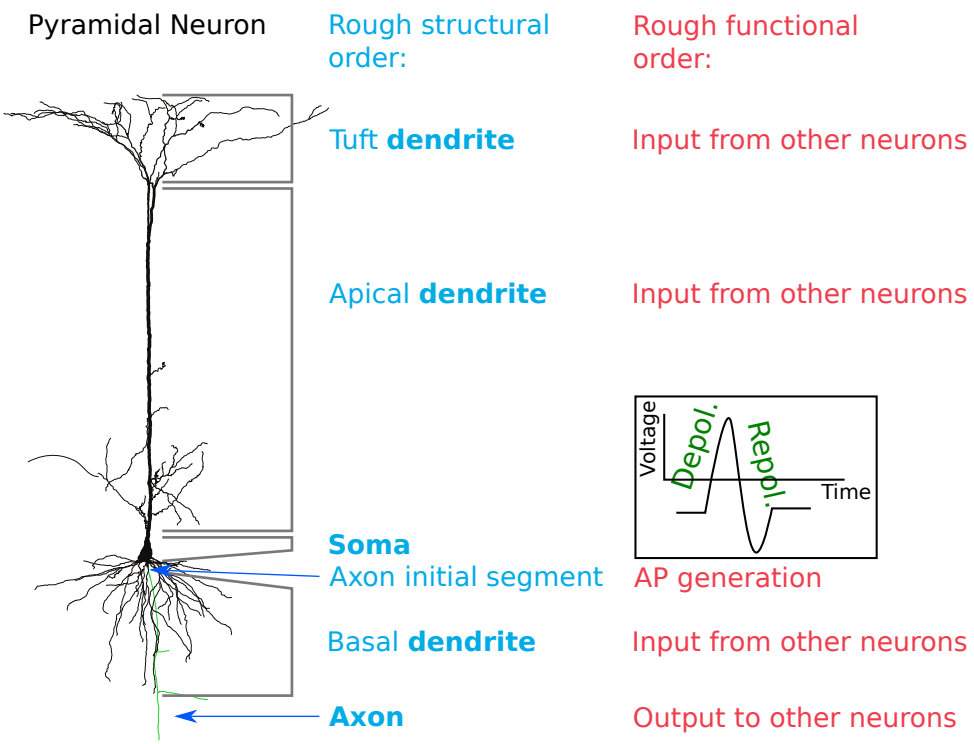

Figure 1.1.: Reconstruction of a pyramidal neuron with structural and functional components. Main structural components (blue text) are the dendrites, soma and axon (green in the reconstructed neuron). Main functional components (red text) are: receiving input (dendrites), creating action potentials (AIS) passing output to other neurons (axon). The inset sketches the time course of an AP as it travels along the axon. The reconstructed neuron was taken and adapted from Larkum et al. (2001), with permission from the Copyright Clearance Center of the *The Journal of Physiology*.

tential (AP, spike) (see inset in Fig.1.1). iv) From the AIS, action potentials propagate as a self sustained traveling wave along the axon (green in the reconstruction) to the synapses. There, they trigger the release of neurotransmitters into the extracellular space (synaptic cleft) which in turn leads to the opening of membrane channels in the membrane of postsynaptic neurons.

For a detailed description of the mechanisms that are involved in AP generation and synaptic communication see e.g. textbooks as Gerstner et al. (2014).

When thinking of the neuron as transmitter and processor of information, one can ask how the information is encoded in the neuronal activity. As described above, the input to other neurons is determined by APs that travel along the axon and trigger the release of neurotransmitters at the synapse. In particular, minor membrane potential fluctuations, that do not lead to AP generation, do not cause such a release and thus are not transmitted to other neurons. Therefore, information that is interchanged with other neurons cannot be encoded in these subthreshold fluctuations, but has to be stored in the sequence of APs. Because the APs itself have a stereotype shape, it is believed that the information is stored solely in the series of times at which the APs appear (the so called spike train).

When modeling the neuronal voltage dynamics, an important task is the balance between simplification of the model and its ability to capture essential features of the dynamics. In order to investigate information transmission and spike-train statistics it is vital to develop neuron models that replace many of the biophysical details, that lead e.g. to the specific shape of the AP, by effective quantities and focus on the description of the timing of APs.

Compartmentalisation For a mathematical description of the membrane voltage, one way to approximate the spatial structure of the neuron is to approximate the neuron as a chain of compartments that are electrically coupled to each other (see e.g. (Dayan and Abbott, 2001; Ermentrout and Terman, 2010; Gerstner et al., 2014)). This approach is like a rasterization of the neuron and the number of compartments that are used to represent a certain part of the neuron defines the resolution of the spatial structure. Therefore, the more compartments are chosen to describe the neuron, the more of the particular shape is taken into account. However, the mathematical description is more simple for less compartments. The most simple description in terms of spatial resolution is a one-compartment model, which is equivalent to neglecting the spatial structure at all. This simplification summarizes all functional components into one single compartment. Thus, all functional properties illustrated in Fig.1.1 are merged into one point in space. However, it is a priori not clear whether the spatial extension and geometry of the neuron itself has

a functional influence that is neglected due to this approximation.

In this thesis, we address the question of structural functionality and demonstrate in particular that the one-compartment model fails to capture some essential features of the neuronal dynamics that indeed can be captured by a two-compartment model. The two-compartment model is the most simple approximation that still takes the neuronal structure into account. Here, typically one compartment is active and has a mechanism for AP generation (referred to as somatic compartment), while the other one is passive (referred to as dendritic compartment) and receives input from the surrounding network.

Integrate-and-fire mechanism Besides the different levels of describing the spatial structure, also the functioning of the membrane itself can be handled in different ways. The electric properties of the membrane are mainly influenced by the membrane capacitance and the dynamics of the ion channels in the membrane.

A common description to approximate the effect of the membrane-channel dynamics on the membrane voltage is given in the framework of integrate-and-fire models. Within this framework the membrane-channel dynamics that leads to the ion flux across the membrane of one compartment are not explicitly modeled, but are described by effective expressions. The canonical equations for a one-compartment integrate-and-fire model with effectively treated channel dynamics are

$$C\frac{\mathrm{d}V}{\mathrm{d}t} = f(V) + I(t), \tag{1.1}$$

$$\text{If } V(t) > V_{\mathrm{Th}} : V(t + \mathrm{d}t) \to V_{\mathrm{reset}}. \tag{1.2}$$

Here, C represents the membrane capacitance of this compartment and $I(t)$ is some input current (synaptic input or external stimulation). The second line (eq.(1.2)) describes a fire-and-reset mechanism: Whenever the voltage reaches a certain value (V_{Th}) a spike time is recorded and the voltage is set to a reset value (V_{reset}). Together with this fire-and-reset mechanism the function $f(V)$ describes the effects of the ion channel dynamics. Depending on the particular form of $f(V)$ different model types are distinguished. Three standard examples for $f(V)$ are:

- $f(V) = 0$: The perfect integrate-and-fire (PIF) model (Lapicque, 1907; Gerstein and Mandelbrot, 1964) — only the reset mechanism is taken into account, no additional channel dynamics are described. The input currents are integrated until the threshold is reached and the reset is applied.

- $f(V) = -g_l(V - E_l)$: The leaky integrate-and-fire (LIF) model (Stein, 1965; Johan-

nesma, 1968; Knight, 1972) — g_l and E_l describe the membrane leak conductance and the reversal potential. Still the input is integrated, but the subthreshold dynamic is extended by the effect of a leaky membrane. Current leaks out of the compartment and (without input) the voltage decays to E_l.

- $f(V) = -g_l(V - E_l) + g_l\Delta e^{\frac{V-\bar{V}}{\Delta}}$: The exponential integrate-and-fire (EIF) model (Fourcaud-Trocmé et al., 2003) — The subthreshold dynamic is similar to the LIF, but the AP onset is mimicked by an exponential current influx that starts to dominate the dynamic when the voltage becomes larger than a soft threshold ($V > \bar{V}$). This term is supposed to account for the avalanche like activation of voltage dependent sodium channels which are responsible for spike-activation. The exponential dependence of the current on the membrane voltage agrees well with the corresponding experimentally measured inward current (Badel et al., 2008). The sharpness of the onset of this influx is given by the spike slope factor Δ.

Noise in the nervous system As described above, in vivo a neuron receives synaptic input from its presynaptic environment. Because in a mathematical description of a single neuron the activity of the presynaptic neurons is not part of the model, the synaptic input has to be treated by an effective term. The way this is usually done is to include a stochastic process, the so called *synaptic noise*, into the dynamic. This stochasticity has its origin in the incomplete description of the system.

A second source of stochasticity arises from thermal fluctuations of the membrane proteins. These fluctuations lead to random changes in the conformation of the ion channels and thus cause a stochastic opening and closing which leads to fluctuations in the membrane voltage. This causes a real randomness that does not contain any (unknown) signal.

For a neuron that is embedded in the neural network in vivo, both noise sources are present, but likely the former exceeds the latter. In this work, we will use stochastic neuron models with the exponential integrate-and-fire mechanism, both without (one compartment) and with (two compartments) consideration of the spatial structure of the neuron.

1.3. Important measures

In the following, statistical measures that will be used in this work are introduced.

Fourier transform We will denote the Fourier transform of a variable $x(t)$ as $\mathcal{F}(x)$ or $\tilde{x}(f)$. The transformation is defined as

$$\tilde{x}(f) = \mathcal{F}(x) = \int_0^T e^{2\pi i f t} x(t)\,\mathrm{d}t. \tag{1.3}$$

Spike train $x(t)$ Using the fire-and-reset mechanism in neuron models makes it straightforward to define the times of the APs as the times when the reset is applied. For the response of a real neuron typically a threshold is defined and each time instance in which the membrane voltage crosses this threshold from below is taken as time of the AP. This also defines a set of spike times t_i, where i is the i-th AP that characterizes the neurons activity. These spike times are used to define the spike train $x(t)$:

$$x(t) = \sum_{i=1}^{N} \delta(t - t_i). \tag{1.4}$$

Defined in this way, each AP is represented by a δ-peak with unity weight.

Instantaneous firing rate $r(t)$ The instantaneous firing rate of an ensemble of spike trains is given by

$$r(t) = \langle x(t) \rangle\,, \tag{1.5}$$

where $\langle\cdot\rangle$ denotes ensemble average.

Mean firing rate r_0 A basic property of the instantaneous firing rate is its time average, the mean firing rate

$$r_0 = \lim_{T\to\infty} \frac{1}{T} \int_0^T r(t)\,\mathrm{d}t = \lim_{T\to\infty} \frac{N(T)}{T}. \tag{1.6}$$

This is the number of spikes, $N(T)$, that appear within a time window of size T divided by T.

Coefficient of variation C_V The coefficient of variation (CV) of a spike train characterizes the variability of the length of intervals between consecutive spikes (inter spike

intervals [ISI])

$$C_V = \frac{\sqrt{\mathrm{var}(t_{i+1} - t_i)}}{\mathrm{mean}(t_{i+1} - t_i)}. \tag{1.7}$$

The smaller the CV the more regular (pacemaker-like) is the spike train. The larger the CV the more irregular is the spike train (a mixture of long and short ISIs). The CV of a homogeneous Poisson process equals 1.

Power spectrum $S_{xx}(f)$ The power spectrum is a frequency-resolved measure that quantifies the amount of power that a function has in a particular frequency band. It is defined as

$$S_{xx}(f) = \frac{1}{T} \langle \tilde{x}^* \tilde{x} \rangle \,. \tag{1.8}$$

Here, * denotes complex conjugation and $\langle \cdot \rangle$ denotes the ensemble average over all spike trains x. For a spike train the power spectrum does not decay as frequency goes to infinity but saturates at the firing rate $\lim_{f\to\infty} S_{xx}(f) = r_0$, which is due to the δ-peaks in the definition of the spike train (Cox and Lewis, 1966).

Cross-correlation $C_{x_i x_j}(\tau)$ and cross-spectrum $S_{x_i x_j}(f)$ The cross-correlation between spike trains is defined as

$$C_{x_i x_j}(\tau) = \langle (x_i(t) - \langle x_i \rangle)(x_j(t+\tau) - \langle x_j \rangle) \rangle_{i \neq j} \,. \tag{1.9}$$

Here, the outer average runs over all distinct spike trains while the inner average is the mean value of the particular spike train (firing rate). To get an intuition about this quantity, its relation to the *conditional* probability of having spikes in different spike trains is calculated in the following.

With the assumption that $\langle x_i \rangle = \langle x_j \rangle = r_0$ eq.(1.9) becomes

$$C_{x_i x_j}(\tau) = \langle x_i(t) x_j(t+\tau) \rangle_{i \neq j} - r_0^2. \tag{1.10}$$

For a set of spike trains, one can calculate the *joint* probability of having a spike in one spike train in a time window of size $\mathrm{d}t$ and a spike in another spike train in a time window of the same size shifted by τ

$$P\,(\text{spike in train } i,\ \text{spike in train } j \text{ shifted by } \tau) = \langle x_i(t) x_j(t+\tau) \rangle_{i \neq j}\, \mathrm{d}t^2. \tag{1.11}$$

Using eq.(1.9) this is related to the cross-correlation according to

$$P\left(\text{spike in train } i,\ \text{spike in train } j \text{ shifted by } \tau\right) = \left(C_{x_i x_j}(\tau) + r_0^2\right) \mathrm{d}t^2. \tag{1.12}$$

For independent spike trains ($C_{x_i x_j}(\tau) = 0$) this would just be the probability due to chance $P_{\text{chance}} = r_0^2\, \mathrm{d}t^2$. The *conditional* probability of having two spikes in different spike trains appearing at times separated by τ is given by

$$P(\tau) = \frac{P\left(\text{spike in one train},\ \text{spike in another train shifted by } \tau\right)}{P\left(\text{spike in any spike train}\right)} \tag{1.13}$$

$$= \left(\frac{C_{x_i x_j}(\tau)}{r_0} + r_0\right) \mathrm{d}t. \tag{1.14}$$

Thus, e.g. $C_{x_i x_j}(0)$ determines the probability of having synchronous spikes in different spike trains.

According to the Wiener-Khinchin theorem the Fourier transform of the correlation function yields the corresponding cross-spectrum $S_{x_i x_j}(f) = \mathcal{F}(C_{x_i x_j})$. With the convolution theorem this results in

$$S_{x_i x_j}(f) = \frac{1}{T} \left\langle \tilde{x}_i^* \tilde{x}_j \right\rangle_{i \neq j}. \tag{1.15}$$

Cross-correlation $C_{sx}(\tau)$ and cross-spectrum $S_{sx}(f)$ Analogue to the definition of the cross-correlation and cross-spectrum between spike trains one can define a cross-correlation and cross-spectrum between input stimulus $I_s(t)$ and output spike train $x(t)$.

$$C_{sx}(\tau) = \left\langle (I_s(t) - \langle I_s \rangle)(x(t+\tau) - \langle x \rangle) \right\rangle, \tag{1.16}$$

$$S_{sx}(f) = \frac{1}{T} \left\langle \tilde{I}_s^* \tilde{x} \right\rangle. \tag{1.17}$$

Again both quantities are related to each other via Fourier transform $S_{sx}(f) = \mathcal{F}(C_{sx})$. The cross-correlation (spectrum) between input $I_s(t)$ and output $x(t)$ characterizes the linear properties of the system. The cross-spectrum is related to the frequency-response amplitude $\tilde{\chi}(f)$ (also known as susceptibility) according to

$$\tilde{\chi}(f) = \frac{S_{sx}(f)}{S_{ss}(f)}. \tag{1.18}$$

Thus, for an input with flat power spectrum $S_{ss}(f) = \text{const}$ the susceptibility and the cross-spectrum only differ by a scaling factor. The strength of the systems response to a

single signal component at frequency f is characterized by $|\tilde{\chi}(f)|$.

Vector strength $\mathbf{r}(f)$ Another way to quantify the neuronal response to a harmonic driving force in a frequency-resolved way is the vector strength $\boldsymbol{r}(f)$ (Goldberg and Brown, 1969)

$$\boldsymbol{r}(f_s) = \left\langle \frac{1}{N} \sum_{j=1}^{N} e^{2\pi i f_s t_j} \right\rangle_{\text{trials}} . \tag{1.19}$$

Here, t_j are spike times and f_s is the frequency of the harmonic stimulus that is used to elicit the t_j. The average runs over different trials, i.e. repetitive representations of the harmonic stimulus. The vector strength has a natural geometric interpretation: Each spike time t_j is represented in the complex plane by a vector with unit length and phase $2\pi f_s t_j$. The vector strength, $\boldsymbol{r}(f_s)$, is the average over these unit vectors. If the phase of all vectors is randomly distributed the vector strength averages to zero, while for spike times that are perfectly locked on the stimulus each vector will have the same phase and the vector strength approaches its maximal value $|\boldsymbol{r}(f)| = 1$.

It can be shown that the vector strength is directly related to the cross-spectrum $S_{sx}(f)$. To this end, the Fourier transform of a spike train is expressed as

$$\tilde{x}(f) = \sum_{j=1}^{N} e^{i2\pi f t_j}. \tag{1.20}$$

Inserting eq.(1.20) into eq.(1.17) gives

$$S_{xs}(f) = \frac{1}{T} \left\langle \tilde{I}_s^*(f) \sum_{j=1}^{N} e^{i2\pi f t_j} \right\rangle. \tag{1.21}$$

For a harmonic stimulus of the form $I_s(t) = I_0 + I_1 \cos(2\pi f_s t)$ the complex conjugated Fourier transform reads $\tilde{I}_s^*(f) = I_0\delta(f) + 0.5I_1\left(\delta(f - f_s) + \delta(f + f_s)\right)$ which reduces to $\tilde{I}_s^*(f) = 0.5I_1\delta(f - f_s)$ when we restrict ourself to the domain of positive frequencies. Therefore, the stimulus–spike-train cross-spectrum is given by

$$S_{xs}(f) = \delta(f_s - f)\frac{I_1}{2T} \left\langle \sum_{j=1}^{N} e^{i2\pi f t_j} \right\rangle \tag{1.22}$$

$$= \delta(f_s - f)\frac{I_1 r_0}{2}\mathbf{r}(f_s). \tag{1.23}$$

Hence, the vector strength can be used to estimate the shape of the stimulus–spike-train cross-spectrum by tuning the stimulation frequency f_s.

Mutual information rate MIR and spectral coherence Coh(f) As mentioned above, it is believed that the sequence of APs encodes the information that is processed by the neurons. The term information is a mathematically well defined quantity (Shannon, 1948, 1949). However, the absolute amount of information in a signal is not necessarily a useful quantity in neuroscience. More interesting is often the so called mutual information rate (MIR) (Shannon, 1948) which is the rate of information that is common to signal and response and that characterizes how well one signal encodes an other. In principle, the MIR can be measured directly, but this is numerically challenging and a large amount of data is needed (Strong et al., 1998; Bernardi and Lindner, 2015). Alternatively, for Gaussian signals a lower bound of the MIR can be given by (DeWeese and Bialek, 1995; Gabbiani, 1996)

$$\mathrm{MIR} = -\int_0^\infty \log_2\left(1 - \frac{|S_{sx}(f)|^2}{S_{xx}(f)S_{ss}(f)}\right)\mathrm{d}f. \tag{1.24}$$

Here, the integrand can be interpreted as approximation of the mutual information rate density (Bernardi and Lindner, 2015). This mutual information rate density yields a frequency-resolved measure of how much information about the input $I_s(t)$ is present in the spike train $x(t)$ in a certain frequency band. Because the logarithm is a monotonic function, its argument determines the shape of the spectral information filtering. Therefore, the coherence, defined as

$$\mathrm{Coh}(f) = \frac{|S_{sx}(f)|^2}{S_{xx}(f)S_{ss}(f)}, \tag{1.25}$$

is used to infer the neurons information-filtering properties in a frequency-resolved manner. The coherence is a quantity between zero (no linear correlation between input and output) and one (perfect linear relation between input and output). According to the shape of the coherence function, different regimes of information filtering can be distinguished. For a lowpass filter the coherence is large only at small frequencies. In this case, mostly information that is stored in low-frequent signal components is transmitted. In contrast, a broadband coherence is more or less constant in a wide frequency range and indicates an equally well transfer of information at different frequencies. The knowledge of the information filter properties of single neurons is important to explore the functioning of the neuronal system.

Coincidence measure $\Gamma_{a,b}$ When comparing the similarity between two spike trains, a and b, a useful measure is the coincidence factor $\Gamma_{a,b}$ (Kistler et al., 1997). It is defined as

$$\Gamma_{a,b} = \frac{N_{\text{coin}} - N_{\text{chance}}}{\frac{1}{2}(N_a + N_b)} \frac{1}{\mathcal{N}}. \tag{1.26}$$

Here, N_a (N_b) is the number of spikes occurring in spike train a (b) of length T. N_{coin} is the number of spikes that coincide within a precision of $\pm\Delta$. $N_{\text{chance}} = 2\Delta N_a^2/T$ is the expected number of spikes that would coincide by chance if both spike trains would have homogeneous randomly distributed spike times. The normalization factor reads as $\mathcal{N} = 1 - 2\Delta N_a/T$ and puts a limit to $\Gamma_{a,b}$ at 1 (equal to 1 for identical spike trains). Due to the subtraction of N_{chance}, it is expected to yield $\langle \Gamma_{a,b} \rangle = 0$ for independent spike trains.

1.4. A brief introduction on juxtacellular stimulation

Access to neuronal dynamics and the ability to manipulate individual cells in vivo is crucial to gain understanding of the neural code (Rieke et al., 1996). However, the experimental methods have to cope with several issues, e.g. that neurons are not freely accessible but are embedded in a network in the brain of an animal. One way to deal with this problem is to cut the brain in slices and perform experiments in a petri dish (in vitro). Advantages of this approach are e.g. that the membrane potential can be measured by intracellular measurements like the whole cell patch clamp technique (Neher and Sakmann, 1976; Ogden and Stanfield, 1994) and that the neuron no longer receives input from the surrounding network, which makes the experimental situation more stable and well controlled. However, the neuron is not in its natural environment, and therefore the situation might not be fully representative for case in vivo. Additionally, it is impossible to investigate the influence of the neural activity on the animals behavior or network dynamics.

In principle, it is possible to perform whole cell patch clamp experiments in vivo but this is experimentally challenging and the restricted recording time is short due to the reduced lifetime of the neurons. It is therefore of great interest to develop methods that allow for easy applicable in-vivo measurements of identified single cells lasting for a maximal amount of time. Previous studies showed that juxtacellular stimulation can be used to control the firing rate of individual cells in vivo (Houweling et al., 2010; Doron et al., 2017; Doron and Brecht, 2015). This technique is comparable easy to apply and experiments can last up to 3 h for a single neuron (Houweling et al., 2010). However, so far a missing

feature of juxtacellular stimulation was to go one step further than just controlling average firing rates, but also to elicit reproducible spike times. This issue is addressed in this work for pyramidal neurons in the motor- and sensory cortices of rats (the corresponding experiments have been performed by Guy Doron[1]).

1.4.1. Physical background

The juxtacellular single cell stimulation technique has its origin in the juxtacellular labeling technique (Pinault, 1996). This labeling technique is based on the finding that a bilayer lipid membrane can be reversibly perforated when a sufficient electric field is applied across the membrane (Benz et al., 1979; Glaser et al., 1988; Barnett and Weaver, 1991). Such a perforated membrane can become permeable for ions, and therefore allows to stimulate the neuron by current application. The explanation of this phenomenon is based on the theory of electroporation, as e.g. given in Barnett and Weaver (1991); Neu and Neu (2009). It is assumed that two steps are involved: First, the creation of a hydrophobic pore due to thermal fluctuations. Second, the transformation of the hydrophobic pore into a hydrophilic pore which becomes energetically favorable when the pore radius exceeds a certain value R_*. Therefore, the rate of creation of hydrophilic pores is given by the rate of creation of hydrophobic pores with radius R_* (Glaser et al., 1988). The energy that has to be overcome to create a hydrophobic pore of radius R is given by (Glaser et al., 1988)

$$E_\circ(U,R) = 2\pi hR\sigma_\circ(R) - \pi R^2 \frac{(\epsilon_w - \epsilon_m)}{h}\frac{U^2}{2}. \tag{1.27}$$

Here, R is the pore radius, h the thickness of the membrane, and $\sigma_\circ(R)$ is the effective interface tension between the internal wall of the pore and water. The first term describes the contribution due to the new contact surface between membrane (inner surrounding of the pore) and fluid. The second, voltage dependent, term describes the contribution due to the change in capacitance that occurs from pore creation. Here, ϵ_w is the permittivity of the fluid, ϵ_m is the permittivity of the membrane, and U is the voltage across the membrane.

Thus, the rate of hydrophilic pore creation, $K_p(U)$, is related to

$$K_p(U) \sim e^{-\frac{E_\circ(U,R_*)}{k_B T}}, \tag{1.28}$$

where k_B is Boltzmann's constant and T is the absolute temperature. As can be seen

[1]Guy Doron, NeuroCure Cluster of Excellence, Humboldt Universität zu Berlin, 10117 Berlin, Germany guy.doron@charite.de

from eq.(1.27) and eq.(1.28), the increase in pore formation rate due to the additionally applied membrane voltage is given by

$$\frac{K_p(U)}{K_p(0)} = e^{\frac{\pi R_*^2(\epsilon_w - \epsilon_m)U^2}{2hk_BT}}. \tag{1.29}$$

Due to the exponential dependence on U^2 there is a drastic increase in the pore creation rate with increasing voltage. Following the estimates by Glaser et al. (1988), for a voltage of 1 mV the rate increases by eight orders of magnitude. Once the membrane is perforated by hydrophilic pores, current (ions) and solutes can directly invade the cell. Hence, also water-soluble dyes can be brought into the cell, which is why this technique was initially used as cell-labeling technique (Pinault, 1996).

The access to the intracellular space via the hydrophilic pore is the reason why juxtacellular stimulation is assumed to act in a similar way as intracellular stimulation. This can e.g. be justified by the finding that positive currents depolarize the cell while negative currents hyperpolarize it (Pinault, 1996; Houweling et al., 2010) and that juxtacellularly recorded APs point in the positive direction.

Chapter 2.

Data analysis of juxtacellular stimulation experiments

2.1. Spike extraction

In this work, we are interested in the precision and reliability of APs that are evoked in response to frozen noise stimuli, and in the frequency-dependent signal-transmission properties of neurons. A simple consideration reveals that AP reliability and signal-transmission are topics that are dependent on each other: the more a neuron supports high-frequency stimulus components, the better it responds to fast stimulus changes, and therefore, the more precise is the timing of its APs in response to a particular stimulus. To elaborate on these topics, it is essential to ensure that spike times can be extracted from experimental data reliably and with a high temporal precision. Thus, we have to check carefully whether our method of spike extraction introduces some kind of error or bias.

In juxtacellular stimulation both, recording and stimulation, are done with the same electrode by rapidly switching between the two modes. Because on the one hand, the juxtacellular electrode remains outside of the cell (as explained above), the stimulation current that is needed to evoke a response is larger (typically a few to tens of nA) than e.g. for intracellular patch-clamp experiments (typically hundreds of pA). On the other hand, the measured voltage excursions due to APs are smaller than for intracellular measurements. Because of the combination of both effects, it is often the case that the APs in the recorded voltage are not clearly visible but are dominated by the fluctuations of the input stimulus. Thus, for the purpose of spike extraction, the raw-voltage trace has to be properly filtered to remove the input current and to increase the signal (AP height) to noise (voltage fluctuations) ratio such that spike times can be extracted.

To remove the stimulus from the record, we make use of input stimuli with special statistical characteristics. For most of our experiments, we apply bandpass-limited frozen

Gaussian noise stimuli with either 100 Hz or 200 Hz cutoff frequency. Here, 'Gaussian' means that the distribution from which the Fourier components of the signal are drawn is a normal distribution, and that the histogram of the stimulus in the time domain is Gaussian distributed. Such a Gaussian distribution in the time domain does not cause too many large current excursions, and we assume it to be well tolerated by the physiological constraints of real neurons. 'Bandpass-limited' refers to the finite cutoff frequency, f_c, of the stimulus, meaning that all Fourier components for $f > f_c$ equal zero. Therefore, for frequencies larger than the cutoff frequency $f > f_c$, non-zero Fourier components in the recording should originate from the neurons response or from the surrounding network, but should not be introduced by the stimulus. This property motivates to eliminate the input by removing all Fourier components for frequencies that are smaller or equal to the cutoff frequency of the input stimulus.

Briefly, we calculate the Fourier transform of the recorded voltage $\tilde{V}(f)$, multiply it with a suitable filter function and calculate the inverse Fourier transform of the product to yield the filtered voltage in the time domain. These steps can be summarized by:

$$V(t) \xrightarrow{\mathcal{F}} \tilde{V}(f) \xrightarrow{\text{filter}} \tilde{V}(f) \cdot \Theta^{\text{filter}}(f) \xrightarrow{\mathcal{F}^{-1}} V^{\text{filtered}}(t). \tag{2.1}$$

Here, the filter function $\Theta^{\text{filter}}(f)$ is basically an inverse boxcar function that removes the Fourier components around the stimulation frequencies. However, it turned out that the filtered voltage has slightly smaller artifacts when the edges of the filter are smooth. For that reason a sigmoid function is used to smooth the edges of the boxcar function:

$$\Theta^{\text{filter}}(f) = \frac{1}{1 + e^{-\frac{|f| - f_{\text{filter}}}{a}}} \Theta(|f| - f_c). \tag{2.2}$$

Here, f_c is the cutoff frequency of the input stimulus (100 Hz or 200 Hz), the parameter $f_{\text{filter}} > f_c$ gives the frequency at which the sigmoid equals 0.5 and defines the width of the filter, a gives the steepness of the sigmoid, and the last factor $\Theta(f)$ is the Heaviside function. The Heaviside-term ensures that the frequencies that belong directly to the stimulus are not only dampened but are truly set to zero. We typically use $f_{\text{filter}} = 400$ Hz and $a = 20$ Hz, irrespective of the cutoff frequency of the input to ensure that the stimulus is removed even if higher harmonics might appear.

Equivalently to the case of bandpass stimulation, also stimuli that have power only at a specific frequency can be filtered out. To remove such a harmonic stimulus that oscillates with frequency f_s, the filter eliminates the power in a narrow frequency-band centered around the stimulation frequency. To avoid slow transients that can lead to

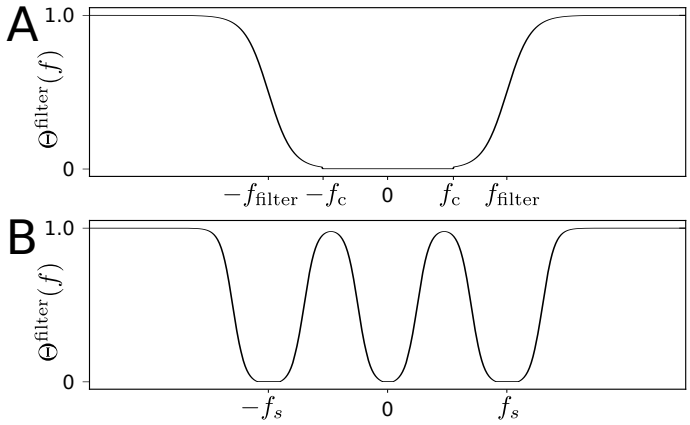

Figure 2.1.: Two possible realizations of the filter function $\Theta^{\text{filter}}(f)$. A) Filter for a bandpass stimulus with cutoff frequency f_{c}. B) Filter for a harmonic stimulus with stimulation frequency f_s. Fourier components at frequencies around zero are removed in both cases.

problems with a threshold criterion for spike extraction, additionally low frequencies are removed. In Fig.2.1, a sketch of the filters is given for both cases (bandpass and harmonic stimulation).

The four states involved in eq.(2.1) are shown in Fig.2.2A-D for an example case of a 100 Hz broadband stimulation. In Fig.2.2A, the trace is dominated by the input, which is also the case in Fig.2.2B where Fourier components for frequencies up to the cutoff frequency are the largest. These Fourier components are removed by filter application in Fig.2.2C (note different x and y-scale). The back-transformed voltage in Fig.2.2D does no longer contain the large excursions due to the input, and as a result the action potentials (APs) become visible (note different y-scale).

However, the filter procedure also removes Fourier components that belong to the response of the neuron and so the resulting voltage is not the original (extracellular) membrane potential but is a highpass-filtered version of it. In order to ensure that the filter does not remove the APs itself, the distribution of the stimulus power has to be chosen such that it does not overlap too much with the frequency domain that supports the APs. If this is ensured, we can expect to observe the APs in the filtered trace (see discussion below). From the filtered voltage trace, the spike times can be extracted by applying a simple threshold criterion: Whenever the filtered voltage crosses the threshold from below, the time instant is stored as a spike time.

To make sure that the extracted spikes belong to one single cell, and that the filtering does not influence the spike times, the procedure is carefully tested in the following.

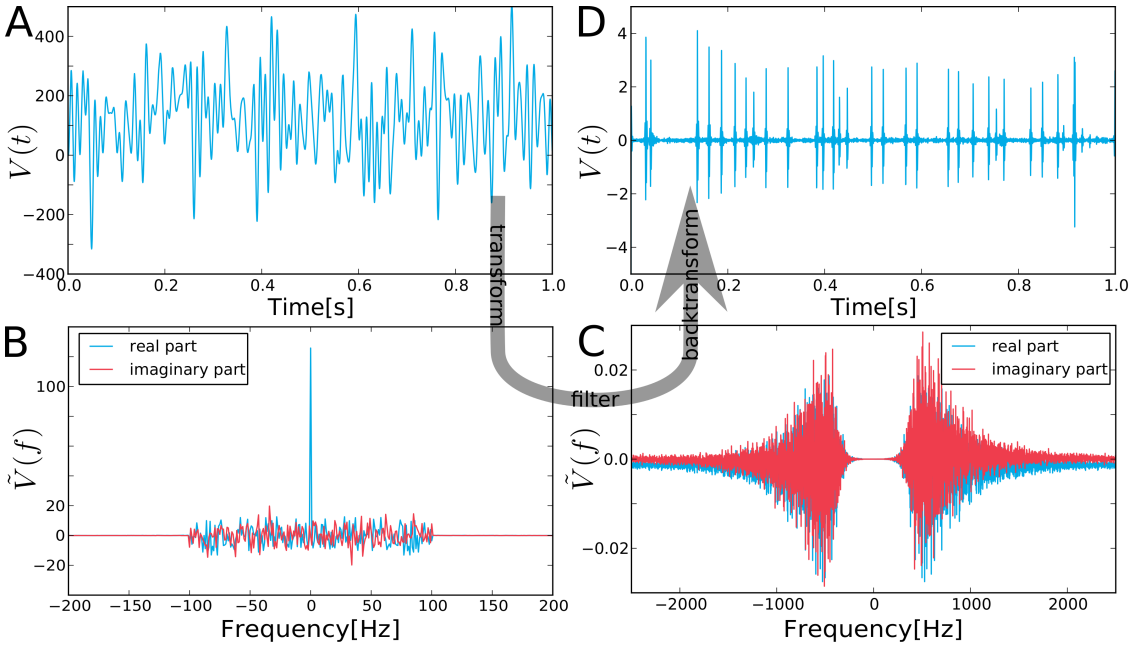

Figure 2.2.: Sketch of the filter procedure for spike extraction. A) The raw-data voltage trace measured with the juxtacellular electrode. Large fluctuations arising from the stimulation current are visible. B) The same data but in the frequency domain. The Fourier components up to the cutoff frequency ($f_c = 100\,\mathrm{Hz}$) of the input dominate the signal. C) The same as in B) but highpass filtered. Note the different scales on the axes. D) Back transform of C, i.e. highpass filtered version of the raw data shown in A. The input fluctuations are gone and the APs appear (again note different y-scale in comparison to A)

2.1.1. Effect of the filter on action potential shape and position

Because we are interested in the exact timing of APs, we have to investigate whether the manipulations in the filter procedure can introduce a bias or some kind of shift to the spike times. We also need to analyze how the spike shape is modified and how large the filter cutoff f_{filter} can be chosen. This requires knowledge of the true APs to compare them to the ones that are extracted by the procedure. When stimulating a neuron with constant current, no input fluctuations that disturb the measurement are present, and thus APs are clearly visible in the unfiltered juxtacellular voltage such that the true spike times can be extracted. Applying the filter procedure to these recordings allows us to compare original and filtered APs.

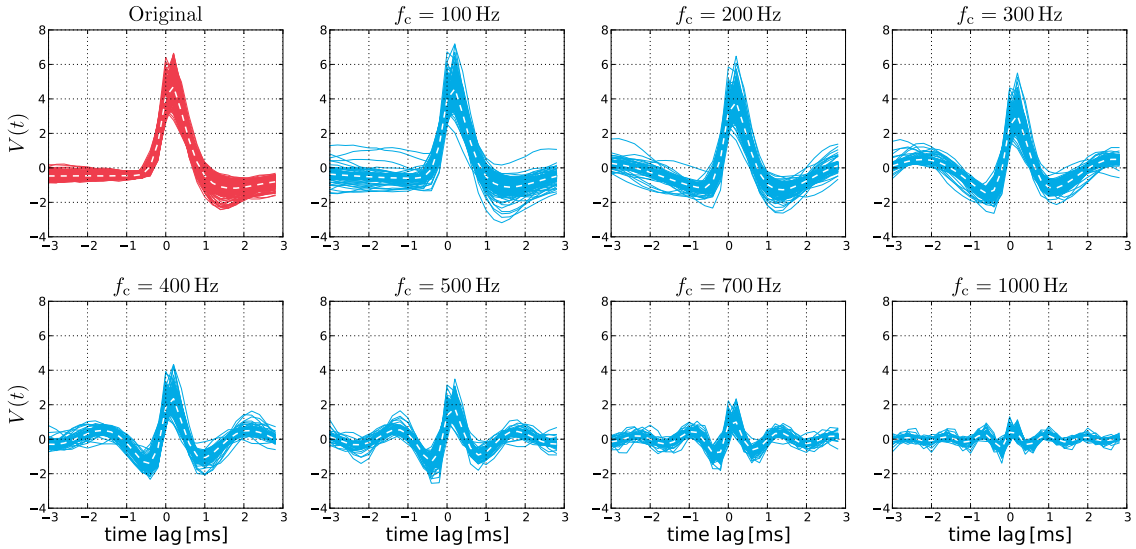

Figure 2.3.: Action potential position remains fixed under filter application The position and the shape of the APs for different filter cutoff frequencies. Solid blue lines are filtered APs, centered around the spike time of the original trace (upper left panel, red). The white dashed lines are the mean AP shapes averaged over all realizations. With increasing cutoff frequency the height of the APs decreases and oscillatory artifacts arise around the central peak.

In Fig.2.3, the shape and the relative position of the resulting APs are plotted for different filter cutoff frequencies. For each AP the voltage trace is shown in a 6 ms time window centered around the true spike time that is extracted from the original data. A filter-induced spike-time shift would result in peaks that are not centered around zero anymore. This would be the case for spike times that are either shifted systematically, resulting in a shift of the average AP peak, or that are shifted randomly, resulting in

a broadening and flattening of the average AP. When comparing the filtered and the original voltage traces, it can be seen that increasing f_c has no effect on the location of the maximum, and therefore the extracted spike times do not depend on the cutoff frequency. However, increasing f_c leads to reduced spike height and relative to the spike height more pronounced artifacts (oscillations) before and after the spike. Because the cutoff frequency in the filter has to be at least as large as the cutoff frequency of the input, this gives rise to an experimental limitation for spike extraction in case of bandpass stimuli. In our case, bandpass-stimulation experiments are restricted to cutoff frequencies of $f_c = 100\,\text{Hz}$ or $f_c = 200\,\text{Hz}$.

In contrast to bandpass stimulation, when stimulating with a pure cosine with frequency f_s, the input can be removed from the recording by eliminating the frequencies in a narrow band around the stimulation frequency f_s. This can be done with sufficiently small filter width, such that in the case of harmonic input-stimuli spike-extraction works even for high input-frequencies.

2.1.2. Justification of spike extraction in juxtacellular recordings

To justify the spike extraction procedure for juxtacellular data, the procedure is also applied to intracellular measurements that are much more controlled. In Fig.2.4, the spike extraction for juxtacellular (column A, left) and intracellular (column B, right) experiments are compared to each other. The top row (A1, B1) shows the raw data of the respective method that was recorded for a bandpass stimulation with cutoff frequency $f_c = 100\,\text{Hz}$. In the juxtacellular case the stimulus had a large variance while it had a small variance for the intracellular case. Thus, large input fluctuations dominate the juxtacellular measurement and APs are almost invisible. To illustrate the extent to which the input signal dominates the neuronal response, an AP (marked by a triangle) is shown in the inset of Fig.2.4A1. In contrast, the intracellular data show pronounced APs that are clearly visible (Fig.2.4B1). After filter application, APs are also visible in the juxtacellular measurement (Fig.2.4A2). The AP that is marked by the triangle is now visible at the same time instant as it was before filter application, and also for the filtered intracellular voltage (Fig.2.4B2) all APs are still present at the correct times.

Single- or multi-unit recordings? Besides the issue of correct spike-time extraction, one might be uncertain whether single- or multi-unit recordings are performed. In Fig.2.4A2, we observe that the APs are not really stereotype but vary in their height. This is illustrated by the histogram of AP height given at the right border of the plot (the histograms

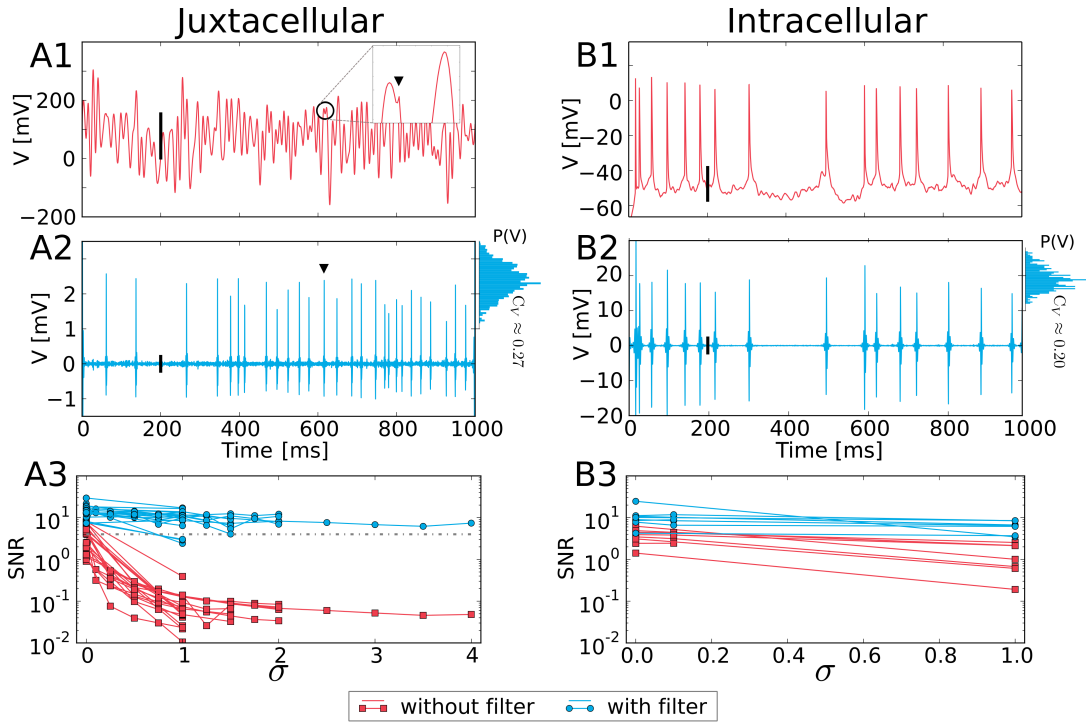

Figure 2.4.: Justification of juxtacellular spike extraction. Both columns (A and B) show similar graphs, A for juxtacellular and B for intracellular recordings. A1 and B1) The raw-voltage trace for an example measurement. The inset in A1 shows a zoom on an AP (marked by the triangle) that is hidden in the raw data. The vertical bars give the size of the standard deviation of the respective trace. A2 and B2) The filtered voltage trace. Here, APs are also visible in the juxtacellular case. The triangle highlights the same AP as in A1. On the right side of the plot a histogram of the AP height is given. A3 and B3) The signal to noise ratio (SNR) of the filtered voltage (blue) and the raw voltage (red). The respective values are plotted against σ, the factor that scales the standard deviation of the input current.

were estimated from a larger set of spike trains than shown here). The variability of the AP height is measured by the coefficient of variation and yields for the juxtacellular experiment $C_V \approx 0.27$. This variable height can be explained by variations of the AP width in combination with the filter procedure: If an AP is scaled along the time axis such that it is broader than its unscaled version, the power of this AP is shifted towards lower frequencies. Therefore, because the filter procedure removes small frequencies, the broadened AP will be stronger reduced in amplitude. This is effectively the same as applying a filter with a higher cutoff frequency (compare Fig.2.3).

To justify this hypothesis, the intracellular measurement can be used as control experiment, because it is certainly a single-unit measurement and the APs are already visible in the raw data. In the intracellular raw voltage, we can see that all APs have almost the same amplitude (Fig.2.4B1). After filter application, we observe variations of the AP height also for the intracellular voltage (as illustrated by the histogram, Fig.2.4B2). When comparing the CV of the AP height distribution for both techniques, we find comparable values for the juxtacellular and intracellular trace. This implies that the height fluctuations arise from the filter procedure and are not caused by multi-unit recordings. In particular, for multi-unit recordings we would expect a multimodal histogram of the spike height, which is not observed.

In addition, because the shape of extracellularly measured APs is determined by the current flow in the extracellular space, such APs can look quite different than those measured intracellularly. Typically, extracellular APs have a triphasic or biphasic shape with a large negative peak (Heinricher, 2004; Gold et al., 2006). The origin of this negative peak is the inward directed current that flows into the neuron during an AP (the neuron acts as a current sink). Because we do not observe this in the juxtacellular recordings, we conclude that juxtacellular stimulation and measurement is a single cell technique that behaves similar to intracellular measurements.

Quality of the recordings A bad electrode configuration can reduce the quality of the recordings by reducing the amplitude of the APs so that it might not be possible to reliably extract spike times. As a measure of the quality of a recording the signal-to-noise ratio, SNR, defined by the average AP height divided by the standard deviation of the voltage trace is used (in Fig.2.4 the standard deviation is marked as vertical black bar in the respective voltage trace)

$$\mathrm{SNR} = \frac{\langle \text{spike height} \rangle}{\mathrm{std}(V)}. \tag{2.3}$$

Because the APs are part of the voltage, they are included in the calculation of the standard deviation so that the standard deviation of the noise background is overestimated which reduces the SNR. To be conservative regarding the quality of a recording, we define the confidence level for a good recording as SNR = 4. This means that the average spike height has to be at least 4 times the standard deviation of the noise background. In Fig.2.4A3 and B3, the SNR is plotted for different cells that have been stimulated with 100 Hz bandpass stimuli of varying standard deviations. The scaling of the standard deviation of the input is plotted on the x-axis. Here, the red squares are computed for the unfiltered voltage. For these data the SNR decays with $1/\sigma$. In contrast, the SNR for the filtered voltage (blue circles) is essentially independent of the input standard deviation σ. For most cells the data points lie above our threshold of SNR = 4 (grey dashed line). Cells that have data points below this threshold are excluded from the analysis in the following. When comparing the SNR for juxtacellular and intracellular data, we find the same order of magnitude for both methods.

In summary, the above considerations make us confident that the extraction of APs from single neurons in juxtacellular stimulation is reliable and provides precise spike times.

2.2. Stimulation protocol

The data that will be analyzed in the following have been generated by two kind of experiments. We focus mainly on stimulation with fluctuating broadband stimuli but also stimulations with pure cosine stimuli of varying frequency have been applied. The broadband stimuli were used to investigate the control about the firing rate and spike timing as well to calculate the frequency-response amplitude and other transfer properties up to the cutoff frequency of the stimulus. The cosine stimuli were used to extend the frequency-response amplitude at larger frequencies in terms of the vector strength. Experiments are performed in vivo in motor neurons and sensory neurons of anesthetized Wistar rats by Guy Doron[1].

Bandpass-limited 'frozen noise' stimulus For the stimulation with bandpass-limited Gaussian white noise the injected current is of the form

$$I_s(t) = I_0 \left(\alpha + \sigma \eta_{f_c}(t)\right). \tag{2.4}$$

[1]Guy Doron, NeuroCure Cluster of Excellence, Humboldt Universität zu Berlin, 10117 Berlin, Germany guy.doron@charite.de

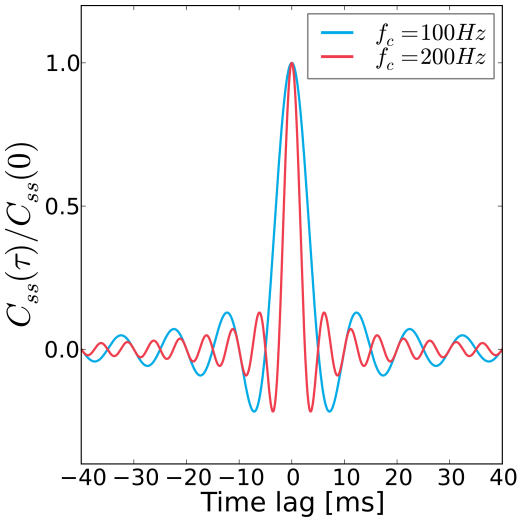

Figure 2.5.: Normalized autocorrelation function $C_{ss}(\tau)$ of the bandpass-limited input current $I_s(t)$ (eq.(2.4)) for both values of the cutoff frequency $f_c = 100\,\mathrm{Hz}$ (blue) and $f_c = 200\,\mathrm{Hz}$ (red).

Here, the random function $\eta_{f_c}(t)$ has zero mean, unit variance and is Gaussian white noise with cutoff frequency f_c. Because of the finite cutoff frequency and despite the label 'white' which refers to a flat power spectrum of $I_s(t)$, eq.(2.4) defines a so called colored noise.

In the frequency domain the power spectrum of the input current $I_s(t)$ is a boxcar function $S_{ss}(f) = S_{ss}(0)\Theta(f_c - |f|)$, with $S_{ss}(0) = I_0\sigma/f_c$. Therefore, the autocorrelation $C_{ss}(\tau)$ which is the inverse Fourier transform of the power spectrum, is a sinc function,

$$C_{ss}(\tau) = S_{ss}(0)\sin(2\pi f_c\tau)/\pi\tau. \tag{2.5}$$

The first zero crossing of this function is located where the sine has its first zero crossing (that is unequal to zero), which is at $\tau = 1/(2f_c)$. Thus, the restriction of the stimulus power to frequencies smaller than the cutoff frequency leads to a significant autocorrelation time, i.e. the time of the first zero crossing, which is 5 ms for the case of $f_c = 100\,\mathrm{Hz}$ and 2.5 ms for $f_c = 200\,\mathrm{Hz}$. In Fig.2.5, the normalized autocorrelation function is plotted for both values of the cutoff frequency.

In eq.(2.4), αI_0 is the mean value and σI_0 the standard deviation of $I_s(t)$. The constant I_0 is set during a tuning phase in the beginning of the experiment and is fixed for each neuron ($I_0 \in [1\,\mathrm{nA}, 14\,\mathrm{nA}]$) in order to yield a firing rate of roughly $15 - 30\,\mathrm{Hz}$. Thus, by changing α or σ the effect of varying the mean input or the fluctuation strength can be

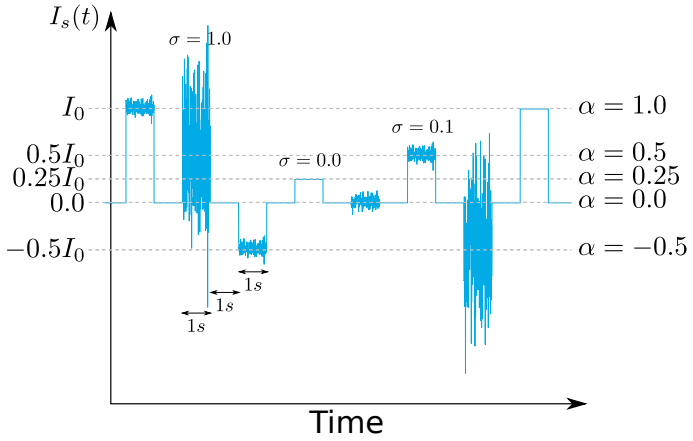

Figure 2.6.: Exemplary stimulation protocol. Periods of stimulation and silence alternate, while the order of the mean values (indicated by the dashed horizontal lines) and standard deviations is random. Different stimulus realizations have been mixed across the experiment.

compared for different neurons with different I_0.

When stimulating a neuron, either one particular realization of the frozen noise, $\eta_{f_c}(t)$, has been used or (in most cases) random switches between 10 different noise realizations were applied. Each input realization has been applied several times to record multiple trials.

Fig.2.6 shows a schematic plot that illustrates an example of the stimulation protocol. The dashed horizontal lines correspond to the α values used to scale the mean input ($\alpha \in \{-0.5, 0, 0.25, 0.5, 1\}$). The various amplitudes of the fluctuations result from different values for σ (here $\sigma \in \{0.0, 0.1, 1.0\}$). The sequence of σ and α as well as the different stimulus realizations was randomly ordered. Each stimulus lasted for 1 s and two subsequent stimuli were separated by a 1 s break.

Pure cosine stimulus In the case of harmonic input the neurons were stimulated by currents of the form

$$I_s(t) = I_0 \left(1 + \sqrt{2}\cos\left(2\pi f t\right)\right), \tag{2.6}$$

where the frequency varied between 50 Hz and 1000 Hz. The prefactor I_0 constant for each neuron and determined within a tuning phase as for the case of bandpass stimulation. The mean value and the standard deviation of this stimulus equal I_0, which (in comparison to eq.(2.4)) corresponds to $\alpha = 1$ and $\sigma = 1$. Again, the stimulus was applied for 1 s time

windows interrupted by 1 s breaks.

2.3. Spike-train control

For the purpose of investigating the control about spike trains, neurons were stimulated with input of the form of eq.(2.4) with $f_c = 100\,\mathrm{Hz}$ and systematically varying parameter α and σ. In particular, $\alpha \in \{-0.5, 0, 0.25, 0.5, 1\}$ and $\sigma \in \{0, 0.01, 0.1, 1\}$ have been used for most cells, while some cells were also stimulated with intermediate and larger σ values. Typically, ten realizations of the frozen noise stimulus have been generated for each parameter pair α, σ and each realization was applied several times.

In Fig.2.7, the results of such an experiment are given for one example cell and one particular frozen noise realization. In the first row, the respective realization of the stimulation current for different standard deviations (for the case of maximal mean; $\alpha = 1$) is given. In the subsequent rows, raster plots for different values of the mean input and standard deviation are shown. The raster plots in different columns correspond to different standard deviations (σ) of the stimulus, increasing from left to right while different rows correspond to different mean input (α), increasing from top to bottom.

2.3.1. Firing-rate control

In Fig.2.7, in each column the number of action potentials increases with α (from top to bottom). This implies that a positive current depolarizes the cell while a negative current hyperpolarizes it and agrees with the observation that the firing rate increases with the mean input (Houweling and Brecht, 2008; Houweling et al., 2010). Thus, the neurons are affected by the (external) stimulus in a similar way as it would be the case for an intracellular recording. The relationship between firing rate and mean input current is quantified in Fig.2.8 for more cells. Because the factor I_0 was fixed for each neuron separately, the firing rate is not directly plotted versus the mean input, $I_0\alpha$, but versus α which is the factor that has been varied. This was done to make different neurons comparable.

The gray lines show the mean firing rates of individual cells whereas the colored lines are averages over the cell ensemble. Different cells exhibit quite different firing rates for each input level α, but all of them tend to increase their firing rate with the mean input. When comparing the case with small stimulus amplitude, $\sigma < 1$ (Fig.2.8A), to the one with large amplitude, $\sigma = 1$ (Fig.2.8B), a linearizing effect in the firing rate curve can be observed. This is a well known feature of neuron models, known as firing rate linearization

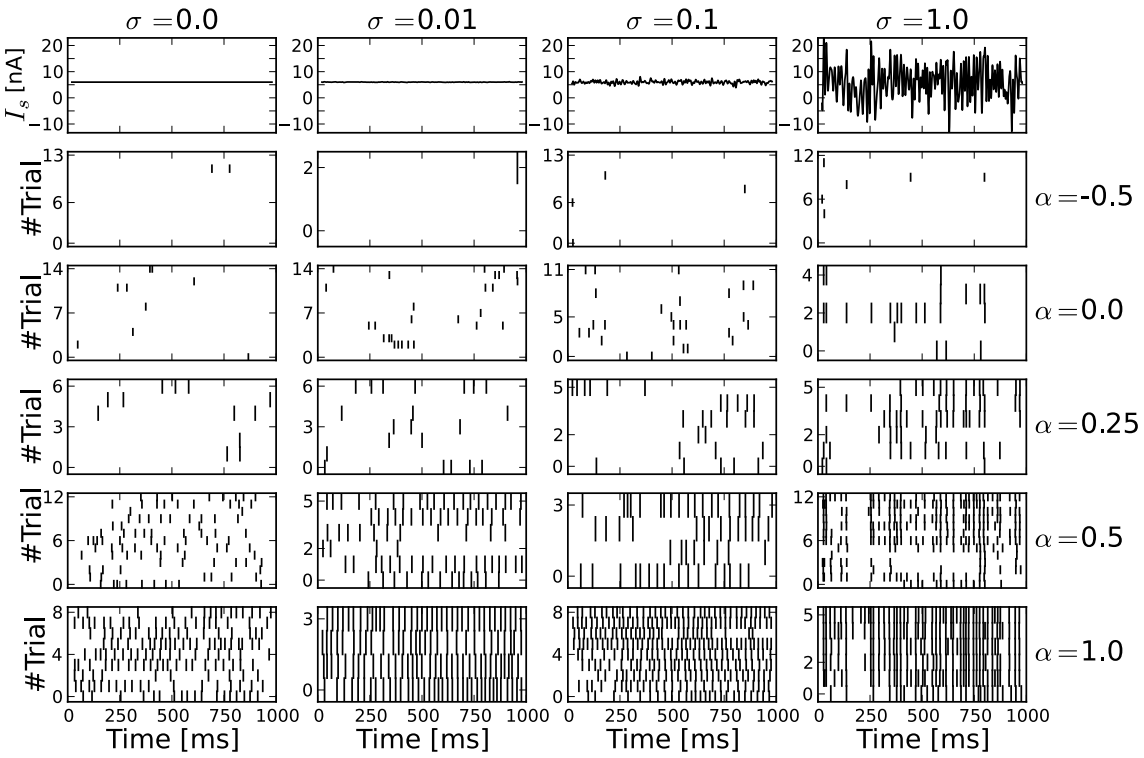

Figure 2.7.: Juxtacellular stimulation yields good control of neuronal spiking. Synchrony increases with σ, the rate increases with α. Each column corresponds to a certain standard deviation of the stimulus. As labeled at the top of the plot σ increases from the left to the right column ($\sigma \in \{0, 0.01, 0.1, 1\}$). The top row shows the stimulus with the respective standard deviation (the mean of the stimulus is that for $\alpha = 1$). Each row below shows raster plots that correspond to a certain mean value of the input. The varying size of AP markers results from the varying number of trials. As labeled at the right of the plot α increases from top to bottom ($\alpha \in \{-0.5, 0, 0.25, 0.5, 1\}$). The firing rate increases with α and large standard deviations yield coincident spike times while standard deviations yield unreliably distributed spike times.

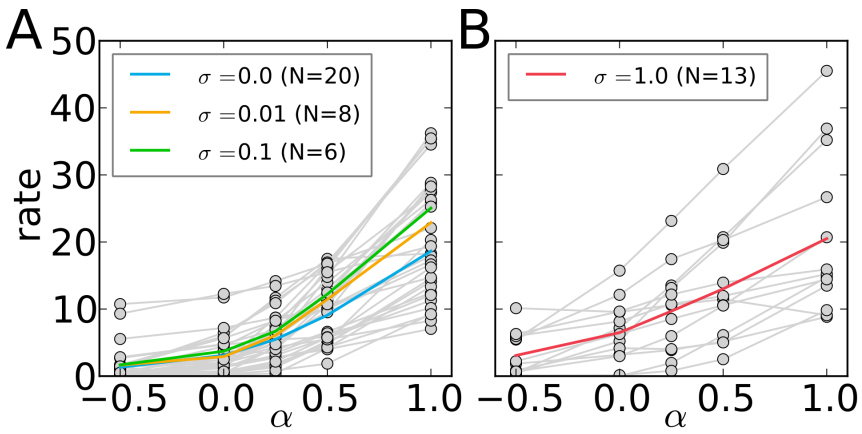

Figure 2.8.: Mean firing rate is well controlled by the mean input current. The mean firing rate plotted over α (the factor that scales the mean input). The two plots separate the cases of stimulation with: A) small standard deviation and B) large standard deviation. Grey circles belong to individual cells, while the colored lines are averages over the cell ensemble for the respective value of σ.

due to noise (Clay, 1976; Yu and Lewis, 1989).

2.3.2. Spike-time reliability

Besides the increase of the firing rate, we can make another observation in Fig.2.7 when comparing raster plots for different stimulus variances (different columns). For large σ more spikes coincide from trial to trial, which leads to vertical lines going through the raster plot. Therefore, similar to the well known result by Mainen and Sejnowski (1995), we find that temporal fluctuations in the input can increase the spike-time reliability and lead to reproducible spike trains. However, in Mainen and Sejnowski (1995) the experimental setup is different because these are whole cell recordings in vitro, and therefore the background noise that desynchronizes the spike trains is mainly due to channel noise. In contrast to this, in our situation the stimulated cell is embedded in an intact neuronal network in vivo and thus it is subject to a much stronger noise source which is the dendritic input from the surrounding cells. Because of this, repetitive presentations of the same stimulus are not necessarily expected to evoke the spike times with the same reliability as for the in vitro case.

To quantify the similarity between spike trains, we use the coincidence measure Γ, eq.(1.26), introduced by Kistler et al. (1997). In Fig.2.9A,B, scatter plots with the firing rate on the y-axes and the coincidence factor on the x-axes are plotted. Fig.2.9A shows the data points for weak variance ($\sigma < 0.5$), while Fig.2.9B shows those for larger variance

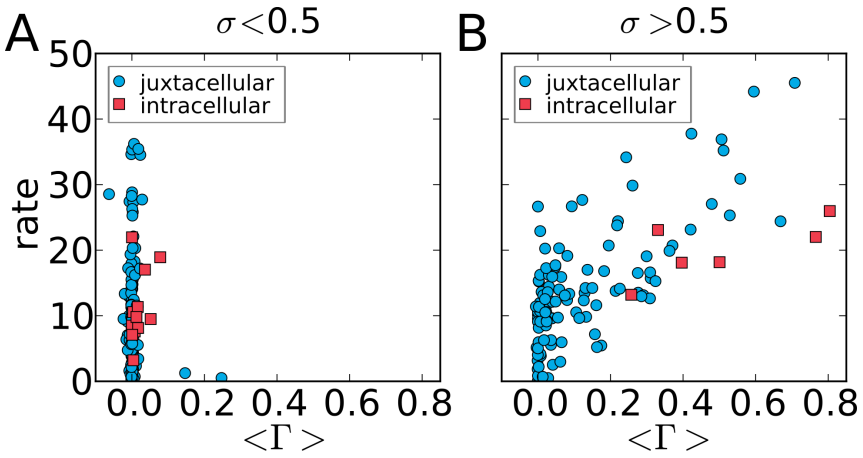

Figure 2.9.: Unreliable spiking for weak σ and high reliability for large σ. The coincidence factor Γ and the firing rate are plotted against each other. The two plots separate the cases of stimulation with: A) small standard deviation ($\sigma < 0.5$) and B) large standard deviation ($\sigma > 0.5$). Blue markers show the results for juxtacellular experiments, red marker for intracellular experiments. For both techniques and independent of the firing rate, small σ does not result in reliable spiking (left plot), while large σ can result in reliable spike times. One intracellular data point is omitted in panel B (coordinates (81.6, 0.77)).

($\sigma > 0.5$) of the input stimulus. For small σ, the values of Γ are centered around $\Gamma = 0$, which means that the spike times appear randomly distributed and independent from trial to trial. Fig.2.9B shows the case for larger σ ($\sigma > 0.5$). Here, the data points are wide spread up to large values of $\Gamma \approx 0.75$. Note that $\Gamma = 1$ is the maximal value that is only achieved for identical spike trains.

Besides the tendency that Γ increases with the stimulus variance σ^2, we observe that high Γ-values correspond to high firing rates. This can be explained by the following consideration: When a signal increases the firing rate of a neuron this can happen in two different ways. Either the introduced APs are randomly distributed, which will lead to an increase of the firing rate but will let Γ unchanged (Fig.2.9A), or the spike times of the APs are correlated due to the temporal structure of the common signal, which would cause an increase in the Γ factor. In particular, the more spikes are introduced at reliable times, the more pronounced is the increase of Γ. This causes a correlation between Γ and the firing rate (Fig.2.9B). However, note that there are two distinct ways how the introduction of reliable spikes can happen, and that it is not clear which one takes place here. First, for both ways we can think of the constant part of the stimulus to introduce spikes times at random positions. Second, these random spike times are modified by the noisy part of the

stimulus either by i) sifting them towards specific spike times or ii) deleting some spikes and adding them at reliable times. In (Voroneko et al., 2015) it has been shown that this issue can have consequences for the information filtering properties of the neuron and e.g. can lead to a highpass filter of information for the case of shifted spike times.

To compare the performance of juxtacellular stimulation to that of intracellular stimulation, equivalent experiments for the latter method have been performed and the resulting Γ-values are given in Fig.2.9 (red squares). Both methods display a similar dependence between firing rate and coincidence measure and also the maximal achieved Γ-values are similar. This means that under Gaussian bandpass stimulation our juxtacellular in-vivo stimulation yields a spike-time reliability that is similar to that of intracellular stimulation in vivo.

2.4. Transfer properties

In the previous section, we have studied the juxtacellular stimulation from a more technical perspective. In particular, we showed that frozen noise stimuli can be used to generate reproducible spike trains. However, when a stimulus elicits again and again a similar response, it is evident that the response is somehow related to this stimulus. Such a relation can be quantitatively analyzed e.g. in terms of input-output statistics. But also measures like spike-train–spike-train statistics can provide useful insights into the response properties of the neuron.

In the following, a detailed analysis of the experimental data is presented. The data were recorded in motor and sensory cortices during juxtacellular bandpass stimulation with a cutoff frequency of 100 Hz or 200 Hz, or during stimulation with pure cosine stimuli. Because no systematic differences between data from one or the other cortex could be observed, we pooled data from both cortices together. Irrespective of the stimulus properties (mean and amplitude), the data are sorted into three groups that are defined by different levels of spike-time reliability: i) weak reliability $\Gamma < 0.15$, ii) intermediate reliability $0.15 < \Gamma < 0.35$, ii) large reliability $\Gamma > 0.35$, and are averaged over the respective group. Only experiments for which 10 stimulus realizations are used have been included in the analysis.

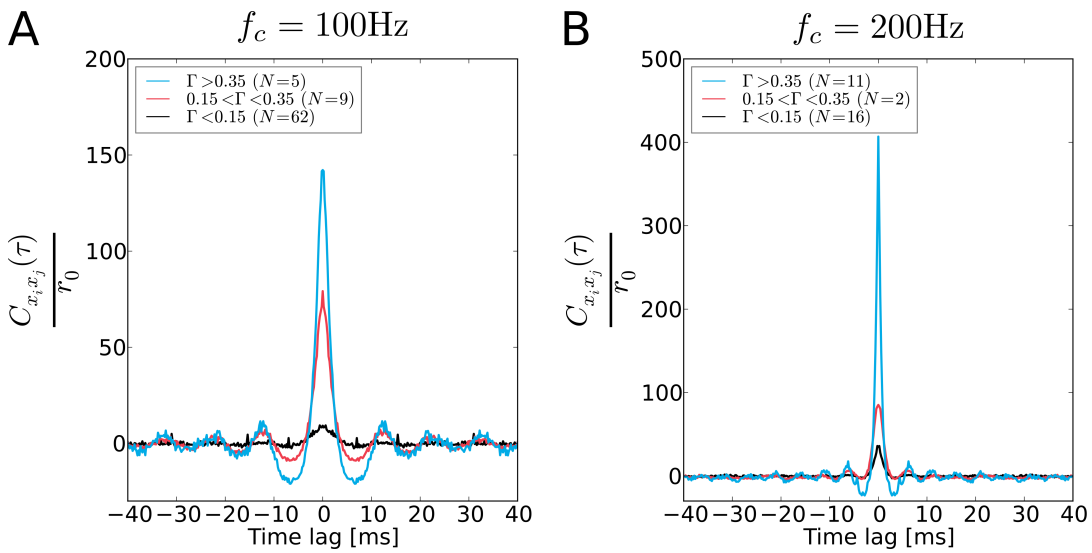

Figure 2.10.: Large coincidence Γ corresponds to peaked spike-train cross-correlation $C_{x_i x_j}(\tau)$. The spike-train–spike-train cross-correlation normalized by the firing rate. A) Input cutoff-frequency $f_c = 100$ Hz, B) Input cutoff-frequency $f_c = 200$ Hz). Different colors correspond to different amounts of spiking reliability (Γ-levels). The pronounced peak at zero corresponds to an increased probability that two spike trains have spikes occurring at the same time.

2.4.1. Spike-train–spike-train cross-correlation

As explained in the introduction (eq.(1.14)), the probability of having synchronous spikes in different trials is given by

$$P(0) = \left(\frac{C_{x_i x_j}(0)}{r_0} + r_0 \right) \mathrm{d}t. \tag{2.7}$$

Thus, it is to expect that a high Γ-value is translated into a spike-train–spike-train cross-correlation, $C_{x_i x_j}(\tau)$, that is peaked around zero. For perfectly synchronous spikes, the peak at zero would have the width of the time bin. However, in real neurons the spikes are not perfectly in time and thus the width of the peak is related to the precision of the synchrony. In Fig.2.10, the spike-train–spike-train cross-correlation normalized by the firing rate is plotted for the three subsets of the data (weak, intermediate and high synchrony). Here, the cross-correlation is computed only for pairs of spike trains that belong to the same stimulus realization and is averaged over all possible combination of distinct trials and all different stimuli. We define the width of the peak, δ, as the time of the first zero crossing of $C_{x_i x_j}(\tau)$. This results in $\delta \approx 4.4$ ms for intermediate and $\delta \approx 3.2$ ms

for high synchrony in the case of 100 Hz bandpass stimulation. For 200 Hz bandpass stimulation, we find $\delta \approx 2.8$ ms for intermediate and $\delta \approx 1.8$ ms for high synchrony. The sharper peak for 200 Hz shows that the jitter in the spike times is smaller in comparison to the 100 Hz case and indicates that spikes are more precisely timed. Overall, the small width of the peak in the cross-correlations shows that precise timing of APs in the range of a few ms could be achieved.

Right next to the peak at zero, minima can be observed in the cross-correlation function. These minima can have two reasons: First, there is a lower bound for the temporal proximity of two consecutive APs. This is due to the finite duration of the AP and the refractory time that is necessary for the neuron to be ready to fire again. Therefore, the probability to fire an AP right after a previous AP has appeared is reduced. Second, the autocorrelation of the stimulus (eq.(2.5)) shows that there is an increased probability that the stimulus is negative a certain amount of time after it was positive. This can be concluded from the negative peaks in Fig.2.5 that are next to the central positive peak. Thus, if it is likely to fire an AP at a time when the stimulus is positive, in turn it is more unlikely to fire later (when the probability is higher that the stimulus is negative). Because the position of the minima in Fig.2.10 depends on the cutoff frequency of the stimulus and roughly agrees with that in the autocorrelation, the second explanation seems to be more important in our case.

Note that the precision of spiking is related to the width of the peak in the spike-train–spike-train cross-correlation, while the reliability of AP appearance can be characterized by the area under the peak, or as in our case, is given by the Γ-factor.

Theoretical results of the spike-train–spike-train cross-correlation for a conceptually different situation, namely a conductance based synaptic input signal, have been derived in the linear response regime in Ostojic et al. (2009). Although in our case the input signal is not a conductance but a current input, this study reveals qualitatively the same results: It shows for the case in which the input signal dominates the background noise that the correlation function is peaked around zero and has a symmetric oscillatory decrease with increasing time lag. For a decreasing ratio of signal and noise strength, the oscillations in the correlation function vanish and it becomes monotonically decreasing, which agrees with our observation for $\Gamma < 0.15$ in Fig.2.10. Also, the broadening of the central peak with the correlation time of the input signal (or in our case the inverse cutoff frequency) is found in their publication.

According to Ostojic et al. (2009), the width of the peak is related to the largest time scale that is present either in the statistics of the input current or in the linear response function of the neuronal dynamic. Thus, the significant sharpening of the peak when

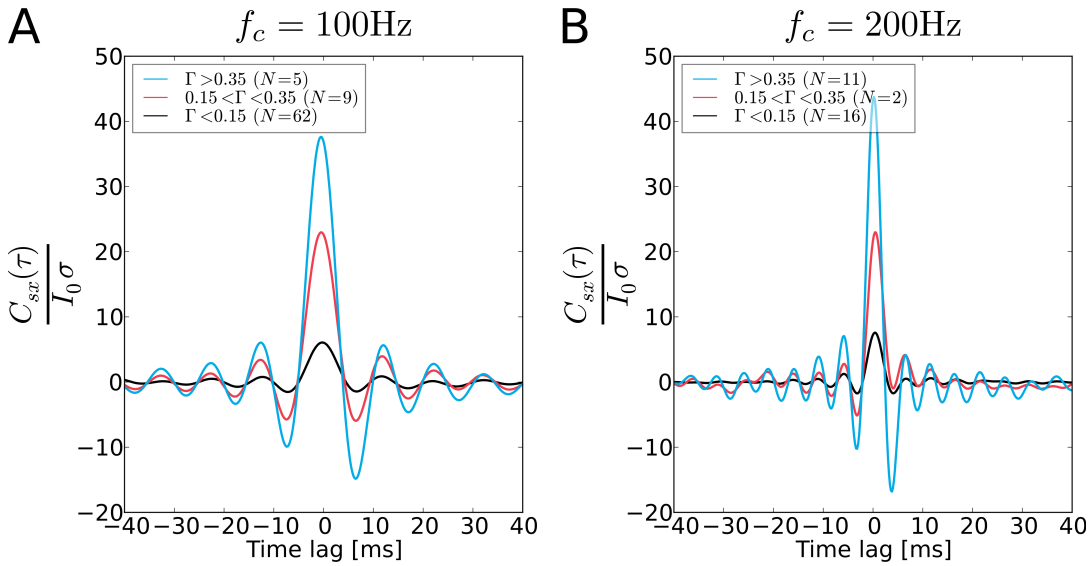

Figure 2.11.: Large coincidence Γ corresponds to peaked input-output cross-correlation $C_{sx}(\tau)$. The stimulus–spike-train cross-correlation normalized by the input strength. A) Input cutoff-frequency $f_c = 100\,\mathrm{Hz}$, B) Input cutoff-frequency $f_c = 200\,\mathrm{Hz}$. Different colors correspond to different amounts of spiking reliability (Γ-levels). The peak around zero corresponds to the fact that positive currents drive the neuron to generate APs. The non-vanishing cross-correlation at negative time lags is due to the finite width of the stimulus auto-correlation function.

switching from 100 Hz to 200 Hz (compare Fig.2.10A and Fig.2.10B) indicates that the largest time scale of the neuronal dynamics is clearly below that of the 100 Hz stimulus, which reflects the neurons ability to reliably respond to rapid stimulus changes.

2.4.2. Stimulus–spike-train cross-correlation

From the above considerations, we have concluded that spike trains which belong to the same stimulus realization are, to some extent, similar. Obviously, the reason for this similarity is the common stimulus. The correlation between this stimulus and the corresponding spike trains can be quantified by the stimulus–spike-train cross-correlation, $C_{sx}(\tau)$. Because a scaling of the stimulus results in the same scaling of the correlation function, the ratio $C_{sx}(\tau)/(I_0\sigma)$ is plotted in Fig.2.11. The correlation function shows a peak that is located close to zero time lag and that increases with Γ. Because $C_{sx}(\tau)$ is not symmetric, the width of the peak is defined by $\delta = \frac{\tau_{0+}-\tau_{0-}}{2}$ where $\tau_{0\pm}$ is the left and the right zero crossing. In case of 100 Hz bandpass stimulation, we observe a narrow peak with a width of $\delta \approx 4.8\,\mathrm{ms}$ for intermediate and $\delta \approx 4.0\,\mathrm{ms}$ for high reliability. For

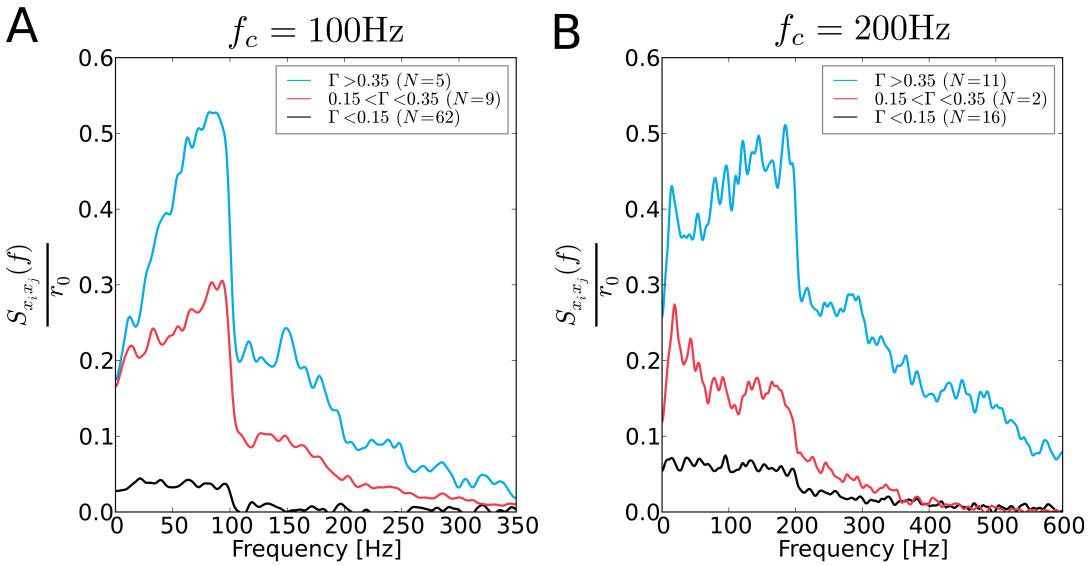

Figure 2.12.: Sustained spike-train–spike-train cross-spectra $S_{x_i x_j}(f)$ up to high frequencies. The spike-train–spike-train cross-spectrum normalized by the firing rate. A) Input cutoff-frequency $f_c = 100\,\mathrm{Hz}$, B) Input cutoff-frequency $f_c = 200\,\mathrm{Hz}$. Different colors correspond to different amounts of spiking reliability (Γ-levels). The spike-train–spike-train cross-spectra have a drop at the inputs cutoff-frequency.

200 Hz the peak is even sharper with a width of $\delta \approx 3.6\,\mathrm{ms}$ for intermediate and $\delta \approx 2.8\,\mathrm{ms}$ for high synchrony. A significant fraction of these peaks lies in the region with negative time lag $\tau < 0$. On the first glance this might be irritating because the stimulus evokes the spike train and thus the former variable should proceed the latter, which is typically associated with a non-vanishing correlation only for positive time lags. However, here this observation is not due to acausality but is a result of the finite bandwidth of the stimulus. As given in eq.(2.5), the autocorrelation function of the input stimulus is a sinc function (see Fig.2.5) that has a width of the central peak which is given by $\delta = 1/(2f_c)$. Thus, the width of the peaks of $C_{sx}(\tau)$ are in the order of the width of the autocorrelation, i.e. 5 ms and 2.5 ms for $f_c = 100\,\mathrm{Hz}$ and $f_c = 200\,\mathrm{Hz}$ respectively.

2.4.3. Spike-train–spike-train cross-spectrum

The Fourier transform of the spike-train–spike-train cross-correlation $C_{x_i x_j}(\tau)$ is the spike-train–spike-train cross-spectrum, $S_{x_i x_j}(f)$. Because $C_{x_i x_j}(\tau)$ is an even function $S_{x_i x_j}(f)$ is real.

In Fig.2.12, $S_{x_i x_j}(f)/r_0$ is plotted. The cross-spectra show a sharp drop that is associated with the respective stimulus cutoff frequency $f_c = 100\,\mathrm{Hz}$ and $f_c = 200\,\mathrm{Hz}$. Thus,

Fourier components that directly originate from the response to the stimulus are dominant within the spike trains. In particular, for high reliability ($\Gamma > 0.35$) the spectra increase with frequency. On the one hand, the dominant presence of high-frequency components can be seen as a result of the peakedness of the cross-correlation function $C_{x_i x_j}(\tau)$, and therefore is a result of the precise timing of APs (the Fourier transform of a narrow distribution in the time domain yields a broad distribution in the frequency domain). On the other hand, because the stimulus is the source of the common Fourier components in the spike trains, it is an indicator of how strong the neuron responds to certain frequencies of the stimulus.

This explanation s is supported by the results in Ostojic et al. (2009) for the case of synaptic input that is modeled as transient conductance increase. These calculations reveal that the cross-spectrum between trials of a frozen synaptic input signal is given by

$$S_{x_i x_j}(f) = \frac{r_{0,\mathrm{syn}}^2}{r_0^2} |S_{sx}(f) g_{\mathrm{syn}}(f)|^2 S_{yy}(f), \tag{2.8}$$

where $S_{yy}(f)$ is the power spectrum of the summed synaptic input, $g_{\mathrm{syn}}(f)$ is the Fourier transform of the synaptic filter, $r_{0,\mathrm{syn}}$ is the firing rate of the synaptic input, and $S_{sx}(f)$ is the input-output cross-spectrum of the neuron. Thus, eq.(2.8) reveals that the shape of the spike-train–spike-train cross-spectrum, $S_{x_i x_j}(f)$, is proportional to the squared input-output cross-spectrum, and therefore is strongly affected by the latter.

2.4.4. Stimulus–spike-train cross-spectrum

The stimulus–spike-train cross-spectrum, $S_{sx}(f)$, is also known as frequency-response amplitude and is the Fourier transform of the stimulus–spike-train cross-correlation. In Fig.2.13, the ratio $|S_{sx}(f)|/(I_0\sigma)$ is plotted for $f_c = 100\,\mathrm{Hz}$ and $f_c = 200\,\mathrm{Hz}$. The sharp peak in $C_{sx}(\tau)$ (shown in Fig.2.11) that results from the close locking of the spike trains on the stimulus translates into a stimulus–spike-train cross-spectrum that has power up to high frequencies. The cross-spectra for low Γ-values are smaller than for large Γ. Because the spectra are normalized by $I_0\sigma$ this different height does result from the scaling that is introduced by different stimulation strength. Instead, less reliable spike trains (small Γ) indicate that the neurons do not follow the stimulus as close as for more reliable spike trains (large Γ). This is because unreliable spike trains are evoked, relative to the stimulation strength, by a larger fraction of intrinsic noise.

For reliably spiking cells, we find that the cross-spectrum increases in the whole frequency range up to the input's cutoff frequency, while it seems to be approximately con-

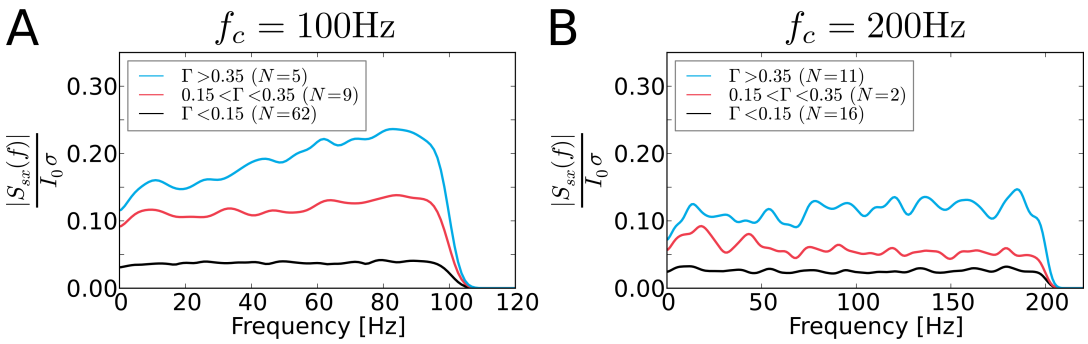

Figure 2.13.: Sustained stimulus–spike-train cross-spectra $S_{sx}(f)$ up to high frequencies. The stimulus–spike-train cross-spectrum normalized by the input strength. A) Input cutoff-frequency $f_c = 100$ Hz, B) Input cutoff-frequency $f_c = 200$ Hz. Different colors correspond to different amounts of spiking reliability (Γ-levels). The stimulus–spike-train cross-spectrum does not show a cutoff before the inputs cutoff frequency. Therefore, the neurons track frequencies way above their firing rate.

stant for others. In particular, we do not observe a lowpass shape with a cutoff in the range of the firing rate, as predicted for one-compartment IF models (Lindner and Schimansky-Geier, 2001; Brunel et al., 2001; Fourcaud-Trocmé et al., 2003). This indicates that the neurons reliably respond to input changes that are faster than their firing rates.

2.4.5. Coherence and mutual information rate

Despite the question how strong the response to a certain input frequency is, it is of great interest to infer the transfer of information in a frequency-resolved manner. The total information that is common to both, input and output, is called mutual information. The mutual information per time is given by the mutual information rate (MIR). As given in eq.(1.24), the MIR for Gaussian signals can be approximated by a lower bound (DeWeese and Bialek, 1995; Gabbiani, 1996)

$$\mathrm{MIR} = -\int_0^{f_c} \log\left(1 - \mathrm{Coh}(f)\right) \mathrm{d}f.$$

When interpreting the integrand as approximation of the MIR density, the shape of the coherence defines the neurons information-transfer properties in a frequency-resolved way. In Fig.2.14, the coherence function is given for 100 Hz and 200 Hz, again for the three subsets $\Gamma < 0.15$ (weak reliability), $0.15 < \Gamma < 0.35$ (intermediate reliability) and $\Gamma > 0.35$ (high reliability).

In line with the results for the stimulus–spike-train cross-spectrum (see Fig.2.13), the

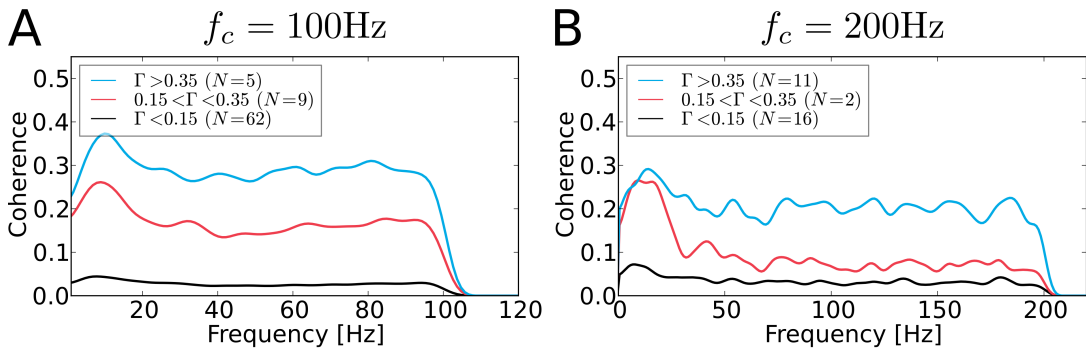

Figure 2.14.: Spectral coherence function reveals broadband coding of information. The spectral coherence function. A) Input cutoff-frequency $f_c = 100$ Hz, B) Input cutoff-frequency $f_c = 200$ Hz. Different colors correspond to different amounts of spiking reliability (Γ-levels). For high reliability Γ the spectral coherence function is constant up to the inputs cutoff.

coherence is larger for the highly reliable spike trains than for those that are less reliable. We find that there is no lowpass shape in the coherence which is in contrast to what one would expect from the predictions of one-compartment IF-models (Vilela and Lindner, 2009b). The large coherence values for frequencies that are multiple of the firing rate is an unexpected result and indicates that the neurons encode a significant amount of information at high frequencies. In particular, the almost flat shape indicates that they do not prefer any specific frequency, but encode information equally well for all frequencies.

The relation between reliability (Γ) and lower-bound estimate of the total amount of mutual information per time (MIR) is plotted in Fig.2.15. Here, each data point represents the stimulation of one neuron with one particular stimulation paradigm (specific choice of the parameters α, σ). Different colors correspond to different neurons. The overall increase of the coherence with Γ is translated into a larger mutual information rate for high Γ values. Interestingly, this relation seems to follow an almost linear dependence. For strong coincidences the values of the lower bound reach 70 bit/s for the 100 Hz stimulation and go beyond 100 bits/s for the 200 Hz case. These values are comparable to information rates measured in various sensory neurons (cf. Table 2 in Borst and Theunissen (1999)). However, note that for little trial-to-trial variability, the true mutual information rate can be significantly larger than this lower-bound estimate because of nonlinear encoding that is not described by the coherence function (Borst and Theunissen, 1999; Bernardi and Lindner, 2015).

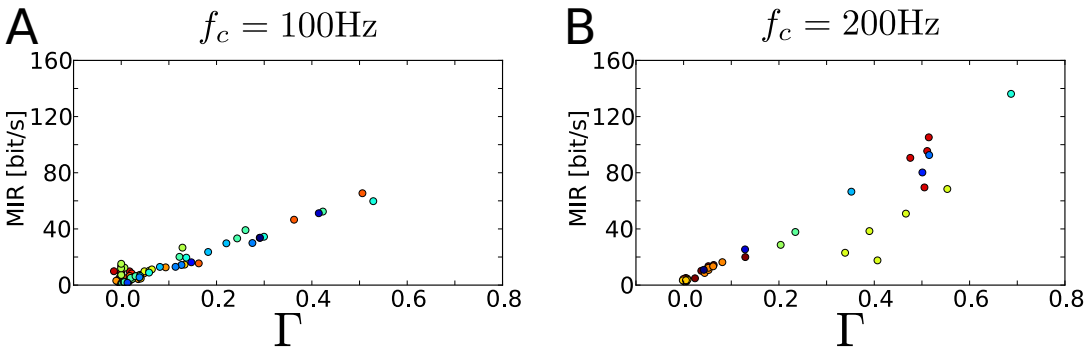

Figure 2.15.: Mutual information increases with spike-time reliability. The lower bound on the mutual information rate MIR versus the spike-time reliability. A) Input cutoff-frequency $f_c = 100\,\mathrm{Hz}$, B) Input cutoff-frequency $f_c = 200\,\mathrm{Hz}$. Different cells are marked in different colors, repetitive occurrence of the same color indicates that this cell has been stimulated with different stimulus statistics (values for α and σ).

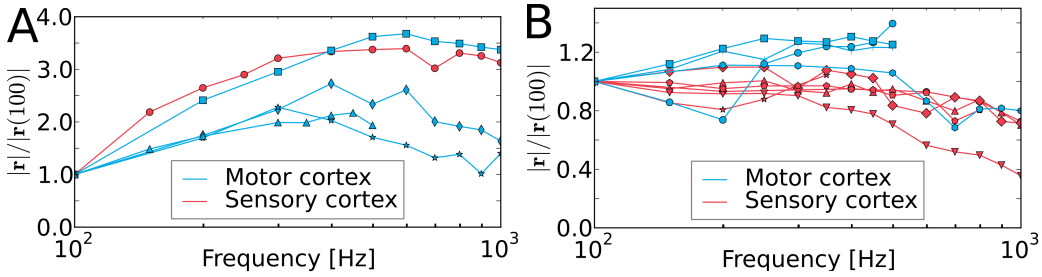

Figure 2.16.: The vector strength reveals that neurons can reliably track fast stimuli. Both figures show the vector strength for cells from motor cortex (blue) and sensory (red) cortex in a frequency range from 100 Hz to 1000 Hz. A) Cells that show an initially increasing vector strength. B) Remaining cells. Notably for non of the cells a clear cutoff in the range of the firing rage can be identified.

2.4.6. Vector strength

For the purpose of exploring the frequency-response amplitude in a wider frequency range, experiments with harmonic stimuli of the form given in eq.(2.6) have been performed. In these experiments, the stimulation frequency was varied from $f_s = 100\,\mathrm{Hz}$ to $f_s = 1000\,\mathrm{Hz}$.

In Fig.2.16, the absolute value of the vector strength, normalized by its value at 100 Hz, is plotted. Here, cells from the different cortices are color coded. The individual curves display a large variability in the frequency dependence and were sorted in two groups, A and B: In Fig.2.16A, cells for which the vector strength shows a pronounced initial increase are plotted, while cells were this is not the case are given in Fig.2.16B. The curves in Fig.2.16A tend to show shallow maxima around $f_s = 600\,\mathrm{Hz}$ and remain above

the value at 100 Hz even for the largest frequencies. Some of the curves in Fig.2.16B start to decrease around $f_s = 400$ Hz, however, this decrease is only slight and no clear cutoff frequency can be identified from the data. Given the strong cell-to-cell variability, there was no principal difference with respect to high-frequency coding for the data measured in motor cortex (blue) and somatosensory cortex (red).

Hence, the sustained high-frequency support that has been observed for bandpass stimulation can also be found for harmonic stimulation in a much wider frequency range.

2.5. Summary

In this chapter, the method of spike extraction for juxtacellular broadband stimulation has been carried out and justified. We showed that spike extraction for stimulation currents with cutoff frequencies that do not exceed a few hundred Hz is reliable.

We also showed that juxtacellular stimulation provides a good control about neuronal spiking activity in vivo. In particular, fluctuating stimuli can drive neurons to reliably generate reproducible spike trains with a spiking precision in the range of ms. From the experimental side of view, such a control about single-cell dynamics in vivo is an important tool that may set the basis for new reverse physiology experiments. Such experiments could e.g. investigate the role of particular spike sequences on the animals behavior and thus would e.g. deepen the studies from Brecht et al. (2004); Houweling and Brecht (2008); Li et al. (2009), where the influence of single spikes on the animals behavior or brain state has been investigated.

We found for pyramidal cells in the motor and sensory cortex that the input-output cross-spectra and the spectral coherence do not exhibit a lowpass characteristic. In contrast, the cells provide a sustained response to stimulation frequencies that are way beyond the inverse of the membrane time constant or the firing rate of the neuron. In terms of the vector strength, we could show that the high-frequency support is large up to 1000 Hz (the limit of our experimental investigation). A large vector strength at high frequencies has also been measured in previous in-vitro (Köndgen et al., 2008; Boucsein et al., 2009; Tchumatchenko et al., 2011; Ilin et al., 2013; Ostojic et al., 2015) and in-vivo (Tchumatchenko et al., 2011) experiments. These studies often reported a cutoff in the vector strength at several hundred Hz. To our knowledge, the only study that reported an increasing vector strength and sustained support up to 1000 Hz (as we found for some cells [see Fig.2.16A]) was a study on Purkinje cells (which have an exceptional large dendritic tree) by Ostojic et al. (2015).

Besides the sustained support of power at high frequencies, the broadband shape of

the spectral coherence is in contrast to the characteristics of simple one-compartment IF models. Such a flat coherence implies that no information filtering with respect to the different Fourier components of the input signal takes place, instead, information is transferred equally well for all frequencies up to the cutoff of the stimulus. The ability of neurons to rapidly respond to stimulus changes and to provide broadband information coding is potentially of major importance for the functioning of the nervous system.

Chapter 3.

Theoretical description: Capturing salient features of neuronal dynamics

This chapter deals with the attempt to use a mathematical neuron model in order to describe the statistics that have been measured experimentally in cortical neurons in vivo (see previous section). The quantitative reproduction of experimentally measured data by simple neuron models has also been addressed in previous studies in vitro (Jolivet and Gerstner; Paninskia et al., 2005; Clopath et al., 2007; Naud et al.) and in vivo (Lansky et al., 2006) (for a brief review see e.g. Naud and Gerstner (2013)). However, these studies mainly quantified the similarity between experiment and simulations in terms of the spike-time coincidence measure Γ, but did not elaborate on matching multiple spectral statistics at once. Besides this and in contrast to our juxtacellular data, the parameter optimization in these studies is typically based on intracellularly recorded membrane-voltage traces that provide much more information to optimize the model parameters than this is the case for the bare sequence of spike times.

In contrast to these approaches, our aim is a quantitative match (by means of one parameter set per cell) of all statistics that are available from our analysis in ch.2.4. To this end, based on spike-train statistics, an optimization procedure is used to minimize a cost function that characterizes the similarity between experiment and simulation in terms of the mean firing rate, the spike-train–spike-train cross-spectra, the spike-train–stimulus cross-spectra, and the power spectra. However, we tested the quality of the performance also in terms of the coincidence factor between simulated and experimental spike trains, Γ_{se}, and the intrinsic reliability within experiments, Γ_{ee}, and simulations, Γ_{ss}. We did not split our dataset into one part for the optimization and one part to test the predictive power of the fit. However, because the coincidence between experimental and simulated spike times was not directly used in the optimization process, the resulting Γ-values can be thought to have some predictive meaning.

In order to successfully cope with this optimization task, we have to balance between two opposite strategies. On the one hand, we have to choose a neuron model that is as simple as possible in order to reduce the number of intrinsic parameters. On the other hand, the model should be able to capture the features of the real neuron whose dynamics we want to reproduce. If the model would be too complex, i.e. that it has many intrinsic parameters, it might be possible to capture many features of real neurons, but a successful parameter optimization would be unlikely due to the high dimensionality of the parameter space. Thus, the choice of the right model is an important task that determines whether or not the attempt to reproduce the data can work.

3.1. Motivation for the neuron model

One of the most simple neuron models that provides reasonable results is the one-compartment integrate-and-fire (IF) model which goes back to Lapicque (1907); Gerstein and Mandelbrot (1964); Stein (1965). The basic approximations in this model are: (i) Neglecting the spatial structure of the neuron and restricting the description to a zero dimensional point neuron. (ii) An artificial spiking mechanism that does not explicitly model the states of the ion channels that are involved in spike generation; instead an effective fire-and-reset rule is used. Such a model does not aim at a detailed biophysical description of the neuron, but assumes that it is not required to know all the underlying mechanisms to understand its functional properties (Abbott, 1999).

The first attempt of a quantitative description of experimentally measured neuronal statistics by using the most simple IF model, a perfect IF model, can be found in Gerstein and Mandelbrot (1964). Since that time IF models of different complexity have been developed and were intensively studied in various scenarios to investigate the effect of different mechanisms on the firing statistics, and to reproduce experimentally obtained results. These efforts resulted e.g. in work that could successfully match spike trains and voltage traces of individual neurons which have been stimulated with fluctuating currents in vitro (Badel et al., 2008; Jolivet et al., 2008; Hertäg et al., 2012). IF models also have been used to reproduce experimentally measured statistics like the inter-spike-interval distribution (Gerstein and Mandelbrot, 1964; Fisch et al., 2012), the inter-spike-interval correlations and spike-train power spectra (Bauermeister et al., 2013).

Due to the simplicity of IF models, it can be possible to analytically calculate some of their statistics. This has been e.g done in theoretical studies that aim at the calculation of transfer properties. These studies show that (under white Gaussian noise stimulation) the frequency-response amplitude has a lowpass shape with a cutoff frequency in the

range of the neurons firing rate (Brunel et al., 2001; Lindner and Schimansky-Geier, 2001; Fourcaud-Trocmé et al., 2003; Richardson, 2007). Furthermore, studies on the spectral coherence function revealed that the information transfer obeys a lowpass characteristic for these models (Stein et al., 1972; Vilela and Lindner, 2009b).

In comparison to these theoretical results, some experimental studies have reported quite different properties of the neuronal dynamics. In particular, the frequency-response amplitudes (or the vector strength) that have been measured in (Köndgen et al., 2008; Boucsein et al., 2009; Tchumatchenko et al., 2011; Ilin et al., 2013) show cutoff frequencies way above the firing rates of the neuron. Besides these studies, our data analysis in ch.2 reveals flat or increasing stimulus–spike-train cross-spectra (Fig.2.13), and no cutoff in the vector strength (Fig.2.16). The increase of the stimulus–spike-train cross-spectra qualitatively agrees with the increasing response amplitude for Purkinje cells that has been observed by Ostojic et al. (2015).

Also, our analysis reveals that the coherence does not possess a lowpass characteristic with a cutoff in the range of the firing rate, but reveals a sustained transmission of information at higher frequencies. These observations are in marked contrast to the properties that have been derived for the one-compartment IF models. We therefore have to conclude that one-compartment IF models do not seem to be compatible with a quantitative reproduction of our experimental results.

To come up with a model that accounts for the missing features that have been observed in experiments, but that still incorporates as much as possible of the simplicity of the IF framework, the simple models have to be extended in a suitable way. In terms of generating naturalistic voltage traces, the most sophisticated one-variable single-compartment-IF model is the exponential integrate-and-fire (EIF) model (Fourcaud-Trocmé et al., 2003; Badel et al., 2008). This model is given by

$$C_\mathrm{s}\frac{\mathrm{d}V_\mathrm{s}}{\mathrm{d}t} = -g_\mathrm{s}V_\mathrm{s} + g_\mathrm{s}\Delta_T e^{\frac{V_\mathrm{s}-V_\mathrm{Th}}{\Delta_T}} + I_\mathrm{soma} \tag{3.1}$$

and obeys the fire-and-reset mechanism: if $V(t) = V_\mathrm{Threshold}$, then $V(t) \to V_\mathrm{reset}$. Here, the voltage variable $V_\mathrm{s}(t)$ is a spatially independent variable and effectively describes the voltage at the spike generating zone. The membrane capacitance and the leak conductance are given by C_s and g_s respectively. The total inward current that enters the somatic compartment consists of I_soma and an exponential term that is supposed to account for the exponentially enhanced current influx that gives rise to the onset of an AP. The latter term is characterized by the spike slope factor, Δ_T, that gives the sharpness of the onset, and by the threshold value, V_Th, that determines the voltage at which the exponential

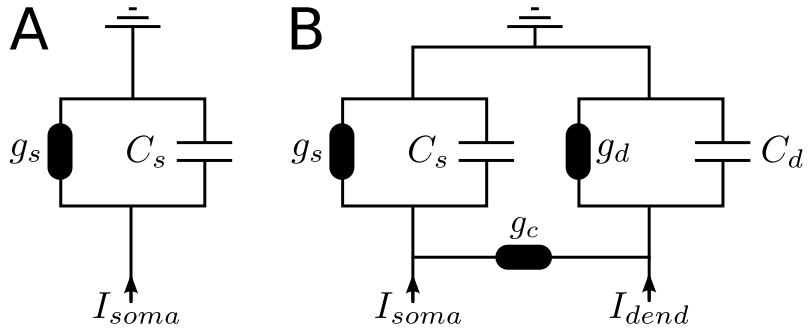

Figure 3.1.: Equivalent circuit for A) the one-compartment model and B) the two-compartment model.

term starts to dominate the equation and triggers an AP. An equivalent circuit of this model is given in Fig.3.1A.

An experimental and theoretical study by Bekkers (2011) revealed, that the subthreshold decay of the somatic voltage in response to a somatic applied current pulse is fast when the connection to the dendrite is strong while it becomes slower when the connection to the dendrite is pinched (see Fig.1 in Bekkers (2011)). This implies that the presence of the dendritic tree supports the transfer of high-frequency stimulus components. Besides this study, Eyal et al. (2014) and Ostojic et al. (2015) reported that the effect of the spatially distribution of the neuron, in particular the presence of a passive dendritic tree, can lead to filter properties that show enhanced support of high frequencies. Eyal et al. (2014) demonstrated by simulating a multi-compartment model with the software NEURON that the cutoff frequency of the vector strength is shifted towards higher frequencies with increasing dendritic load (i.e. the ratio of the dendritic and somatic size). Ostojic et al. (2015) showed analytically, and by simulations that a two-compartment-IF model can have an increasing response amplitude. Because of the pronounced high-frequency support that we found in our experiments, these considerations motivated us to incorporate a dendrite in our neuron model. The most simple treatment of the spatial structure that is imposed by the presence of a dendritic tree, is to attach an additional dendritic compartment to the somatic compartment (see Fig.3.1B). This results in a two-compartment model that is equivalent to that used in (Ostojic et al., 2015). In the following, this model will be introduced and compared to more complex models.

3.2. Two-compartment EIF model

The two-compartment EIF model consists of a somatic compartment that is equipped with a spiking mechanism and a purely passive dendritic compartment. Both compartments are connected via an ohmic conductance to allow for electro-tonic coupling. The differential equations for the two-compartment EIF model are given by

$$C_{\mathrm{s}}\frac{\mathrm{d}V_{\mathrm{s}}}{\mathrm{d}t} = -g_{\mathrm{s}}V_{\mathrm{s}} - g_{\mathrm{c}}(V_{\mathrm{s}} - V_{\mathrm{d}}) + g_{\mathrm{s}}\Delta_T e^{\frac{V_{\mathrm{s}}-V_{\mathrm{Th}}}{\Delta_T}} + I_{\mathrm{soma}}, \tag{3.2}$$

$$C_{\mathrm{d}}\frac{\mathrm{d}V_{\mathrm{d}}}{\mathrm{d}t} = -g_{\mathrm{d}}V_{\mathrm{d}} + g_{\mathrm{c}}(V_{\mathrm{s}} - V_{\mathrm{d}}) + I_{\mathrm{dend}}, \tag{3.3}$$

and a fire-and-reset rule that obeys

$$\text{If } V_{\mathrm{s}}(t) \geq X = 6V_{\mathrm{Th}} \text{ then } V_{\mathrm{s}}(t) \to X \text{ and } V_{\mathrm{s}}(t + \mathrm{d}t) \to 0. \tag{3.4}$$

Here, $V_{\mathrm{s}}(t)$ and $V_{\mathrm{d}}(t)$ are the somatic and dendritic membrane potentials. When the somatic voltage is large enough, i.e. $V_s(t) > V_{\mathrm{Th}}$, the exponential term dominates the dynamics and generates a fast voltage upstroke, the sharpness of which is defined by the spike slope factor Δ_T. Once this upstroke reaches a fixed threshold X, the fire-and-reset rule eq.(3.4) is applied. We first set the voltage to X and perform the reset to zero in the next time step. This is done to avoid numerical artifacts from too large exponentials and to yield constant AP height and comparable influence on the dendritic compartment for each AP (due to the passive coupling of somatic and dendritic compartment the somatic AP is also visible in the dendritic compartment). To keep the number of parameters as small as possible, and to investigate solely the influence of the spatial extension of the model, dendritic after-spike hyperpolarization as in Ostojic et al. (2015) is not taken into account. Instead, the dynamic of the dendritic compartment (eq.(3.3)) continues during the upstroke and the reset of the somatic compartment.

We assume that soma and dendrite have the same resting potentials. If the resting potentials would differ this would result in a constant current flow from one compartment to the other which is not physiological. Without loss of generality, we shifted the voltages to set the resting potential to zero (see reset rule in eq.(3.4)). The parameter C_{s} (C_{d}) is the somatic (dendritic) membrane capacitance, g_{s} (g_{d}) is the somatic (dendritic) membrane leak conductance, and g_{c} is the coupling conductance between the two compartments.

The currents $I_{\mathrm{soma}}(t)$ and $I_{\mathrm{dend}}(t)$ are the somatic and dendritic input currents that account for the experimentally injected stimulation current, the noise due to membrane channel fluctuations, and input from the surrounding presynaptic population. The somatic in-

put current $I_{\mathrm{soma}}(t) = I_{\mathrm{s}}(t)/\alpha + I_{\mathrm{noise,s}}(t)$ consists of two parts. First, the external stimulus, $I_s(t)$, that is evoked by the juxtacellular electrode and which is scaled by a dimensionless constant $\alpha > 1$. This rescaling is necessary because the somatic current, $I_{\mathrm{soma}}(t)$, enters in eq.(3.2) as if it was injected intracellularly. However, in our juxtacellular setting the electrode is extracellular, and therefore only a fraction of the stimulation current, $I_{\mathrm{s}}(t)$, enters the cell. Second, to account for the random fluctuations arising in the soma in vivo, we add white Gaussian noise, $I_{\mathrm{noise,s}}(t)$, with zero mean $\langle I_{\mathrm{noise,s}}(t)\rangle = 0$ and correlation function $\langle I_{\mathrm{noise,s}}(t) I_{\mathrm{noise,s}}(t')\rangle = 2D_s\delta(t-t')$. Here, the parameter D_s describes the intensity of the somatic noise. The dendritic current, $I_{\mathrm{dend}}(t) = I_{\mathrm{noise,d}}(t) + \mu_d$, accounts for the synaptic input that the dendrite receives. It consists of a constant base current, μ_d, and Gaussian white noise with zero mean $\langle I_{\mathrm{noise,d}}(t)\rangle = 0$ and $\langle I_{\mathrm{noise,d}}(t) I_{\mathrm{noise,d}}(t')\rangle = 2D_d\delta(t-t')$, where D_d is the dendritic noise intensity.

To effectively reduce the number of parameters, we divide eq.(3.2) by $g_{\mathrm{s}}\Delta_T$ and eq.(3.3) by $g_{\mathrm{d}}\Delta_T$ and measure the voltages in units of the spike slope factor, $V/\Delta_T \to V$. This leads to the dimensionless equations

$$\tau_{\mathrm{s}}\frac{\mathrm{d}V_{\mathrm{s}}}{\mathrm{d}t} = -V_{\mathrm{s}} - \frac{g_{\mathrm{c}}}{g_{\mathrm{s}}}(V_{\mathrm{s}} - V_{\mathrm{d}}) + e^{V_{\mathrm{s}}-V_{\mathrm{Th}}} + \frac{I_{\mathrm{s}} + \alpha I_{\mathrm{noise,s}}}{\alpha g_{\mathrm{s}}\Delta_T}, \tag{3.5}$$

$$\tau_{\mathrm{d}}\frac{\mathrm{d}V_{\mathrm{d}}}{\mathrm{d}t} = -V_{\mathrm{d}} + \frac{g_{\mathrm{c}}}{g_{\mathrm{d}}}(V_{\mathrm{s}} - V_{\mathrm{d}}) + \frac{I_{\mathrm{noise,d}} + \mu_d}{g_{\mathrm{d}}\Delta_T}. \tag{3.6}$$

Here, $\tau_{\mathrm{s}} = C_{\mathrm{s}}/g_{\mathrm{s}}$ and $\tau_{\mathrm{d}} = C_{\mathrm{d}}/g_{\mathrm{d}}$ are the somatic and dendritic membrane time constants of the isolated compartments. In total, this model involves nine intrinsic parameters that can be expressed by

$$\alpha g_{\mathrm{s}}\Delta_T,\ \tau_{\mathrm{s}},\ \tau_{\mathrm{d}},\ \frac{V_{Th}}{\Delta_T},\ \frac{g_{\mathrm{c}}}{g_{\mathrm{s}}},\ \frac{g_{\mathrm{c}}}{g_{\mathrm{d}}},\ \frac{\alpha^2 D_s}{(g_{\mathrm{s}}\Delta_T)^2},\ \frac{D_d}{(g_d\Delta_T)^2},\ \frac{\mu_d}{g_d\Delta_T}. \tag{3.7}$$

3.3. Is a two-compartment model sufficient to describe the dendritic influence?

It is natural to ask, if it is sufficient to describe the major effects of a complex dendritic structure, when taking the spatially extension of the neuron into account only by adding a single dendritic compartment to the soma. To elaborate on this question, we will have a look at the subthreshold dynamics of the two-compartment model (in particular its transfer properties) and compare it to models of various complexity, i.e. a one-compartment model, the multi-compartment model used by Eyal et al. (2014) to study the influence of the

dendrite on high-frequency transmission, and a soma attached to a semi-infinite chain of dendritic compartments.

In the subtheshold regime, the somatic voltage is smaller than the threshold (i.e. $V_\mathrm{s}(t) < V_\mathrm{Th}$) and no AP firing takes place. Therefore, in IF models the fire-and-reset mechanism can be neglected and for an EIF model also the exponential term (in eq.(3.1) and eq.(3.2)) can be assumed to be close to zero. Thus, the models simplify to purely linear systems of ordinary differential equations (in the case of the one-compartment model to a single equation rather than a system of equations). When we take the Fourier transform of the linearized equations, we can write the time derivative as multiplication by $i2\pi f$ and obtain a linear algebraic equation for $\tilde{V}_s(f)$ and $\tilde{I}_s(f)$. This equation is solved by

$$\tilde{\boldsymbol{V}}(f) = \boldsymbol{\chi}(f)\tilde{\boldsymbol{I}}(f). \tag{3.8}$$

Here, $\tilde{\boldsymbol{V}} = (\tilde{V}_s, \tilde{V}_d)$ and $\tilde{\boldsymbol{I}} = (\tilde{I}_s, \tilde{I}_d)$ are Fourier transformed somatic and dendritic voltages and input currents respectively. The elements, χ_{ij}, of the susceptibility matrix, $\boldsymbol{\chi}$, connect the inputs to the different compartments with the respective outputs (i and j either refer to the somatic [s] or dendritic [d] compartment).

Because in the full nonlinear equations the spike-generating mechanism acts on the somatic compartment, the somatic voltage dynamic determines the spike train that is generated by the model. Therefore, also in the simplified linear model we are most interested in the response of the somatic voltage, $V_\mathrm{s}(t)$, with respect to a somatic stimulation current, $I_s(t)$, that accounts for the juxtacellular input. Following eq.(3.8) these quantities are connected via $\tilde{V}_s(f) = \chi_{ss}(f)\tilde{I}_s(f)$, where the susceptibility $\chi_{ss}(f)$ is the respective entry of the matrix $\boldsymbol{\chi}(f)$ (here $\tilde{I}_d = 0$ was assumed). Because in our case the input, $I_s(t)$, is a current and the output, $V_\mathrm{s}(t)$, is a voltage, the susceptibility is also called impedance function, $\chi_{ss}(f) = Z_s(f)$. The frequency dependence of the impedance function characterizes the somatic subthreshold response of the model to certain Fourier components of the stimulus. For the two-compartment model this quantity has also been briefly discussed in Ostojic et al. (2015).

Two-compartment model – subthreshold impedance $Z_s^{\mathrm{two}}(f)$ The calculation of the somatic impedance function yields

$$Z_s^{\mathrm{two}}(f) = \frac{1}{g_s} \frac{1 + \frac{g_c}{g_d} + i2\pi\tau_d f}{\left(1 + \frac{g_c}{g_s} + i2\pi\tau_s f\right)\left(1 + \frac{g_c}{g_d} + i2\pi\tau_d f\right) - \frac{g_c^2}{g_s g_d}}. \tag{3.9}$$

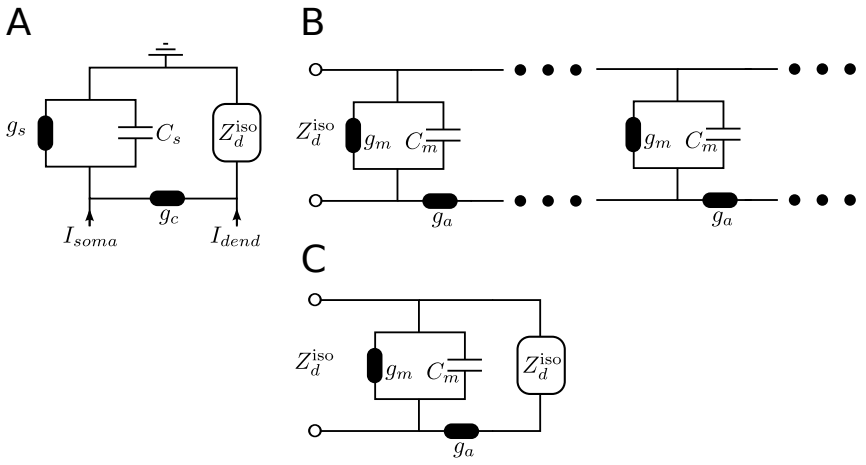

Figure 3.2.: Equivalent circuits for A) a compartment model with a dendritic load $Z_d^{\rm iso}$ attached to the somatic compartment, B) an isolated dendrite consisting of an infinite chain of compartments, C) an equivalent scheme to calculate the impedance Z_d of an infinite chain of compartments.

Isolated soma – subthreshold impedance $Z_s^{\rm iso}(f)$ In the limit of a vanishing dendrite, $g_c \to 0$, eq.(3.9) simplifies to the impedance of an isolated soma (i.e. a one-compartment model)

$$Z_s^{\rm iso}(f) = \frac{1}{g_s} \frac{1}{1 + i2\pi\tau_s f}. \tag{3.10}$$

Semi-infinite dendrite model – subthreshold impedance $Z_s^{\infty}(f)$ The impedance for a soma attached to a semi-infinite dendrite can be calculated according to the following scheme (see Fig.3.2 for illustration). We assume the impedance of the isolated semi-infinite dendrite to be $Z_d^{\rm iso}(f)$ (Fig.3.2B). Therefore, the impedance of a soma coupled to the dendrite via an ohmic coupling conductance g_c (Fig.3.2A) is given by

$$Z_s^{\infty}(f) = \frac{1}{g_s} \frac{1}{1 + i2\pi f\tau_s + \frac{1}{g_s} \frac{g_c}{1+g_c Z_d^{\rm iso}(f)}}. \tag{3.11}$$

Thus, the remaining task is to find an expression for the impedance of the isolated semi-infinite dendrite $Z_d^{\rm iso}(f)$. The equivalent circuit of this dendrite is given in Fig.3.2B and C. It consists of an infinite chain of compartments, where each compartment is described by an axial conductance g_a, a membrane resistance g_m and a capacitance C_m. Because the dendrite is assumed to be infinitely long it should not make a difference to add an extra

compartment and the impedance should stay the same (Fig.3.2C). Thus, we can write

$$Z_d^{\text{iso}}(f) = \frac{1}{g_m} \frac{1}{1 + i2\pi f\tau_d + \frac{1}{g_m} \frac{g_a}{1+g_a Z_d^{\text{iso}}(f)}}. \tag{3.12}$$

This expression yields a quadratic equation for $Z_d^{\text{iso}}(f)$ that is uniquely solvable under the restriction $\text{Re}(Z_d^{\text{iso}}(f)) \geq 0$

$$Z_d^{\text{iso}}(f) = \frac{1}{2g_a} \left(-1 + \sqrt{1 + 4\frac{g_a}{g_m} \frac{1}{1 + i2\pi f\tau_m}} \right). \tag{3.13}$$

Inserting eq.(3.13) in eq.(3.11) gives the expression for the somatic impedance.

Multicompartment model In principle, one could calculate the impedance for a model with a finite number of compartments by successively applying eq.(3.11). However, this would give a lengthy expression and is not demonstrated here. Instead, the impedance function for the multi-compartment model is calculated numerically. To this end, the model used by Eyal et al. (2014) has been implemented in NEURON and the impedance was defined as the ratio of the Fourier-transformed voltage, measured at the spike initiating zone, and the Fourier-transformed current that is injected in the soma. The model consists of 107 compartments [soma (1), axon (21+25) and dendrite (60)]. In particular, we refer to the case in Eyal et al. (2014) of an intermediate conductance load ($\rho = (G_{\text{dend}} + G_{\text{soma}})/(G_{\text{axon}}) = 190$) where G_{dend}, G_{soma} and G_{axon} are the inverse input resistances of the isolated compartments respectively. This dendrite has a length of 3 mm and a diameter of 5 µm (parameters as in Eyal et al. (2014) Fig.2 (gray curves)).

It is noteworthy that the description of the dendritic tree by a single cylinder is completely equivalent to directly treating a branched dendrite that fulfills certain constraints (Rall, 1962a,b). It was shown in Rall (1962b) that this equivalence e.g. holds true if the sum of the 3/2 power of the diameters of the daughter branches equals the 3/2 power of the diameter of the parent branch for all daughter branches:

$$\sum_k d_k^{\frac{3}{2}} = d_0^{\frac{3}{2}}.$$

Here, d_k is the diameter of the k-th daughter branch and d_0 is that of the parent branch. Interestingly, this $d^{3/2}$ law roughly agrees with experimentally measured branching diameters in motoneurons of cats (Rall, 2011). Therefore, the simple description of the dendrite by a single cylinder (known as equivalent cylinder) is much more general than it seems to

be on the first glance.

In order to test how well the subthreshold dynamics of the two-compartment model can match that of a more detailed dendritic description, the absolute value of the impedance function for the different models is plotted in Fig.3.3 over a wide frequency range. Here, the impedance of the multi-compartment model was calculated numerically for the parameters used by Eyal et al. (2014). The impedance of the two-compartment model and the infinite-dendrite model were fitted by minimizing the mean-square displacement to the multi-compartment impedance, using a downhill simplex algorithm (Nelder and Mead, 1965). The infinite-dendrite model performs slightly better, but both the two-compartment and the infinite-dendrite model show subthreshold filter properties that are close to that of the multi-compartment model up to 10 000 Hz.

To visualize the enhanced support of high frequencies due to the dendrite, also the impedance of a one-compartment model (with parameters as for the two-compartment model) that does not take the dendrite into account, is plotted as in Fig.3.3. The one-compartment impedance clearly fails to match that of the other models. In particular, the impedance of the one-compartment model is much larger for small frequencies. Hence, high-frequency filter characteristics (i.e. the transfer relative to that of low frequencies) can be achieved by reducing the support of low frequencies, which seems to be the case here. This observation can be better understood when we compare the subthreshold properties of the two-compartment model (i.e. eq.(3.9)) to that of the one-compartment model (eq.(3.9)) by applying approximations for different frequency regions.

Low frequencies: In the limit of low frequencies ($f \to 0$), one can neglect the capacitive influence and the impedance functions simplify to the so called somatic input-resistance, which yields for the two-compartment and the one-compartment model

$$Z_s^{\text{two}}(f \to 0) = \frac{1}{g_s} \frac{1 + \frac{g_c}{g_d}}{1 + \frac{g_c}{g_d} + \frac{g_c}{g_s}}, \tag{3.14}$$

$$Z_s^{\text{iso}}(f \to 0) = \frac{1}{g_s}. \tag{3.15}$$

Because the second factor in eq.(3.14) is smaller than one, the two-compartment response to slow stimuli is always reduced in comparison to that of the one-compartment model. This can be explained by a fraction of the current that leaks into the dendritic compartment and hence decreases the somatic response.

Intermediate frequencies, $g_c/(2\pi C_d) < f < g_c/(2\pi C_s)$: With increasing frequency the capacities of the somatic and dendritic compartment become more important. When we assume that the capacitance per surface area for soma and dendrite is roughly the same,

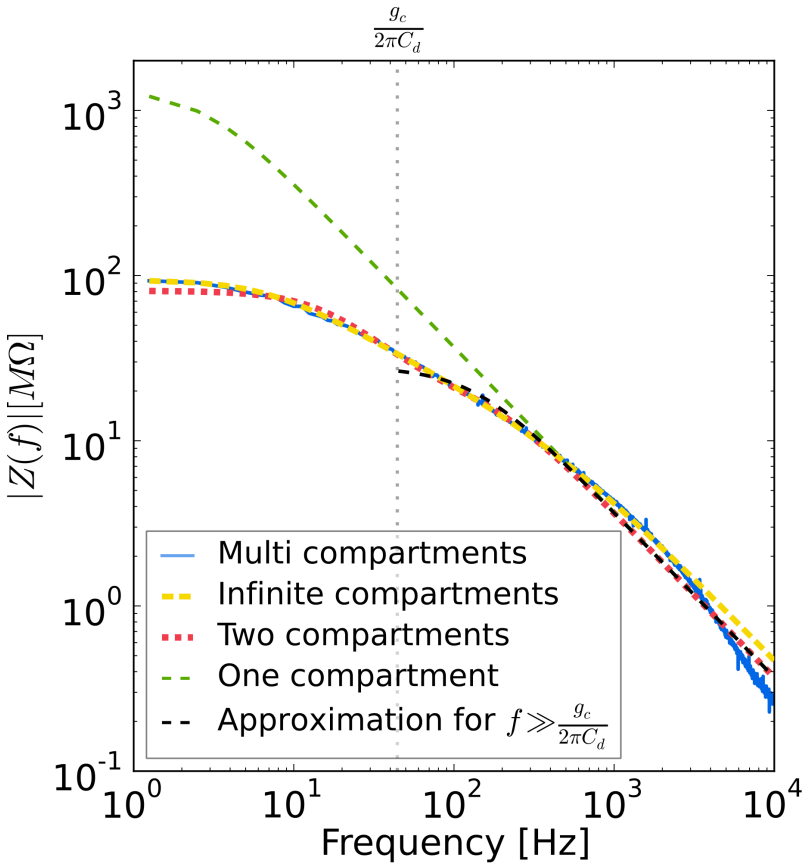

Figure 3.3.: Two-compartment model can match the subthreshold dynamics of models with more detailed dendrites. The subthreshold impedance function for the multi-compartment model used by Eyal et al. (2014) (solid blue) is well matched by the model with infinitely long dendrite (dashed yellow) and by the two-compartment model (dotted red). In contrast, the one-compartment model (dashed green) has an increased susceptibility at low frequencies. For intermediate and high frequencies the two-compartment model is well approximated by a one-compartment model with adapted membrane conductance (dashed black).

we find for the total capacitance that $C_d > C_s$. This is because the effective surface area of the dendritic compartment is expected to be larger than that of the somatic compartment. Therefore, the capacitive current in the dendritic compartment becomes large before this is the case in the somatic compartment. This allows us to define an intermediate frequency region, $g_c/(g_d 2\pi\tau_d) = g_c/(2\pi C_d) < f < g_c/(2\pi C_s) = g_c/(g_s 2\pi\tau_s)$, in which we perform the approximations $1 \ll \frac{g_c}{g_d}$ and $\frac{g_c}{g_d} \ll 2\pi\tau_d f$ to simplify eq.(3.9):

$$\begin{aligned} Z_s^{\text{two}}(f) &\approx \frac{1}{g_s} \frac{i2\pi\tau_d f}{(1+\frac{g_c}{g_s}+i2\pi\tau_s f)(i2\pi\tau_d f) - \frac{g_c^2}{g_s g_d}} \\ &= \frac{1}{g_s} \frac{i2\pi\tau_d f}{(1+i2\pi\tau_s f)(i2\pi\tau_d f) + \frac{g_c}{g_s}(i2\pi\tau_d f - \frac{g_c}{g_d})} \\ &\approx \frac{1}{g_s} \frac{i2\pi\tau_d f}{(1+i2\pi\tau_s f)(i2\pi\tau_d f) + \frac{g_c}{g_s}(i2\pi\tau_d f)} \\ &= \frac{1}{g_s} \frac{1}{1+\frac{g_c}{g_s}+i2\pi\tau_s f} = \frac{1}{g_s + g_c + i2\pi C_s f}. \end{aligned} \tag{3.16}$$

This equation corresponds to an equivalent circuit in which the dendritic compartment is grounded. Therefore, in this region the two-compartment model behaves like a one-compartment model with increased membrane conductance $g_s + g_c$, which results in a decreased membrane time constant $C_s/(g_s + g_c)$. When comparing eq.(3.16) to eq.(3.10), we find that the absolute value of the impedance for the two-compartment model is smaller than for the one-compartment model (see Fig.3.3 at intermediate frequencies). However, also the relative decay w.r.t. the value at small frequencies (i.e. the strength of the decrease of $Z(f)$ normalized by $Z(0)$) is smaller for the two-compartment model and thus the dampening with frequency is less pronounced. The expression eq.(3.16) is plotted in Fig.3.3 for $f > g_c/(2\pi C_d)$ and shows a qualitative agreement with the full impedance $Z_s^{\text{two}}(f)$ in this region.

A different approximation for the impedance at intermediate frequencies can be found in Ostojic et al. (2015). Here, the authors not only assume the dendritic compartment to be grounded, but also neglect the influence of the somatic conductance and capacitance which results in $Z_s^{\text{two}}(f) \approx 1/g_c$. This approximation more strikingly points out that the decrease of the impedance function is flattened, but when looking at the full impedance in Fig.3.3, a constant seems to be a very rough approximation.

High frequencies, $f > g_c/(2\pi C_s)$: For even larger frequencies we can further approxi-

mate $1 \ll \frac{g_c}{g_s} \ll 2\pi\tau_s f$, which yields

$$Z_s^{\text{two}}(f \to \infty) = \frac{1}{g_s}\frac{1}{i2\pi\tau_s f} = \frac{1}{i2\pi C_s f}. \tag{3.17}$$

This is the same expression as the high-frequency limit of the one-compartment model, and here solely the somatic capacitance determines the dynamics.

In summary, we can conclude that the somatic subthreshold dynamics of the two-compartment model show a suppressed support of low frequencies due to the presence of the dendritic compartment. Therefore, in comparison to the one-compartment model, and normalized to the transmission at low frequencies, the two-compartment model has an enhanced support of high frequencies.

The ability of the two-compartment model to match the dynamics of more complex models in the linearized (subthreshold) regime can be regarded as a necessary condition to have similar properties as the full nonlinear models. However, this is not a strict argument because the nonlinearity (the fire-and-reset mechanism and the exponential term) can introduce effects to the dynamics that are not obvious for the linearized case.

3.4. Estimating a plausible range for the two-compartment parameters

Because the two-compartment IF model is an abstract model, some considerations about the biophysical meaning of the involved parameters are needed to estimate a plausible range for these parameter values. However, one should note that both the somatic and the dendritic compartment are effective descriptions of the respective parts of the neuron and likewise are the values of the model parameters only effective. For example, when assuming the same density for leaky ion channels in the soma and the dendrite both parts would have the same conductivity (i.e. conductance per surface area). Thus, the ratio of the total conductances should equal the ratio of the respective surface areas $g_\mathrm{s}/g_\mathrm{d} = A_\mathrm{s}/A_\mathrm{d}$. This, however, is not always true as e.g. becomes clear when thinking of the two-compartment model as an effective description of a neuron with infinitely long dendrite. This dendrite would have an infinite surface area, A_d, but the two-compartment parameter g_d would surely be finite. Still, the effective parameters are related to their biophysical counterparts, and thus plausible parameter regions can be estimated. To this end, the approximations that are involved when deriving the equations for the two-compartment model have to be reviewed in more detail.

3.4.1. Approximations that lead to the two-compartment model

In ch.3.2, the input from the synaptic background was introduced as additive white Gaussian noise. This is a common assumption that strongly simplifies the mathematical description. This noise term is characterized by a mean value and a noise intensity for which the relation to biophysical parameters is not obvious. To understand this relation the approximations that lead to the white noise description are briefly reviewed in the following. A detailed discussion of this calculations is given in the lecture notes by Lindner and Voronenko (2005). A related approach can also be found in Richardson and Gerstner (2005).

When the synaptic input is treated in a more biophysical motivated (although still phenomenological) way, it can be described as a change of the membrane conductivity. For our two-compartment model this would mean that the dendritic compartment (eq.(3.3)), which is the compartment that receives the synaptic input, would be described according to

$$C_d \frac{\mathrm{d}V_\mathrm{d}}{\mathrm{d}t} = -g_d(V_\mathrm{d} - E_l) + g_E(t)(E_E - V_\mathrm{d}) + g_I(t)(E_I - V_\mathrm{d}) + g_c(V_\mathrm{s} - V_\mathrm{d}), \tag{3.18}$$

where g_d is the constant dendritic leak conductance, E_l is the reversal potential of the leak current, and g_c is still the coupling conductance to the somatic compartment. The opening and closing of the additional membrane conductances that account for the excitatory and inhibitory ion-channels is described by $g_E(t)$ and $g_I(t)$ respectively (the index denotes either the excitatory $[E]$ or the inhibitory $[I]$ case). The synaptic current depends on the difference between the dendritic voltage and the respective reversal potentials that are given by E_E and E_I.

The time course of the synaptic conductances can be experimentally estimated by measuring the postsynaptic current in voltage clamp mode at different clamping potentials. Typically $g_{E,I}(t)$ has a fast upstroke and a slower exponential decay that can be well approximated by a single exponential with decay time $\tau_{E,I}$:

$$g_{E,I}(t) = \sum_i a_i^{E,I} e^{\frac{t-t_i}{\tau_{E,I}}} \Theta(t - t_i).$$

Here, t_i are the times of synaptic events and $a_i^{E,I}$ is the synaptic weight that defines the amplitude of the postsynaptic current peak. This description for the conductances is

equivalent to writing

$$\tau_{E,I}\frac{\mathrm{d}g_{E,I}}{\mathrm{d}t} = -g_{E,I} + \tau_{E,I}\sum_{i=1}^{N_{E,I}} a_i^{E,I}\delta(t-t_i), \tag{3.19}$$

where N_E and N_I are the total numbers of APs that the neuron receives via excitatory and inhibitory synapses and thus this implies the assumption that all synapses are lumped together in this compartment.

When we assume N_E (N_I) to be a large number that the synaptic weights a_i^E (a_i^I) are uncorrelated and independent and that the spike times are distributed with Poissonian statistic, the sum over the delta functions in eq.(3.19) can be replaced by a constant input and additional white Gaussian noise (this is known as diffusion approximation (Ricciardi, 1977; Lánský and Lánská, 1987)).

At this point the conductance $g_{E,I}$ is still a filtered version of the white noise, and therefore would be described by colored noise with correlation time $\tau_{E,I}$. When we further assume that $\tau_{E,I}$ is small against the time scale of the membrane dynamic, we can neglect the left side of eq.(3.19) and $g_{E,I}$ becomes white Gaussian noise. However, because the synaptic noise still effects the conductances it enters the voltage dynamic in eq.(3.18) as multiplicative noise. We further assume that the noise is small and that it causes the fluctuations in the voltage, we can conclude that the product given by the deviation of the conductances from their mean value times the deviation of the voltage from its mean value can be neglected. With these approximations, we obtain an equation in which the noise enters as additive noise

$$\begin{aligned} C_d\frac{\mathrm{d}V_\mathrm{d}}{\mathrm{d}t} =& -g_d(V_\mathrm{d}-E_l) + R_E\tau_E\langle a_E\rangle(E_E-V_\mathrm{d}) + R_I\tau_I\langle a_I\rangle(E_I-V_\mathrm{d}) \\ &+ g_c(V_\mathrm{s}-V_\mathrm{d}) + \sqrt{R_E\tau_E^2\langle a_E^2\rangle(E_E-E_0)^2 + R_I\tau_I^2\langle a_I^2\rangle(E_I-E_0)^2}\xi(t). \end{aligned} \tag{3.20}$$

Here, R_E and R_I are the total rates of excitatory and inhibitory synaptic inputs and $\langle a_{E,I}\rangle(E_{E,I}-V_d)$ is the amplitude of a single postsynaptic current for excitatory and inhibitory synapses respectively.

When we look at the terms that account for the mean current which enters the cell due to the synaptic input,

$$\mu_\mathrm{d}(V_\mathrm{d}) = R_E\tau_E\langle a_E\rangle(E_E-V_\mathrm{d}) + R_I\tau_I\langle a_I\rangle(E_I-V_\mathrm{d}), \tag{3.21}$$

we see that this expression depends on the actual value of the voltage. Thus, typically

all terms in eq.(3.20) that are proportional to V_d are lumped together and an effective leak conductance, $g_0 = g_d + R_E\tau_E \langle a_E\rangle + R_I\tau_I \langle a_I\rangle = g_d + \langle g_E\rangle + \langle g_I\rangle$, and an effective reversal potential, $E_0 = (g_d E_l + \langle g_E\rangle E_E + \langle g_I\rangle E_I)/(g_d + \langle g_E\rangle + \langle g_I\rangle)$, are defined. However, these parameters depend on the mean synaptic activity and therefore they are not representative for conductances or leak potentials that are measured in vitro. Thus, also the membrane time constant defined as $\tau_m = C_d/g_0$ can strongly depend on the synaptic activity. For a related discussion about this issues see e.g. Koch et al. (1996). To avoid this problem, our approach is to approximate the mean synaptic current $\mu_\mathrm{d}(V_\mathrm{d})$ by a constant that is independent of V_d. So we can keep the remaining membrane parameters independent of the synaptic activity, such that they can be estimated by values from in vitro measurements.

The synaptic reversal potentials are typically around $E_E \approx 0\,\mathrm{mV}$ (Coombs et al., 1955; Purves, 2004) and $E_I \approx -60\,\mathrm{mV}$ (Ferster and Jagadeesh, 1992; Takahashi, 1992; Purves, 2004). Therefore, E_I is close to what is used in most voltage clamp experiments to measure excitatory post synaptic currents (EPSCs). We assume that the membrane voltage is on average in the middle of E_E and E_I, which leads to: $(E_E - V_\mathrm{d}) = -(E_I - V_\mathrm{d}) \approx 0.5\,(E_E - V_\mathrm{clamp})$. We further assume that the amplitude for inhibitory postsynaptic currents (IPSCs) and for excitatory postsynaptic currents (EPSCs) is roughly the same (with opposite sign), and that the r'th part of the total synaptic input rate, $R_\mathrm{all} = R_E + R_I$, is excitatory while the (1-r)'th part is inhibitory. This simplifies eq.(3.21) to an expression for the mean synaptic input current that is independent of the actual voltage

$$\mu_\mathrm{d} \approx R_\mathrm{all}\tau_E \frac{\langle a_E\rangle\,(E_E - V_\mathrm{clamp})}{2}(2r-1). \tag{3.22}$$

With the same assumptions $(E_E - E_0)^2 \approx (E_I - E_0)^2 \approx (0.5(E_E - V_\mathrm{clamped}))^2$ the noise intensity can be approximated as

$$D_d = \frac{1}{8} R_\mathrm{all}\tau_E^2 \left\langle a_E^2\right\rangle (E_E - V_\mathrm{clamped})^2. \tag{3.23}$$

Insertion into eq.(3.20) reduces the equation to

$$C_d\frac{\mathrm{d}V_\mathrm{d}}{\mathrm{d}t} = -\,g_d(V_\mathrm{d} - E_l) + g_c(V_\mathrm{s} - V_\mathrm{d}) + \mu_\mathrm{d} + \sqrt{2D_d}\xi(t) \tag{3.24}$$

which has the form of the equation used to describe the dendritic compartment in the two-compartment model (eq.(3.3)).

3.4.2. Parameter estimates

The above considerations enable us to estimate the order of magnitude for the parameters of the dimensionless two-compartment model (eq.(3.7)). However, making estimates is further complicated due to the fact that some of the biophysical quantities measured in experiment already vary in a wide range. The values that have been e.g. measured for the resistivity of the cell membrane ρ_m vary from $8000\,\Omega\text{cm}^2$ (Connors et al., 1982) up to $20\,000\,\Omega\text{cm}^2$ and $100\,000\,\Omega\text{cm}^2$ (Koch, 1999). In contrast, experimentally measured values for the capacitance per surface area yield typically similar values and are reported in the range of $0.5\,\mu\text{Fcm}^{-2}$ to $1\,\mu\text{Fcm}^{-2}$ (Solsona et al., 1998; Koch, 1999; Gentet et al., 2000).

Estimating $\alpha g_s \Delta_T$ To estimate the range for this model parameter, we have to estimate α, g_s and Δ_T separately. When comparing the amount of current that is usually needed for intracellular recording (hundreds of pA) to the amount of current that is needed in juxtacellular experiments (a couple of nA, see e.g. Houweling et al. (2010)), we can conclude that roughly the tenth part of the current enters the cell. We therefore assume here that $\alpha \approx 10$.

An estimate of g_s can be calculated from $g_s = A_s/\rho_m$, where ρ_m it the specific membrane resistivity and A_s is the surface area of the somatic compartment. Values for ρ_m vary widely across the literature ($\rho_m \approx 10^4 - 10^5\,\Omega\text{cm}^2$) (Connors et al., 1982; Koch, 1999). The surface area A_s can be estimated as the surface of a sphere with radius r_s. The somatic diameter of a pyramidal neuron typically is in the order of tens of microns. With $r_s \approx 20\,\mu\text{m}$ we get $A_s \approx 4\pi r_s^2 \approx 5000\,\mu\text{m}^2$. These values yield $g_s \approx 0.5 - 5\,\text{nS}$ which is roughly consistent with the values that have been found for this parameter by Bekkers (2011) (0.8 nS) and (Ostojic et al., 2015) (0.1 nS) for Purkinje cells.

Recently, Harrison et al. (2015) have published parameter estimates for the single compartment EIF model, fitted on pyramidal neurons in vitro. They present parameter distributions for pyramidal neurons from various cortical areas. The values they report have been achieved by fitting a one-compartment EIF model to intracellular measured voltage traces. In particular, here we refer to their estimate of the spike slope factor Δ_T. Harrison et al. (2015) report the distribution for Δ_T as a log normal distribution with mean and standard deviation

$$\langle \Delta_T \rangle = 1.34, \quad \sigma(\Delta_T) = 0.55. \tag{3.25}$$

To find an approximation for the upper bound of a reasonable parameter range, we use the mean plus the standard deviation as estimate for Δ_T and calculate $\alpha g_s \Delta_T \approx 95\,\text{pA}$.

Estimating the time constants τ_s, τ_d When defining the membrane time constant as a passive property of the neurons membrane, it is given by the membrane capacitance per surface area times the specific resistance of this area, $\tau_m = c_m \rho_m$. The value for the membrane capacitance is relatively reliable measured among authors and usually ranges in between $0.8 - 1.2\,\mu\mathrm{F/cm}^2$ (Solsona et al., 1998; Koch, 1999; Gentet et al., 2000). With these values and the values for ρ_m (see above), we can roughly estimate τ_m and get values in the range from 8 ms to 120 ms which is consistent with the range given by Koch et al. (1996).

One has to be cautious when interpreting this time constant. As becomes apparent from the definition, τ_m is a property of the membrane that only corresponds to the decay time of the voltage if the neuron would be an isolated iso-potential soma (Rall, 1969). This would e.g. correspond to the case that is described by a one-compartment IF model, where the total injected current would leak through the somatic membrane. In fact, a real neuron is not a single iso-potential soma and a large fraction of the injected current does not leak through the somatic membrane but is spread out into the other parts of the neuron (e.g. into the dendritic tree) (Rall, 1959, 1969; Koch et al., 1996; Koch, 1999). Thus, the decay time is subject to the influence of the neurons geometry and the passive membrane time constant is an upper bound for the voltage decay time (Rall, 1969; Koch et al., 1996). Due to the two-compartment structure of our model, this geometric influence is already partially included in the model structure and must not be completely described by the choice of the effective time constants. Therefore, our parameter τ_s and τ_d are more linked to the passive membrane time τ_m, than they are to the decay time of one-compartment models.

In the literature e.g. Ostojic et al. (2015) and Bekkers (2011) use a two-compartment model to simulate the dynamics of Purkinje cells. From the parameters given in Ostojic et al. (2015) we can calculate $\tau_s = 200\,\mathrm{ms}$, and from Bekkers (2011) we get $\tau_s \approx 50\,\mathrm{ms}$ for the somatic compartment. For the dendritic compartment both references use $\tau_d \approx 200\,\mathrm{ms}$. These values agree with the interpretation that these parameters are more similar to the passive membrane time constant than to the voltage response time, the value of which would be smaller. We restricted ourself to $\tau_s < 100\,\mathrm{ms}$, $\tau_d < 100\,\mathrm{ms}$.

Estimating V_{Th}/Δ_T In eq.(3.2) and eq.(3.3), we shifted the membrane potential by subtracting the leak potential. Therefore, our threshold parameter, V_{Th}, is given by the distance between real threshold, V_{th}, and leak potential, E_l. The study by Harrison et al. (2015) reports parameter estimates for single-compartment EIF models for pyramidal cells from various cortical areas. They measure the difference between leak and threshold

potential and report a gaussian distribution with mean and standard deviation given by

$$\langle V_{th} - E_l \rangle = 29.8\,\mathrm{mV}, \quad \sigma(V_{th} - E_l) = 4.16\,\mathrm{mV}. \tag{3.26}$$

With a small estimate for the spike slope factor, $\Delta_T \approx 0.5\,\mathrm{mV}$, we can set $V_{\mathrm{Th}}/\Delta_T = 80$ as upper limit for this parameter.

Estimating g_c/g_s and g_c/g_d As already mentioned, in the simplified two-compartment model the parameters have to be seen as effective parameters. Thus, to estimate the range of g_c/g_d and g_c/g_s we compare the dendritic load that the single dendritic compartment imposes on the soma to the load that has been used by other authors and that was found for complex dendrites.

In Rall (1959), the dendritic load ρ is defined as the ratio of the complete neurons input conductance and the input conductance of an isolated soma. Equivalently, we can define the dendritic load for our two-compartment model. The input resistance of the isolated somatic compartment is simply $1/g_s$ (eq.(3.15)), and therefore the input conductance (i.e. the inverse input resistance) is g_s. The input resistance of the full two-compartment model is given by eq.(3.14). This leads to

$$\rho = 1 + \frac{g_c}{g_s} \frac{1}{1 + \frac{g_c}{g_d}}. \tag{3.27}$$

Taking the limit of infinite intracellular conductivity yields $\rho_\infty = \lim_{g_c \to \infty} \rho = (g_s + g_d)/g_s = 1 + g_d/g_s$. This is an upper bound for ρ that only depends on the ratio of the effective dendritic membrane conductance and the somatic membrane conductance. In particular, it does not depend on the internal resistivity which is difficult to measure (Stuart and Spruston, 1998; Antic, 2003; Golding et al., 2005; Bekkers, 2011).

When we assume g_c to be finite, we can ask in which range the ratio g_c/g_s must be to account for the fraction $x \in [0, 1]$ of the maximal possible conductance load ρ_∞. We therefore insert $x\rho_\infty$ in the left hand side of eq.(3.27) and solve the equation for g_c/g_s. With the expression for ρ_∞ this results in

$$\frac{g_c}{g_s} = \frac{g_d}{g_s} \frac{1 - x(1 + \frac{g_d}{g_s})}{(x - 1)\left(1 + \frac{g_d}{g_s}\right)}. \tag{3.28}$$

This expression is plotted in Fig.3.4 for three different values of g_d/g_s that have been reported by other authors. i) In Bekkers (2011) the subthreshold dynamics of the two-compartment model is fitted to the subthreshold dynamics of a Purkinje cell, which results

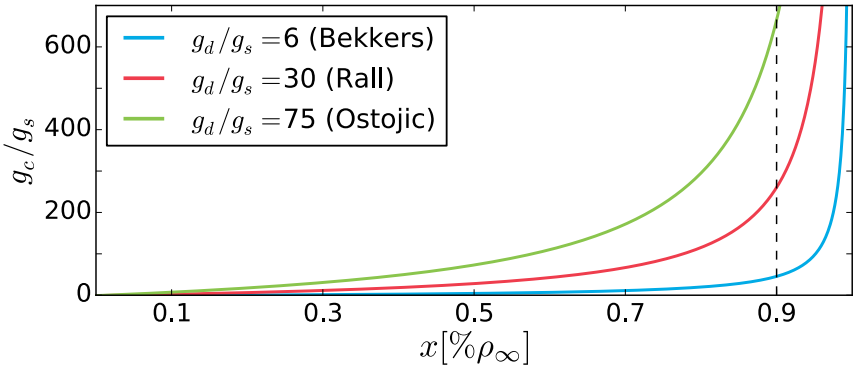

Figure 3.4.: The ratio g_c/g_s as a function of the percentage x of the dendritic load ρ_∞ for infinite intracellular conductance g_c. The different colors correspond to the ratios of g_d/g_s reported by different authors. For $x \to 1$ the curves diverge since this is the case where $g_c \to \infty$. For $x = 0.9$ (indicated by the dashed vertical line) the curves give us estimates of the ratio g_c/g_s that is necessary to yield the dendritic load $\rho = 0.9\rho_\infty$ (for a given ratio g_d/g_s).

in ratio $g_d/g_s \approx 6$. ii) In contrast to this, Ostojic et al. (2015) finds $g_d/g_s \approx 75$ which is more than a factor of ten larger. These fits would yield $\rho_\infty = 7$ and $\rho_\infty = 76$ respectively. iii) The values of the dendritic load calculated by Rall (1959) are in the order of $\rho \in (8, 47)$ and lie in between those found by Bekkers (2011) and Ostojic et al. (2015). We assume $g_d/g_s \approx \rho = 30$ to account for values from this reference.

In Fig.3.4, we can see that g_c/g_s increases with increasing g_d/g_s (different curves). For $x = 0.9$, which corresponds to 90% of the maximal possible dendritic load (for the particular choice of g_d/g_s), we find $g_c/g_s \approx 45$ (Bekkers, 2011), $g_c/g_s \approx 260$ (Rall, 1959) and $g_c/g_s \approx 665$ (Ostojic et al., 2015) for the three different cases respectively.

Because we deal with pyramidal cells that have a significantly smaller dendritic tree than Purkinje cells, we assume that $g_c/g_s = 600$ should be a sufficient large estimate for the upper bound for this parameter.

With the lowest estimate for $g_d/g_s = 6$ and

$$\frac{g_c}{g_d} = \frac{g_c}{g_s}\frac{g_s}{g_d}, \tag{3.29}$$

this yields the upper bound for $g_c/g_d = 100$.

As a proof of concept, we can estimate the conductance g_c as the conductance of a

cylinder with diameter d and length L.

$$g_c = \frac{\pi d^2}{\rho_i 4L}. \tag{3.30}$$

When we insert the expression for the electrotonic length constant $L = \sqrt{(\rho_m/\rho_i)(d/4)}$ as derived by Rall (1977), we obtain

$$g_c = \frac{\pi}{2}\sqrt{\frac{d^3}{\rho_i \rho_m}}. \tag{3.31}$$

With the resistivity of the intracellular fluid, $\rho_i = 100\,\Omega\text{cm}$ (Koch, 1999; Eyal et al., 2014), the dendritic diameter $d = 4\,\mu\text{m}$, and an intermediate membrane resistivity $\rho_m = 50\,000\,\Omega\text{cm}^2$, this estimate yields $g_c \approx 177\,\text{nS}$. Together with the above estimate of the somatic conductance, g_s, this results in the conductance ratio $g_c/g_s \approx 35$ to 355 and agrees with the range estimated above.

Estimating the noise strength D_d and the mean background activity μ_d For in vitro experiments, typical values for the EPSC of a single synaptic impulse can be found in the literature. They have a peak height ranging from a few to a few hundreds of pA and decay constants typically ranging from 2 ms to 5 ms (Hestrin et al., 1990; Silver et al., 1992; Hestrin, 1993; Feldmeyer et al., 2002; Gonzalez-Islas and Hablitz, 2003; Benedetti et al., 2013; Joshi et al., 2015). To estimate an upper bound for our noise parameters (μ_d and D_d), we assume the decay time as $\tau_E \approx 5\,\text{ms}$ and the EPSC amplitude as $\langle a_E \rangle\,(E_E - V_{\text{clamped}}) \approx 200\,\text{pA}$. We further assume that the average input rate is $R_{\text{all}} = 2000\,\text{Hz}$. This corresponds e.g. to a neuron that has 2000 input synapses with an average input rate of 1 Hz per synapse. We also assume that roughly 75% of the synaptic input is excitatory while 25% are inhibitory (Koch, 1999). With these numbers and the approximation $\langle a_E^2 \rangle \approx \langle a_E \rangle^2$ we yield from eq.(3.22) and eq.(3.23)

$$\mu_d = 5000\,\text{pA}, \tag{3.32}$$

$$D_d = 250\,\text{pA}^2\text{s}. \tag{3.33}$$

With the lower estimates for $g_d = 6g_s = 3\,\text{nS}$ and $\Delta_T = 0.5\,\text{mV}$, we calculate the upper bound for $\frac{\mu_d}{g_d \Delta_T} \approx 3333$ and that for $\frac{D_d}{(g_d \Delta_T)^2} = 111$.

3.5. Parameter optimization

After the model has been specified and estimates for a plausible parameter range are defined, the parameters need to be optimized in order to reproduce the particular experimental results. To this end, we define a cost function, $f_{\text{cost}}(\mathbf{p})$, that quantifies the model performance and assigns a scalar to each set $\mathbf{p} \in \mathbb{R}^{N_{\text{par}}}$ of independent parameter values, where N_{par} is the dimension of the parameter space. To optimize the value of this cost function, we use an optimization strategy that iteratively varies the parameters and minimizes $f_{\text{cost}}(\mathbf{p})$. In the following, the cost function and the optimization procedure are introduced in detail.

3.5.1. The cost function

To formulate the optimization as minimization problem, the cost function needs to have a global minimum at the optimal parameter values. In our case this is achieved by constructing the cost function as

$$f_{\text{cost}}(\mathbf{p}) = \sum_i \frac{\|\Phi_i^{\text{exp}} - \Phi_i^{\text{sim}}(\mathbf{p})\|_{f_F}}{\|\Phi_i^{\text{exp}}\|_{f_F}}, \tag{3.34}$$

where Φ_i is a measurable quantity that should be optimized for. The superscript refers either to the experimental (exp) or the simulated data (sim). In the numerator of eq.(3.34), the difference between the experimental and the simulated dataset is given for each measure Φ_i. Due to the normalization by $\|\Phi_i^{\text{exp}}\|$ (denominator) different measures become comparable.

We choose four measures, Φ_i, that are given by: i) the power spectrum, $\Phi_1(f) = S_{xx}(f)$, ii) the spike-train–spike-train cross-spectrum, $\Phi_2(f) = S_{x_i x_j}(f)$, iii) the stimulus–spike-train cross-spectrum, $\Phi_3(f) = S_{sx}(f)$, iv) and the mean firing rate, $\Phi_4 = r$. Because the firing rate is a scalar quantity the norm that appears in eq.(3.34) can be reduced to the absolute value. In contrast, $\Phi_1(f)$, $\Phi_2(f)$ and $\Phi_3(f)$ are frequency-dependent quantities, and therefore a norm that assigns a scalar value to each term in eq.(3.34) has to be defined. We use the area under the absolute value of the respective function up to a frequency f_F as definition of the norm (we choose $f_F = 1.5 f_c$)

$$\|\Phi_i\|_{f_F} = \int_0^{f_F} |\Phi_i(f)| \, \mathrm{d}f. \tag{3.35}$$

Therefore, the total cost function is given by

$$f_{\text{cost}}(\mathbf{p}) = \frac{\|S_{xx}^{\text{exp}} - S_{xx}^{\text{sim}}\|_{f_F}}{\|S_{xx}^{\text{exp}}\|_{f_F}} + \frac{\|S_{x_i x_j}^{\text{exp}} - S_{x_i x_j}^{\text{sim}}\|_{f_F}}{\|S_{x_i x_j}^{\text{exp}}\|_{f_F}} \tag{3.36}$$

$$+ \frac{\|S_{sx}^{\text{exp}} - S_{sx}^{\text{sim}}\|_{f_F}}{\|S_{sx}^{\text{exp}}\|_{f_F}} + \frac{|r^{\text{exp}} - r^{\text{sim}}|}{r^{\text{exp}}}. \tag{3.37}$$

By construction, this cost function has a minimum with $f_{\text{cost}}(\mathbf{p}) = 0$ for parameters that lead to $\Phi_i^{\text{sim}}(\mathbf{p}) = \Phi_i^{\text{exp}}$ for all i, and fulfills $f_{\text{cost}}(\mathbf{p}) > 0$ for all other parameters. However, more details about the shape of $f_{\text{cost}}(\mathbf{p})$ remain unknown. In particular, it is not clear whether the cost function is unimodal or if several local minima exist (which is a likely case). To take into account that physiological parameter values are only plausible within a certain range (as explained in ch.3.4), we added penalties to the cost function whenever a parameter p_j passes the corresponding boundary p_j^{b}. Each time this happens the value of the cost function is increased by $10 + (p_j - p_j^{\text{b}})^2/(p_j^{\text{b}})^2$.

3.5.2. The optimization strategy

In order to find the best parameter values, the choice of the optimization strategy is a crucial point. In particular, depending on the properties of the 'energy surface' (i.e. the hyper plane given by the values of the cost function in the parameter space) the use of some optimization strategies might be natural and expedient, while others are inappropriate. For continuous differentiable cost functions the usage of optimization schemes like gradient-decent methods might be the first choice. Typically, such methods can be applied to find local minima or to perform an optimization on an unimodal cost function, while they are not suitable for searching global minima on multimodal cost functions.

Because in our case the calculation of the cost function is based on spike-train statistics (and therefore on point processes), we cannot expect that an arbitrary small parameter variation results in an arbitrary small change of the objective function and consequently $f_{\text{cost}}(\mathbf{p})$ is not continuously differentiable. Also, we cannot expect that the cost function is unimodal, but it is likely that several local minima exist. Besides this, the dynamics of our model is subject to noise, and therefore multiple evaluations of the cost function can lead to variations in the results, even if the same parameter values have been used again. Thus, the optimization algorithm has to work on a noisy surface which makes it even more difficult to perform an optimization.

A class of optimization algorithms that can deal with non differentiable cost functions are evolutionary algorithms. A popular state of the art algorithm of this class is

the covariance-matrix adaptation evolution-strategy algorithm (CMA-ES) proposed by Hansen and Ostermeier (2001). We will particularly concentrate on the variant that has been extended for large population sizes (i.e. the number of solutions per iteration) by Hansen et al. (2003). The CMA-ES is well suited for non-continuous, noisy and multi-modal problems and is therefore feasible for global optimization (Hansen and Kern, 2004; Auger et al., 2009).

In the following, the basic principles of the CMA-ES are presented. More detailed information is given in the respective literature (e.g. (Ostermeier et al., 1994; Hansen and Ostermeier, 2001; Hansen et al., 2003; Hansen, 2006; Chotard et al., 2012)). The source code for the algorithm can be found in Hansen and Baudis (2008 - 2015).

In each iteration i, the CMA-ES draws an ensemble of N_{pop} points in the parameter space from a multivariate normal distribution

$$\mathbf{p}_i^{(k)} \sim \mathcal{N}(\mathbf{p}_i^{\text{mean}}, \sigma_i^2 \mathbf{C}_i). \tag{3.38}$$

Here, $\sim$ denotes equality in distribution. The index $k \in [1, ..., N_{\text{pop}}]$ labels the k-th realization of the parameter set $\mathbf{p}_i^{(k)} \in \mathbb{R}^{N_{\text{par}}}$ that is drawn from the normal distribution and that is a feasible solutions of the optimization problem in iteration i. The normal distribution is specified by the mean value $\mathbf{p}_i^{\text{mean}}$ and the covariance matrix $\mathbf{C}_i$ which is scaled by the step size σ_i.

To calculate the feasible solutions $\mathbf{p}_{i+1}^{(k)}$ for the next iteration the multivariate distribution, from which the candidates are drawn, has to be updated. To this end, the new mean value $\mathbf{p}_{i+1}^{\text{mean}}$, the new step size σ_{i+1}, and the new shape of the covariance matrix $\mathbf{C}_{i+1}$ have to be calculated.

For each of the N_{pop} points in the parameter space the cost function, $f_{\text{cost}}(\mathbf{p}_i^{(k)})$, is evaluated and the best $\mu = N_{\text{pop}}/2$ parameter points are sorted (and relabeled w.r.t. k) according to their values such that $f_{\text{cost}}(\mathbf{p}_i^{(1)}) \leq f_{\text{cost}}(\mathbf{p}_i^{(2)}) \cdots \leq f_{\text{cost}}(\mathbf{p}_i^{(\mu)})$. Using this order, the new mean value of the normal distribution for the next iteration is calculated as weighted sum of the best μ candidates

$$\mathbf{p}_{i+1}^{\text{mean}} = \sum_{k=1}^{\mu} \omega_k \mathbf{p}_i^{(k)}, \tag{3.39}$$

where the weights ω_k are distributed according to

$$\omega_k = \frac{\log\left(\frac{\mu+0.5}{k}\right)}{\sum_{j=1}^{\mu}\log\left(\frac{\mu+0.5}{j}\right)}. \tag{3.40}$$

With this definition, the weights fulfill $\omega_k > \omega_{k+1} > 0\ \forall k$ and $\sum \omega_k = 1$. Thus, the best candidate $\mathbf{p}_i^{(1)}$, that corresponds to the smallest value of the cost function, is weighted with the largest factor. This kind of probability weighted averaging avoids the necessity to calculate or approximate a gradient, which can be problematic for noisy functions.

The updated step size σ_{i+1} and the covariance matrix $\mathbf{C}_{i+1}$ are calculated using cumulative step size adaptation (Ostermeier et al., 1994; Hansen, 2006; Chotard et al., 2012). For this purpose cumulative paths $\mathbf{P}_i^C$ and $\mathbf{P}_i^\sigma$ are defined as

$$\mathbf{P}_{i+1}^{C,\sigma} = (1 - c_{C,\sigma})\mathbf{P}_i^{C,\sigma} + \sqrt{c_{C,\sigma}(2 - c_{C,\sigma})}\mathbf{Y}_i^{C,\sigma}. \tag{3.41}$$

Here, $\mathbf{Y}_i^{C,\sigma}$ are normalized displacements of the mean value $\mathbf{p}_i^{\text{mean}}$ during the latest iteration step (the superscript denotes the case for the cumulative path of the covariance matrix C and the step size σ respectively). The constants $c_{C,\sigma}$ scale how fast the influence of previous iterations decreases: for $c_{C,\sigma} = 1$ the evolutionary paths reduce to the normalized mean step of the last generation and no information about previous steps is taken into account; for $c_{C,\sigma} = 0$ the new paths equal the previous ones and no learning takes place.

For the covariance matrix, $\mathbf{C}_i$, and the step size, σ_i, the displacements, $\mathbf{Y}_i^C$ and $\mathbf{Y}_i^\sigma$, are defined as

$$\mathbf{Y}_i^C = \sqrt{\mu_{\text{eff}}}\frac{\mathbf{p}_{i+1}^{\text{mean}} - \mathbf{p}_i^{\text{mean}}}{\sigma_i}, \tag{3.42}$$

$$\mathbf{Y}_i^\sigma = \sqrt{\mu_{\text{eff}}}\mathbf{C}_i^{-\frac{1}{2}}\frac{\mathbf{p}_{i+1}^{\text{mean}} - \mathbf{p}_i^{\text{mean}}}{\sigma_i}. \tag{3.43}$$

The factor $\mu_{\text{eff}} = \left(\sum_{k=1}^{\mu}\omega_k^2\right)^{-1}$ is the so called *variance effective selection mass* and $\mathbf{C}_i^{-\frac{1}{2}}$ is the square root of the inverse covariance matrix. With these prefactors a neutral selection

(random choice of the 'best' $\mathbf{p}_{i+1}^{(k)}$ for calculation of $\mathbf{p}_{i+1}^{\text{mean}}$) leads to

$$\mathbf{Y}_i^C = \sqrt{\mu_{\text{eff}}} \frac{\mathbf{p}_{i+1}^{\text{mean}} - \mathbf{p}_i^{\text{mean}}}{\sigma_i} \tag{3.44}$$

$$\sim \frac{\sqrt{\mu_{\text{eff}}}}{\sigma_i} \sum_{k=1}^{\mu} \omega_k \mathcal{N}(0, \sigma_i^2 \mathbf{C}_i) \sim \frac{\sqrt{\mu_{\text{eff}}}}{\sigma_i} \mathcal{N}(0, \sum_{k=1}^{\mu} \omega_k^2 \sigma_i^2 \mathbf{C}_i) \tag{3.45}$$

$$\sim \mathcal{N}(0, \mathbf{C}_i), \tag{3.46}$$

where eq.(3.38) and eq.(3.39) have been used for the first $\sim$ relation. An analogue calculation results in $\mathbf{Y}_i^\sigma \sim \mathcal{N}(0, \mathbb{1})$ under natural selection. Thus, under neutral selection, the updated cumulative path, $\mathbf{P}_{i+1}$, would have the same statistics as in the previous iteration. This holds true because the prefactors in eq.(3.41) are chosen such that for equally independent normal distributed $\mathbf{P}_i$ and $\mathbf{Y}_i$ (i.e. $\mathbf{P}_i \sim \mathbf{Y}_i$) also $\mathbf{P}_{i+1}$ is normal distributed with the same covariance (Hansen and Ostermeier, 2001)

$$\mathbf{P}_{i+1} \sim (1-c)\mathbf{P}_i + \sqrt{c(2-c)}\mathbf{Y}_i \sim \mathbf{P}_i.$$

Therefore, under neutral selection no bias is introduced in the evolution of the path.

With eq.(3.41) and eq.(3.43) the new step size is calculated according to

$$\sigma_{i+1} = \sigma_i \exp\left(\frac{c_\sigma}{2}\left(\frac{|\mathbf{P}_{i+1}^\sigma|^2}{N_{\text{par}}} - 1\right)\right). \tag{3.47}$$

Whenever the length of the cumulative path is larger than the expected value under random selection ($|\mathbf{P}_{i+1}^\sigma|^2 > N_{\text{par}}$) there is a correlation between the direction of consecutive steps, and an increase of step size is likely to be beneficial. On the other hand, if previous steps point in different directions they partly cancel each other and the length of the cumulative path is small, which results in a decrease of the step size (Hansen, 2006). To avoid too fast increasing or diverging step size, this update is only performed when the exponent is smaller than 0.6, otherwise the exponent is set to 0.6.

With eq.(3.39), eq.(3.41) and eq.(3.42) the new covariance matrix is calculated according to

$$\begin{aligned}\mathbf{C}_{i+1} =& (1-c_C)\mathbf{C}_i + c_C \left[\alpha \mathbf{P}_{i+1}^C \left(\mathbf{P}_{i+1}^C\right)^T \right. \\ & \left. + (1-\alpha) \sum_{k=1}^{\mu} \omega_k \left(\frac{\mathbf{p}_i^{(k)} - \mathbf{p}_i^{\text{mean}}}{\sigma_i}\right)\left(\frac{\mathbf{p}_i^{(k)} - \mathbf{p}_i^{\text{mean}}}{\sigma_i}\right)^T\right].\end{aligned} \tag{3.48}$$

Here, the first two terms describe the covariance-matrix update due to the evolution path (eq.(3.41)) as introduced in (Hansen and Ostermeier, 2001). This increases the probability to reproduce successful evolution paths rather than single mutation steps (Hansen and Ostermeier, 1996, 2001). The last term is an additionally matrix that increases the performance for large population sizes (large N_{pop}) (Hansen et al., 2003). The parameter $\alpha \in (0, 1)$ weights the two different update contributions.

With these equations the update process is completed and a new generation of feasible solutions can be drawn from $\mathcal{N}(\mathbf{p}_{i+1}^{\mathrm{mean}}, \sigma_{i+1}\mathbf{C}_{i+1})$. Practically, we use the CMA-ES implementation from the PYTHON "cma" package (Hansen and Baudis, 2008 - 2015).

3.5.3. Illustration of the optimization process

To provide a less abstract illustration of the algorithm, the fitting procedure for a two-dimensional parameter space is illustrated in Fig.3.5. Here, the two-compartment model is optimized in a two-dimensional subset of the full parameter space. The parameters that are optimized are the conductance ratios g_c/g_s and g_c/g_d, while the remaining model parameters are fixed at values that have been estimated in a previously performed optimization in the full parameter space (where all parameters have been optimized). In Fig.3.5, the parameters are rescaled by the respective values of the full optimization such that the result of the complete fit is located at the coordinate (1,1).

The parameter values that are drawn by the CMA-ES algorithm are plotted as circles and are color coded according to the corresponding value of the particular cost function $f_{\mathrm{cost}}(\mathbf{p})$. The energy surface (blue surface) has been estimated by evaluating the cost function on a grid in the two-dimensional parameter subset and averaging over 150 realizations to eliminate the intrinsic noise. Note that the noise was not averaged out in the CMA-ES procedure and thus the algorithm had to work on a more noisy surface. The subplots Fig.3.5A-D show the distribution of parameter points that are drawn by the algorithm in different iterations (A for iteration 0, B for iteration 1, C for iteration 10 and D for iteration 80). We can observe that the bivariate normal distribution quickly adapts to the valley in the cost function and that it shrinks into the minimum. We also find that the minimum of f_{cost} is located close to the coordinates (1,1) which correspond to the optimal values that have been found in the optimization of the full nine dimensional parameter space. Although this is not a strict argument for the reliability of the algorithm, the fact that this two-dimensional fit reproduces the result of the complete parameter optimization is an indication that the optimization produces reasonable results, even in the higher-dimensional case.

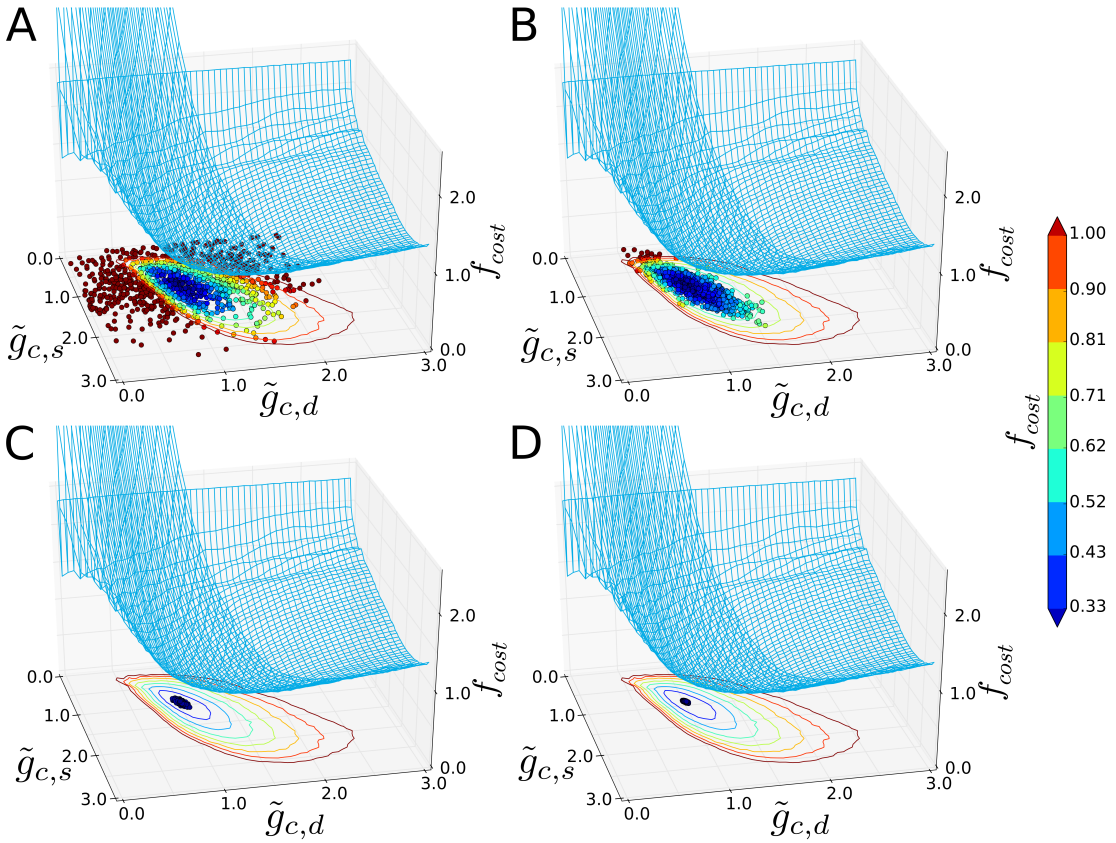

Figure 3.5.: Illustration of the CMA-ES optimization. The energy surface (blue) for a two-dimensional subset of the full (nine dimensional) parameter space is plotted. The feasible solutions (circles) of the CMA-ES algorithm are drawn from a bivariate normal distribution that quickly adapts to the valley of low costs. Individual markers are color coded according to their values of the cost function. A) initial distribution, B) after 1 iteration, C) after 10 Iterations, D) 80th iteration. On the x- and y-axes, $\tilde{g}_{c,s}$ and $\tilde{g}_{c,d}$, rescaled conductance ratios g_c/g_s and g_c/g_d are given. Here, the scaling factor is chosen such that $\tilde{g}_{c,s} = \tilde{g}_{c,d} = 1$ corresponds to the values that have been found for these ratios in a previous fit of the full parameter space.

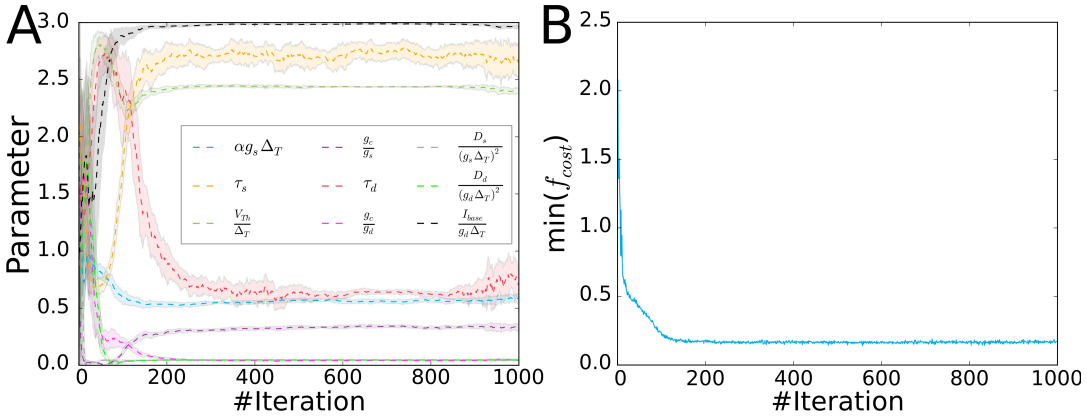

Figure 3.6.: Optimization converges typically within 400 iterations. A) The evolution of the parameters during the optimization process for one typical example. Individual parameter are color coded as indicated. The mean value (dashed line) and the standard deviation (shaded area around the mean) converge to constant values. B) The corresponding evolution of the cost function is plotted. The curve shows the minimal value of all evaluations within a certain iteration. The cost function decreases until it converges to a finite value (except for the weak fluctuations).

Obviously, due to the high dimensionality this kind of visualization is not possible for the full nine dimensional parameter space. Nevertheless, some kind of supervision of the optimization progress is necessary to judge whether the fitting procedure has converged. To this end, the evolution of mean and standard deviation of the individual parameter distributions, and the best value of the cost function can be plotted as a function of the iteration. In Fig.3.6, the parameter evolution is given for a typical optimization procedure (for one particular cell). In Fig.3.6A, the evolution of mean (dashed lines) and standard deviations (shaded area gives the 95% confidence interval $[2\sigma]$) of the parameter values are plotted. To make the different parameters comparable, they are normalized by their starting values (i.e. the mean of the distribution at iteration 0). After 400 iterations both mean and standard deviation converged to constant values (with small fluctuations) for all parameters. In Fig.3.6B, the corresponding evolution of the cost function is plotted. Because N_{pop} parameter points are drawn per iteration the same number of values of the cost function is generated. Here, only the minimal value of these cost function values has been plotted. On average, the cost function decreases with increasing number of iterations until it reaches a constant level.

Such a situation is associated with the convergence of the algorithm and is typically observed within 1000 iterations for all optimizations that have been performed.

3.6. Results

With the above defined one-compartment [eq.(3.1)] and two-compartment models [eq.(3.5) and eq.(3.6)] and with the cost function and the optimization procedure, we investigated to which extend the different models can reproduce all the second-order statistics that are accessible in our in-vivo experiments. In particular, we aim on capturing the spike-train power spectra, $S_{xx}(f)$, the cross-spectra between stimulus and spike trains, $S_{sx}(f)$, the cross-spectra between different spike trains, $S_{x_i x_j}(f)$, and the coherence function, $\mathrm{coh}(f)$.

In Fig.3.7, these statistics are shown for an example cell from motor cortex (black curves) that has been stimulated with bandpass-limited Gaussian white noise with 100 Hz cutoff frequency. The experiment is compared to the results obtained from simulations of the one-compartment model (green) and the two-compartment model (red) for which the parameters have been optimized as described above. Besides these optimized IF models, for this particular cell we simulated the multi-compartment model (blue) used by Eyal et al. (2014). To optimize the performance of the multi-compartment model, no tuning of the intrinsic model parameter has been done, instead we used rescaled versions of the input currents to match the experimental firing rate and added additional white Gaussian noise to the input to account for the trial-to-trial variability.

For all simulations, the same stimuli as in the experiment and for each stimulus the same number of trials have been used. Therefore, some of the fluctuations in the spectra arise from the particular stimulus realizations and are present in both experiments and simulations.

Because of the intrinsic noise that causes a trial-to-trial variability, and due to the finite dataset, repeated simulations will give deviating results for the spectral measures. In Fig.3.7, this variability is illustrated by the colored area that is given by the three fold standard deviation (99.7% confidence interval) of the respective statistic. Thus, for the comparison between simulations and experiment, one can ask for each frequency whether the experimentally measured statistic falls into the colored area or not. Whenever this is the case, the experiment could have been a trial from our simulation, and thus simulation and experiment agree as good as we can expect. However, when the experimental statistics lie outside of the colored area this indicates a qualitative difference between simulation and experiment.

In Fig.3.7A, the power spectra, $S_{xx}(f)$, are shown. All three models agree reasonably well with the experiments. Initially, they show a ramp like increase until they exhibit a pronounced drop that can be associated with f_c. At high frequencies, the spectra saturate at the firing rate (the theoretical high-frequency limit of the power spectra (Cox and Lewis,

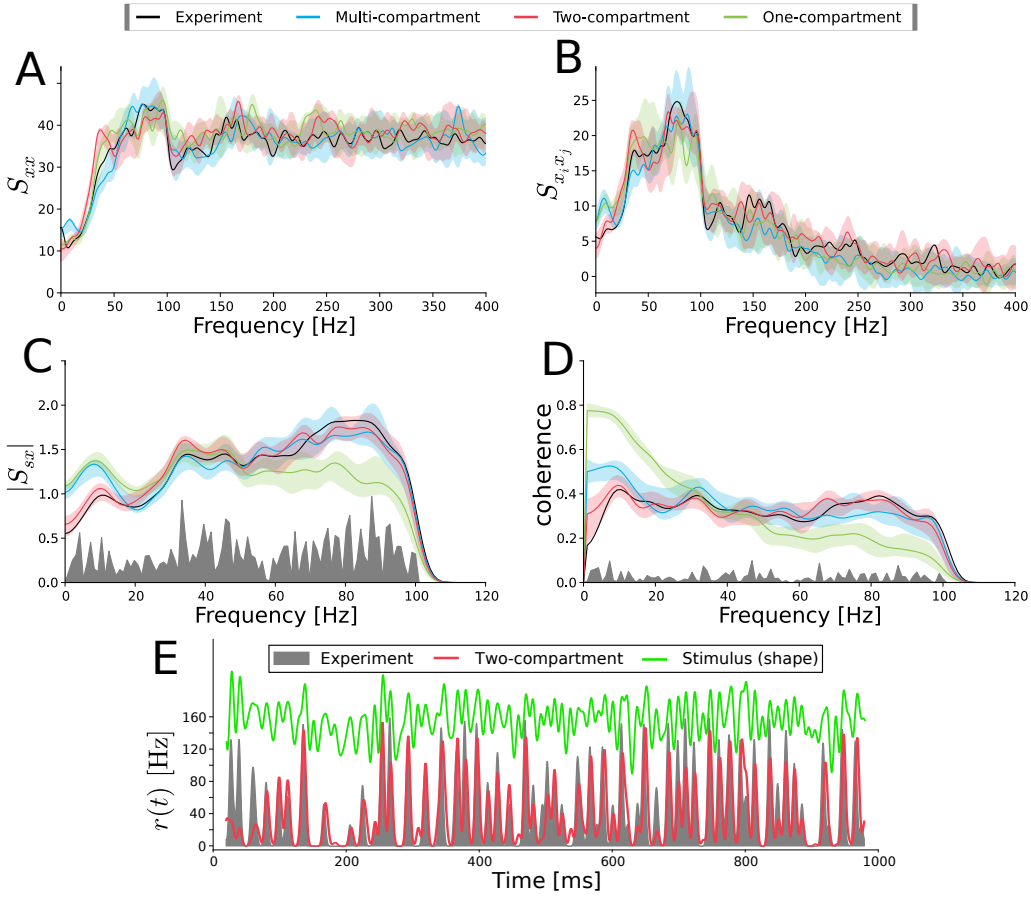

Figure 3.7.: Two-compartment model reproduces experimental statistics for 100 Hz bandpass stimulation. Comparison between simulations (red, green, blue) and experiment (black). The standard deviation of the statistics (transparent color) has been calculated by performing 10 times the same simulation with different realizations of the intrinsic noise. The noise floor in C and D (gray) is calculated by shuffling spike trains and corresponding stimuli. A) The power spectra $S_{xx}(f)$, B) spike-train–spike-train cross-spectra $S_{x_i x_j}(f)$, C) stimulus–spike-train cross-spectra $S_{sx}(f)$ and D) the spectral coherence function $\mathrm{coh}(f)$. E)Example of the instantaneous firing rate for the two-compartment model (red) and the experiment (gray area). To reduce fluctuations caused by the finite size of the data set, all statistics are smoothed with a Gaussian of 3 Hz width.

1966)) which is 37 Hz for this particular cell.

Also, the spike-train–spike-train cross-spectra, $S_{x_i x_j}(f)$ (Fig.3.7B), qualitatively agree for all models and experiment. Here, not only the increase up to the cutoff frequency but also the decay outside the stimulus frequency band (i.e. for $f > 100\,\mathrm{Hz}$) is well matched by the simulations. However, the spectrum for the one-compartment model shows a slightly shallower increase while the two-compartment model even quantitatively reproduces the experiments.

In Fig.3.7C, the absolute value of the input-output cross-spectrum $|S_{sx}(f)|$ is plotted. This plot reveals that the one-compartment model does not show the pronounced increase with frequency that is observed in the experimental spectrum. In contrast, the cross-spectrum for the two-compartment model agrees very well with the experiment in the whole frequency range. Also the multi-compartment model exhibits an increasing cross-spectrum, but performs only slightly worse than the two-compartment model, which is still a surprising agreement because no parameters have been optimized for this model.

For the coherence function (Fig.3.7D), the differences between experiment and one-compartment model are even more pronounced. The one-compartment model exhibits a typical lowpass shape which does not even qualitatively agree with the experiments. The multi-compartment model agrees much better with the measured coherence function, although it slightly decreases with frequency. The two-compartment model almost perfectly matches the experiment and quantitatively reproduces the sustained support of information transfer up to the cutoff frequency very well. This illustrates how the additional dendritic compartment can qualitatively change the information transfer properties of the neuron model.

Another illustration of how the two-compartment model captures the time-dependent response of the neuron can be gained from the instantaneous firing-rate $r(t)$, i.e. the time-dependent probability density for observing a spike at a certain instant in time. This quantity is plotted in Fig.3.7E for one particular stimulus realization for the one-compartment model and the experiment. As a guide for the eye the shape of the stimulus is given at the top of the figure (green line). Both the two-compartment model and the experiment show rapid signal-related changes in the instantaneous firing rate and the peaks appear precisely at the same times. Also, in many cases the variation in the height of the peaks is captured by the model. This reflects the reliability with that the neuron (model) responds to certain parts of the stimulus.

When we estimate the similarity between experiment and simulation in terms of the coincidence factor Γ (eq.(1.26)), the best match is achieved, when two criteria are fulfilled: On the one hand, simulated and experimental spike trains should have the same intrinsic

reliability. This is the case when the coincidence factor, calculated for pairs of simulated spike trains, Γ_{ss}, is as large as it is for pairs of experimentally measured spike trains, Γ_{ee}. On the other hand, simulated spike times should be close to those evoked in experiment. This is achieved best, when the coincidence factor, calculated for mixed pairs of experiment and simulation, Γ_{se}, is as large as possible. In particular, Γ_{se} should be in the order of the intrinsic variabilities, Γ_{ee} and Γ_{ss}. In other words, the simulation has to be as similar to the experiment as the experimental trials are similar to each other. For the example in Fig.3.7, the experimental reliability is $\Gamma_{ee} \approx 0.51$. Simulations of the two-compartment model yield an intrinsic reliability of $\Gamma_{ss} \approx 0.50$ which agrees very well with the experimental value. The similarity between pairs of simulated and experimental spike trains can be calculated as $\Gamma_{se} \approx 0.40$ which is smaller than the intrinsic reliability but still reveals a reasonable agreement. Note that neither the spectral coherence function (Fig.3.7D) nor the instantaneous firing rate (Fig.3.7E) or the coincidence measures are part of the optimization procedure. Instead, they are only indirectly optimized due to the spike-train and input-output statistics used in f_{cost}.

The results for the one-compartment and the two-compartment model fits of a second example, a cell from somatosensory cortex that has been stimulated with white Gaussian noise with 200 Hz cutoff frequency, are given in Fig.3.8. Qualitatively, the results are similar to what we observed for the 100 Hz stimulation in Fig.3.7. The two-compartment model can reproduce all experimentally measured statistics with high accuracy, while the one-compartment model in particular fails to match the input-output statistics (i.e. stimulus spike train cross-spectrum [Fig.3.8C] and the spectral coherence [Fig.3.8D]). The instantaneous firing rate (Fig.3.8E) reveals a close match between experimental and simulated spike times, which is reflected in the values of the coincidence measure. For this cell we obtain $\Gamma_{ee} \approx 0.52$ for the intrinsic reliability in the experiment and $\Gamma_{ss} \approx 0.51$ and $\Gamma_{se} \approx 0.47$ for simulations of the two-compartment model. Thus, in this simulation experimental and model data are almost indistinguishable.

A similar good agreement between spike-train statistics for the two-compartment model and experiment can be achieved for other cells from motor cortex and somatosensory cortex, while the one-compartment model systematically performs worse. In comparison with a detailed dendritic tree, the additional dendritic compartment is a remarkably simple extension of the one-compartment model that still seems to be sufficient to account for the high-frequency transmission of time-dependent stimuli that are injected in the soma.

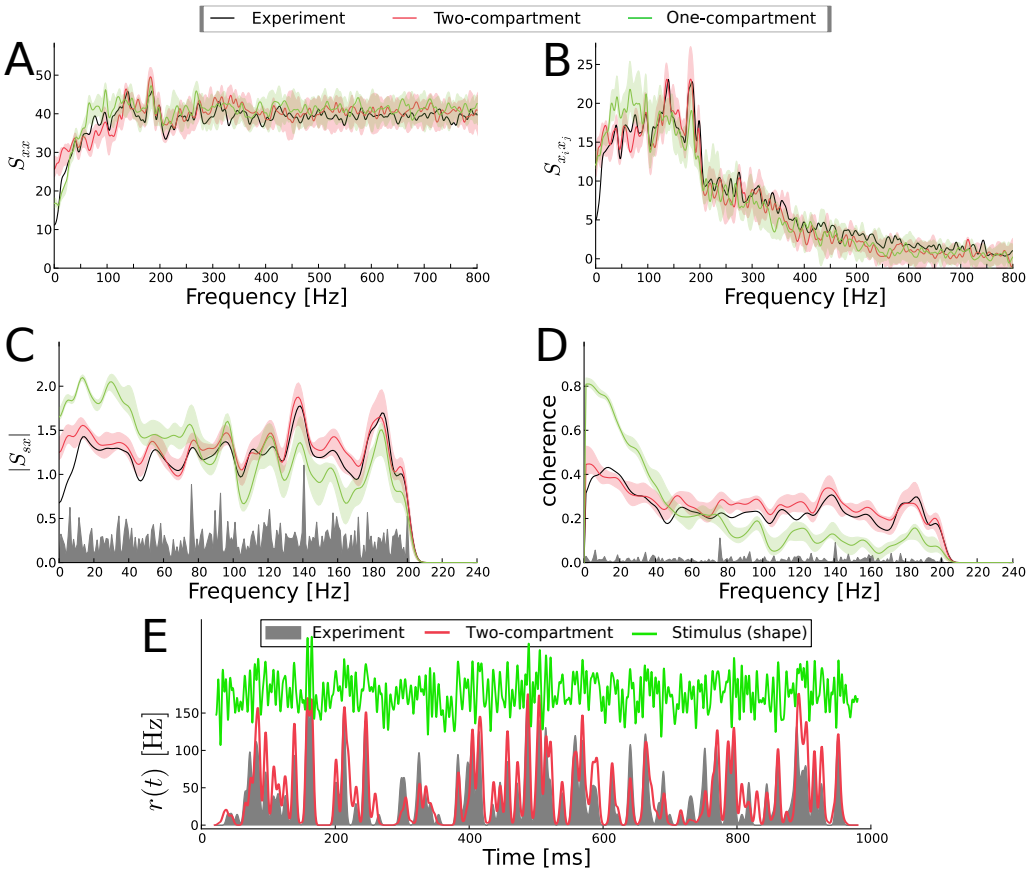

Figure 3.8.: Two-compartment model reproduces experimental statistics for 200 Hz bandpass stimulation. Comparison between simulations (red, green) and experiment (black). The standard deviation (transparent color) has been calculated by performing 10 times the same simulation with different realizations of the intrinsic noise. The noise floor in C and D (gray) is calculated by shuffling spike trains and corresponding stimuli. A) The power spectra $S_{xx}(f)$, B) spike-train–spike-train cross-spectra $S_{x_i x_j}(f)$, C) stimulus–spike-train cross-spectra $S_{sx}(f)$ and D) the spectral coherence function $\mathrm{coh}(f)$ E) Example of the instantaneous firing rate for the two-compartment model (red) and the experiment (gray area). To reduce fluctuations caused by the finite size of the data set, all statistics are smoothed with a Gaussian of 3 Hz width.

3.6.1. Metastatistic

Goodness-of-fit For a systematic comparison of the performance of the one- and the two-compartment model, we define a measure for the goodness-of-fit, Λ. As mentioned above, the finite dataset gives rise to measurement noise in the spectral measures. In order to quantify deviations between simulated and experimental data that go beyond this measurement noise, based on the statistics of the particular measures for the simulated model, we define the functions $\Phi_i^{\pm} = \langle \Phi_i^{\mathrm{sim}} \rangle \pm 3 \cdot \mathrm{SD}(\Phi_i^{\mathrm{sim}})$ with $\Phi_1^{\mathrm{sim}}(f) = S_{xx}(f)$, $\Phi_2^{\mathrm{sim}}(f) = S_{x_i x_j}(f)$ and $\Phi_3^{\mathrm{sim}}(f) = S_{sx}(f)$. Typically, the simulated statistics will be within the region between Φ_i^- and Φ_i^+ (i.e. the colored area in Fig.3.7A-C and Fig.3.8A-C). Therefore, the extent to which the experimentally measured spectra, $\Phi_i^{\mathrm{exp}}(f)$, deviate from this region, provides us with a measure for the goodness-of-fit:

$$\Lambda = \frac{1}{3} \sum_{i=1}^{3} \frac{\int_0^{f_F} \Theta(|\Phi_i^-| - |\Phi_i^{\mathrm{exp}}|)|\Phi_i^{\mathrm{exp}} - \Phi_i^-| + \Theta(|\Phi_i^{\mathrm{exp}}| - |\Phi_i^+|)|\Phi_i^{\mathrm{exp}} - \Phi_i^+| \, \mathrm{d}f}{\int_0^{f_F} |\langle \Phi_i^{\mathrm{sim}} \rangle| \, \mathrm{d}f}, \quad (3.49)$$

Here, $\Theta(x)$ denotes the Heaviside function and $f_F = 1.5 f_{\mathrm{c}}$. This expression compares the area between experimental statistics and colored region to the area under the mean of the respective simulated statistic. Intuitively, Λ can be regarded as a percental deviation of the spectral statistics between simulation and experiment.

In Fig.3.9, Λ is plotted for 16 cells for which the fitting procedure has been applied for the one- and for the two-compartment model. The cells are labeled and sorted along the x-axis according to the Λ-values that correspond to the fit of the two-compartment model. Using this measure, the superiority of the two-compartment model over the one-compartment model becomes apparent. However, not for all cells satisfying two-compartment model fits could be found; beyond cell index 10, we observe a distinct increase of Λ with the cell index. We introduced a threshold (dashed line in Fig.3.9) that divides the population into cells below threshold ('good' fits; blue symbols) and above threshold ('less good' fits; red symbols). Note that the two-compartment model provided the better fit even for the cells for which the statistics are not well captured (above threshold).

Reliabilty of the optimization strategy Because we perform the optimization on an energy surface with mostly unknown properties, there is no guarantee that it always converges to the optimal parameter values. To estimate the reliability of the optimization, the model can be fitted to data that has been created by the model itself. This testing optimization-task is in principle perfectly solvable and the optimal solution would correspond to $\Lambda = 0$. However, due to the noise, the finite dataset, and the potentially

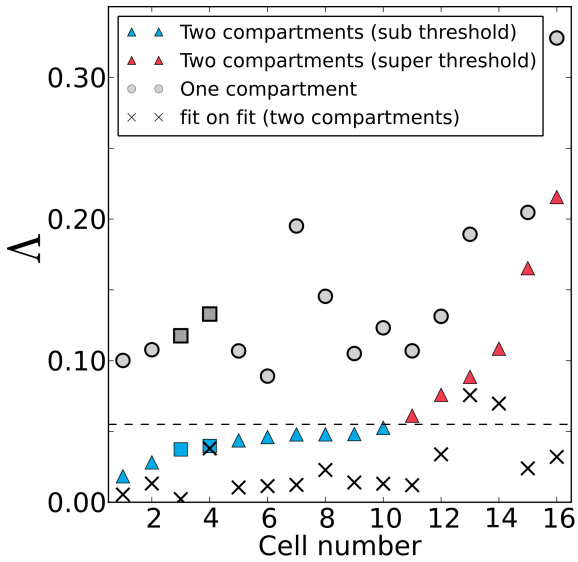

Figure 3.9.: Two-compartment model performs systematically better than one-compartment model. The goodness-of-fit measure Λ is plotted for 16 cells (cell label on the x-axis) for the case of a one- and a two-compartment model fit. The dashed horizontal line indicates a threshold that we chose to separate fits that performed 'good' (below threshold) and fits that performed 'less good' (above threshold). Fits corresponding to Fig.3.7 and Fig.3.8 are indicated by squares. The goodness-of-fit for the one-compartment model is given by gray symbols that of the two-compartment model by blue (subthreshold) and red (superthreshold) symbols. Black crosses correspond to Λ-values that were calculated by fitting a two-compartment model to the statistics that have been achieved from the fit of this particular model to the experiment (i.e. a model fit to the very same model).

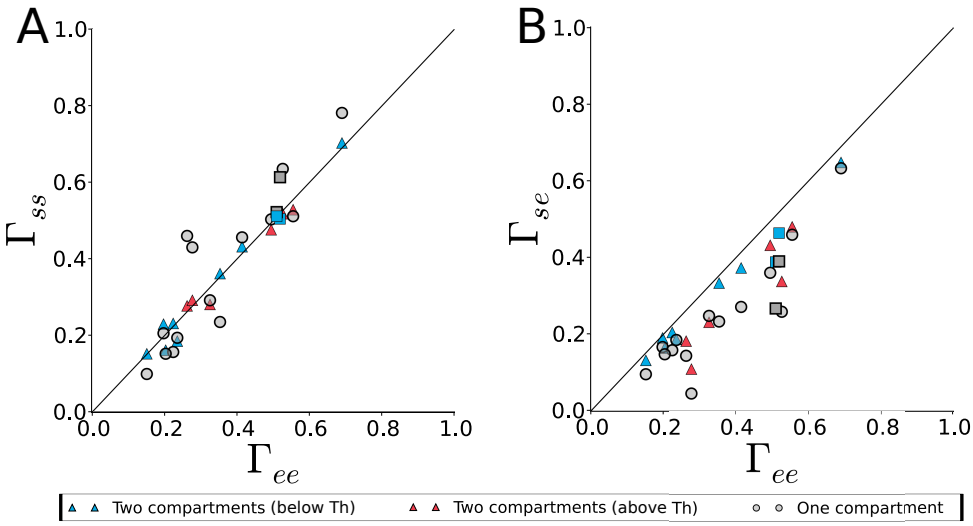

Figure 3.10.: Two-compartment model matches experimental spike times better than one-compartment model. Comparison of the one- and the two-compartment model in terms of the coincidence factor Γ. Color coding as in Fig.3.9. A) Scatter plot of the intrinsic reliabilities for simulation Γ_{ss} and for experiment Γ_{ee}. Data points are distributed along the diagonal (optimal values), but data for the one-compartment model are spread in a wider region. B) Scatter plot of the trial-to-trial reliability in experiment, Γ_{ee}, and the similarity between experiment and simulation, Γ_{se}. The two-compartment model is closer to the diagonal (i.e. the optimal value) than the one-compartment model in both plots.

complicated shape of the energy surface it is unclear to which extent the optimization can reproduce the original data. To test this, we have fitted the two-compartment model to the statistics that have been obtained from fitting the model to the experimental data. In Fig.3.9, the goodness-of-fit for these optimizations is shown (black crosses). We observe that these fits lead to finite but small Λ-values for most cells. Typically, these Λ-values are clearly below those belonging to the fit of the two-compartment model to the experiment (blue and red symbols), which already produced a remarkably agreement. On the one hand, this illustrates the ability of the optimization strategy to converge into a pronounced minimum of the cost function. On the other hand, it suggests that the two-compartment model, although it provides a remarkably agreement with the experimental results, still is not able to match all statistics perfectly.

Besides the comparison in term of spectral statistics, we can estimate the similarity between experiment and simulations in terms of the coincidence factor Γ. These results are shown in Fig.3.10 by using the same color code as in Fig.3.9 (i.e. one-compartment model - gray; two-compartment model - blue [subthreshold] and red [suprathreshold]).

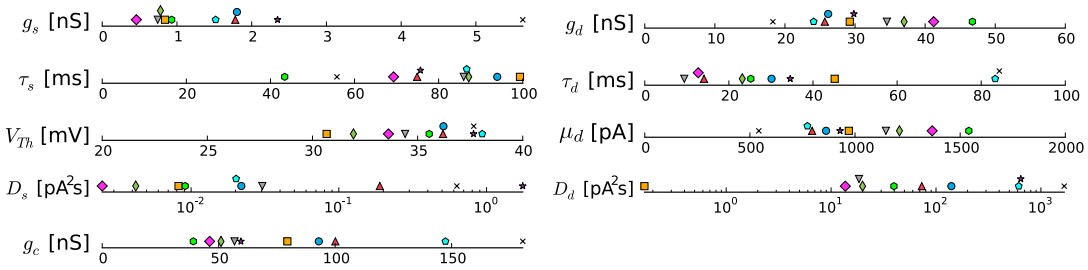

Figure 3.11.: Graphical representation of the nine parameter values resulting from the two-compartment model fits for cells with subthreshold performance. Each symbol/color belongs to a specific cell (some symbols have been shifted vertically for better visibility). A table with these parameter values is given in the appendix.

Fig.3.10A shows the trial-to-trial reliability within simulations (Γ_{ss}) versus the intrinsic trial-to-trial reliability of the experiment (Γ_{ee}). For both models the data is aligned along the diagonal which indicates a similar degree of intrinsic reliability. However, the two-compartment model remains closer to the diagonal than this is the case for the one-compartment model, indicating that the former matches the intrinsic reliability with higher accuracy. In Fig.3.10B, the similarity between simulated and experimental spike trains (Γ_{se}) is plotted against the intrinsic reliability (Γ_{ee}) of the experiment. The data points are again oriented along the diagonal, but tend to be systematically below. This offset reflects that on average the similarity between two randomly chosen experimental spike trains is slightly larger than that between a simulated spike train and an experimental one. However, in comparison to the one-compartment model, the distribution of the data points again reveals superior performance of the two-compartment model, the values of which are closer to the diagonal. Also, when comparing the two-compartment fits that yield subthreshold performance (blue symbols) to those with suprathreshold performance (red symbols), the former tend to be distributed closer to the diagonal than the latter. Thus, the comparison in terms of the coincidence measure qualitatively agrees with the results obtained for the goodness-of-fit (Fig.3.9) and again reveals that the performance of the two-compartment model exceeds that of the one-compartment model.

Parameter values Besides the similarity between experiments and simulation, an interesting question is how the parameter values that result from the optimization process are distributed. Because we made the model dimensionless (see. eq.(3.5) and eq.(3.6)), these parameters are combinations of the biophysical model parameters (see eq.(3.7)), and therefore we have some freedom of choice when calculating the biophysical values. To eliminate this redundancy, we fixed the spike slope factor $\Delta_T = 0.5\,\mathrm{mV}$ and the input scaling

factor α such that the somatic input resistance equals 45 MΩ which is the value that was observed on average in our intracellular recordings. The parameter values that belong to the ten cells that produced a 'good' fit (below threshold) are presented in Fig.3.11. All parameters have a reasonable order of magnitude as discussed in ch.3.4. From this plot, it turns out that the somatic noise intensity D_s takes values much smaller than the noise intensity in the dendritic compartment. This agrees well with the interpretation of the synaptic input as source of the dendritic noise. However, because the two-compartment model still is a strongly simplified biophysical description, these values should be regarded as effective parameter values only.

3.7. Critical review

Besides the spatial extension of the neuron also other mechanisms can affect the spectral coding properties and can improve the performance of the model. In the following, we will briefly elaborate on this issue.

Colored noise As shown in Brunel et al. (2001); Fourcaud and Brunel (2002); Fourcaud-Trocmé et al. (2003), the support of high frequencies can be enhanced e.g. due to the color of the input noise. We therefore also tried to match the experimental results by a one-compartment EIF model that is subject to additive Ornstein-Uhlenbeck (OU) noise with different correlation times. Using OU noise in the one-compartment model is equivalent to the case of white Gaussian noise in the dendritic compartment of the two-compartment model and setting $g_c/g_d = 0$ which simplifies eq.(3.6) such that it generates an exponentially filtered version of the white noise (i.e. OU noise). However, our attempts to reproduce the experimental statistics by a one-compartment EIF model with colored noise were not successful. A significant improvement of the fit could only be observed if a combination of the enhanced high frequency transfer due to the modified subthreshold dynamics ($g_c/g_d > 0$) and a dendritically filtered (colored) noise were present.

This is to some extent reflected by the shape of the energy surface in Fig.3.5. Here, the values of the cost function along the $\tilde{g}_{c,s}$-axis (i.e. for $\tilde{g}_{c,d} \sim g_c/g_d = 0$) correspond to the afore mentioned case of a single compartment model with colored OU noise. Of course for this plot the parameters are optimized for the two-compartment model and the values of the surface on the $\tilde{g}_{c,s}$-axis would look different if the optimization of the remaining parameter would have been preformed for the one-compartment model. However, the global minimum is located at $\tilde{g}_{c,d} \sim g_c/g_d > 0$ while the cost function increases for $g_c/g_d \to 0$. In the picture of the one-compartment model (i.e. for $g_c/g_d = 0$), the parameter $\tilde{g}_{c,s}$

becomes redundant and effectively scales the intensity of the colored noise and the somatic leak conductance. Along the $\tilde{g}_{c,s}$-axis the cost function has a local minimum (close to $\tilde{g}_{c,d} = 0$) that corresponds to the best values of the intensity of the colored noise and leak conductance (for the other parameters fixed). This minimum, however, is significantly above the global minimum.

Spike-frequency adaptation The equations for a one-compartment model that is equipped with an adaptation mechanism can be expressed as (Brette and Gerstner, 2005)

$$\tau \frac{\mathrm{d}V}{\mathrm{d}t} = -V - \frac{w}{g} + e^{V_\mathrm{s} - V_\mathrm{Th}} \frac{I}{\alpha \Delta_T g} \tag{3.50}$$

$$\tau_w \frac{\mathrm{d}w}{\mathrm{d}t} = -w + aV. \tag{3.51}$$

As explained in Gerstner et al. (2014), for the case without dendritic noise there is a mapping between these equations and that of the two-compartment model (eq.(3.5) and eq.(3.6)). Mathematically, this mapping is achieved by the substitutions $w = -g_c V_\mathrm{d}$, $a = -g_c^2/(g_c + g_d)$, $\tau_w = \tau_d/(1 + g_c/g_d)$, $g = g_c + g_s$ and $\tau = \tau_s/(1 + g_c/g_s)$. Here, we can make two important observations that discriminate the adaptation due to the passive dendrite from classic ion-channel caused adaptation. First, the factor a in eq.(3.51) is always smaller than zero, and therefore the adaptation that is induced by the passive dendrite is facilitating. Also, because g_c describes the intracellular conductivity between somatic and dendritic compartment, we found $|a|$ to be significantly larger (see table 2 in appendix A) than typical adaptation conductances that are in the order of a few nS (Brette and Gerstner, 2005; Naud et al., 2008). Second, due to the scaling $\tau_w = \tau_d/(1 + g_c/g_d)$ the timescale of this adaptation variable is smaller than the typical dendritic time scale, and therefore the dendritic compartment causes a comparably fast adaptation. Besides the sign of a and the timescale of the adaptation, another difference to the classical adaptive model is the noise term that in our case enters via the dendritic (adaptation) variable, and therefore acts as colored noise on the somatic compartment.

Increased number of parameters One might argue that the improvement of the fit by adding the additional dendritic compartment is simply due to the increased number of parameters that is acompanied by this extension. However, as we have shown by the analysis of the subthreshold properties the two-compartment model shows qualitatively different transfer characteristics that cannot be accounted for by the one compartment model. Also, the broadband shape of the coherence function that was achieved only by

the two-compartment model is qualitatively different to the information transfer of the one-compartment model.

Another argument that models with increasing number of parameters do not necessarily produce the better results can be obtained from a competition in which different neuron models have to predict spike times of a pyramidal cell. Surprisingly, in this competition the winning model that performed best turned out to be the model with the smallest number of free parameters within all participating models (Naud and Gerstner, 2013).

3.8. Summary

In this chapter, we motivated the extension of the one-compartment EIF model to a two-compartment EIF model. To this end, we showed that the subthreshold response-function of the two-compartment model has a frequency dependence that is similar to that of models which take a dendrite into account with more accuracy. In particular, for the two-compartment model, the frequency response showed a stronger support to high-frequent stimulus components (relative to the support of low frequencies) than this is the case for the one-compartment model. This enhanced high-frequency transmission has been explained by current that leaks into the additional dendritic compartment. By approximating the frequency-response curve in different regions (low, intermediate and high frequencies), we could show that this leak is more pronounced for low-frequent stimulus components and vanishes in the high-frequency limit.

In order to capture the experimental results in simulations, we defined a cost function that measures the similarity of power spectra, spike-train–spike-train cross-spectra, stimulus–spike-train cross-spectra and of the firing rate between simulations and experiment. We estimated a plausible range of parameter values and briefly introduced the CMA-ES algorithm that has been used to optimize these values. The results of the parameter optimization revealed that the two-compartment model could reproduce all the experimentally measured statistics with a high degree of accuracy for many cells. In particular, this model was able to match the high-frequency information transfer that is indicated by the flat shape of the spectral coherence function. In contrast, the one-compartment model performed systematically worse than the two-compartment model and showed a typical lowpass coherence. Thus, we could show that the extension with an additional compartment that is supposed to account for the influence of the dendritic tree, is sufficient to account for the broadband coding of information that could not be described by the one-compartment model.

Chapter 4.

Dictating spike times with Gaussian stimuli

The importance of AP timing in contrast to a neural code in which only the mean firing rate is taken into account, has been debated for more than two decades (Softky and Koch, 1993; Shadlen and Newsome, 1994; König et al., 1995) but still remains an open problem (London et al., 2010; Tchumatchenko et al., 2011; Deneve and Machens, 2016). Since that time, a series of experiments has revealed that a microscopic change, such as a few extra spikes in single cortical neurons, can cause a macroscopic response in the animals behavior or brain state (Brecht et al., 2004; Houweling and Brecht, 2008; Li et al., 2009; Doron et al., 2017). To investigate the role of single APs and AP timing in these kind of 'reverse physiology' experiments, the control about the neuronal dynamics plays a key role.

Up to here, this work was about the question, whether Gaussian stimuli can reliably evoke spike trains in juxtacellular stimulation. To this end, random noise-stimuli have been generated and were used to stimulate cortical neurons. Indeed, this stimulation evoked reliable spike trains, however, the precise timing of the APs remained unknown until the stimulus had been applied.

In this chapter, we extend the problem of evoking reliable spike trains to the issue of defining a prescribed spike train, $x_\dagger(t)$, and to ask for the stimulus, $s_\dagger(t)$, that is supposed to evoke this spike train in a particular neuron. We present an approach to find such a stimulus, and explore experimentally and by numerical simulations, how well the prescribed spike train, $x_\dagger(t)$, and its firing statistics can be evoked by the resulting stimulus, $s_\dagger(t)$. On this stimulus, we impose certain constraints that arise from experimental issues. In particular, we want the stimulus to have i) a finite cutoff-frequency f_c and ii) Gaussian statistics with prescribed mean μ and variance σ^2.

The limitation to a finite cutoff-frequency is motivated by the issue of spike extraction as addressed in ch.2.1: because the input signal and the recorded voltage that contains the APs are superimposed, the input has to be filtered out to allow for detection of the

comparably small APs. This requires a restriction of the frequency domain of the input stimulus, which will be achieved here by using bandpass-limited signals with $f_c = 100\,\mathrm{Hz}$. The second constraint of Gaussian statistics with mean μ and variance σ^2 is motivated by the observation that these kind of stimuli are well tolerated by neurons. Also, the (synaptically filtered) superposition of many input spike trains approaches in many cases Gaussian statistics why this choice seems to be natural. These constraints exclude the first intuitive solution of our problem that is to use a sequence of strong and sharp excitatory current pulses positioned at the prescribed spike times (note that exactly this excluded simple approach was successfully applied in a recent publication by Stüttgen et al. (2017)).

The basic idea and some experimental results on our approach have been published in Doose et al. (2016). This is supported by numerical simulations and a more detailed description of the method in Doose and Lindner (2017).

In the following, we first propose the way how we define the prescribed spike train and later on, we explain the method to generate the stimulus that is supposed to evoke this spike train. It is plausible that the procedure works particularly well, if the prescribed spike train has similar spiking statistics as a spike train generated by this neuron under white Gaussian noise stimulation. Therefore, we first test the performance of our method in experiments with cortical neurons in-vivo for the latter case. We then study numerically the dependence on deviations for the reference statistics (i.e. firing rate and CV) of the prescribed spike train. This is done for two different neuron models, one- and a two-compartment model, and for the suprathreshold and the subthreshold firing regime. For an overview of the whole procedure that computes the stimulus, a schematic representation of the method is given in Fig.4.1 and a pseudo-algorithm of the method is presented in appendix B.

4.1. The systems under investigation

Because one-compartment IF models are used in many neural network studies, it is vital to understand to which extent spike timing can be controlled by time-dependent stimuli in this model class. To this end, we used the one-compartment model with parameter values that are given by Harrison et al. (2015) for pyramidal neurons from layer 2/3 of the rat somatosensory cortex (see table 2 in (Harrison et al., 2015)). However, as we have shown in the previous part of this work, in some situations a one-compartment model is not sufficient to quantitatively reproduce all neuronal spike statistics that can be accounted for by a two-compartment model (Ostojic et al., 2015). Thus, in the following we will also inspect how well spike trains can be evoked in the two-compartment EIF model (see

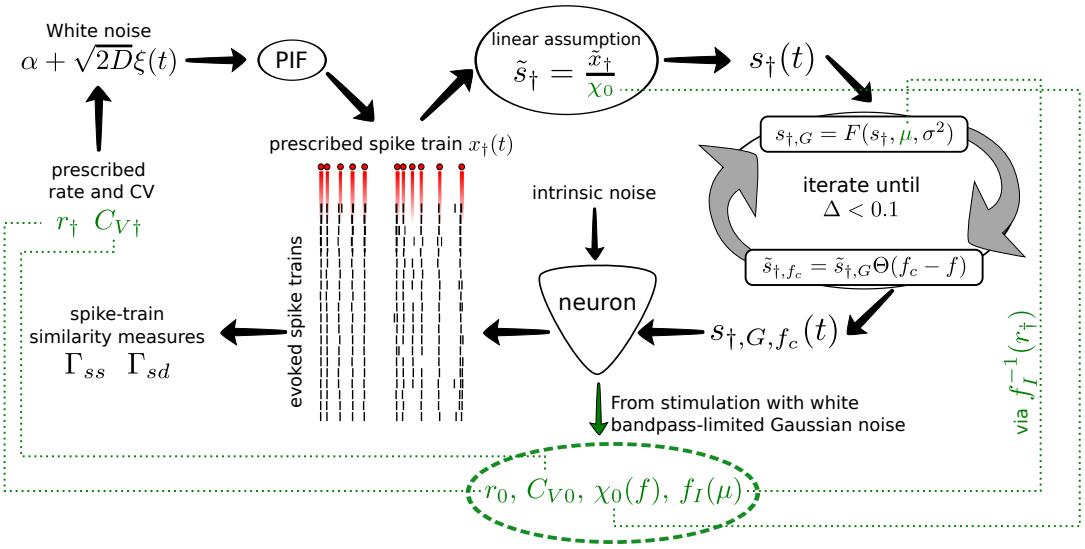

Figure 4.1.: Schematic representation of the procedure that generates prescribed spike trains by stimulating a neuron with colored Gaussian noise with a given cutoff frequency f_c. The green dotted lines indicate which parts of the procedure are influenced by neuron-specific properties (listed in the dashed ellipse).

eq.(3.5) and eq.(3.6)). Here, we use the parameter values that have been achieved for the fit of the cell shown in Fig.3.7.

Besides the numerical studies with the one- and the two-compartment model, in-vivo experiments with juxtacellular stimulation in cortical neurons have been performed[1]. To ease the notation, we will only refer to the *neuron*, even if the *neuron model* is also meant.

4.2. Estimating reference statistics and basic dynamical properties

Before we define the statistics (rate and CV) of the prescribed spike train, and before we can calculate a stimulus that evokes this spike train, we have to explore the 'working point' of the neuron under investigation. This 'working point' is defined by typical firing statistics under the stimulation with a stimulus that has physiological tolerated properties. To explore the *reference* dynamics in response to such a stimulus, we perform a probing experiment in which we measure basic properties of the neuron by stimulating it with

[1]Surgery and electro-physiological recordings have been done by: Guy Doron, NeuroCure Cluster of Excellence, Humboldt Universität zu Berlin, 10117 Berlin, Germany
guy.doron@charite.de

bandpass-limited white Gaussian noise

$$s_0(t) = \mu_0 + \sigma_0 \eta(t). \tag{4.1}$$

Here, $\eta(t)$ is a white Gaussian signal with cutoff frequency $f_c = 100\,\mathrm{Hz}$, unit variance and zero mean. The parameter μ_0 and σ_0^2 specify the mean and the variance of the stimulus. Stimulating the cell with an input as eq.(4.1) provides us with *reference values* for rate and CV, r_0 and C_{V0}, for this particular neuron. Besides this, we can use the white noise stimulation to estimate two other important statistical measures:

The first is the susceptibility at the reference point (r_0, C_{V0}) that is calculated from the input-output cross-spectrum $S_{s_0x}(f)$

$$\chi_0(f) = \frac{S_{s_0x}(f)}{S_{s_0s_0}(f)}, \tag{4.2}$$

where $S_{s_0s_0}(f)$ is the power spectrum of the input current.

The second is the firing-rate-vs-input current relation

$$r_0 = f_\mu(\mu_0, \sigma_0^2), \tag{4.3}$$

that is the mean firing rate measured for a whole range of mean input values μ_0 while the variance σ_0^2 is fixed.

For the remaining part, these quantities will be assumed to be known.

4.3. Creating the prescribed spike train

In previous works different ways to create spike trains with prescribed statistics have been proposed (L. Gomez et al., 2005; Brette, 2009; Macke et al., 2009). For our purpose, we will focus on renewal spike trains with a given prescribed rate, $r_\dagger$, and CV, $C_{V\dagger}$. Because both, rate and CV, are completely defined by the first and the second moment of the ISI distribution of the spike train, all distributions that have the appropriate moments are consistent with these statistics. For the PIF model under white noise stimulation the ISI distribution is known analytically and obeys an inverse Gaussian distribution which is completely defined by the first two moments (Gerstein and Mandelbrot, 1964; Holden, 1976). Thus, in order to generate a renewal spike train, one could subsequently draw ISIs from this distribution. However, here we use the simpler alternative approach and

simulate a white-noise driven PIF model that is given by

$$\frac{\mathrm{d}V}{\mathrm{d}t} = \alpha + \sqrt{2D}\xi(t), \tag{4.4}$$

where $\xi(t)$ is white Gaussian noise with $\langle \xi(t) \rangle = 0$ and $\langle \xi(t)\xi(t') \rangle = \delta(t-t')$, and that has the fire-and-reset rule, whenever $V > 1$ a spike time is registered and a reset, $V \to 0$ is applied. The firing rate and the CV of the renewal spike train that is generated by this model uniquely correspond to the constant input α and the noise intensity D (Vilela and Lindner, 2009a). This relation can be inverted which reveals how the model parameters have to be chosen in order to evoke the prescribed rate and CV:

$$\alpha = r_\dagger, \quad D = \frac{r_\dagger C_{V\dagger}^2}{2}. \tag{4.5}$$

Here, the particular choice of the values for the prescribed rate and CV will be made relative to the reference values r_0 and C_{V0} of the neuron under investigation. For the numerical simulations we varied the prescribed statistics around these reference values and changed the firing rate between $0.5r_0$ and $1.5r_0$ in 20 steps and the CV between $0.2C_{V0}$ and $2.5C_{V0}$ in 46 steps. In the experiments, we only used the reference values itself as prescribed values, $r_\dagger = r_0$ and $C_{V\dagger} = C_{V0}$.

4.4. Calculating a stimulus to evoke the prescribed spike train

Our procedure to calculate stimuli that are supposed to evoke prescribed spike trains involves approximations and transformations that have to be justified a posteriori by testing the performance of our method. Hence, in the following the method is first presented step by step, without addressing the question of the justification:

For a system that acts purely linearly, the input, $s(t)$, and the output, $x(t)$, are related via a convolution

$$x(t) = K * s(t). \tag{4.6}$$

Here, $K(t)$ is the linear response function and $*$ denotes convolution. In the frequency

domain the convolution eq.(4.6) simplifies to a multiplication:

$$\tilde{x}(f) = \chi(f)\tilde{s}(f). \tag{4.7}$$

In this equation the Fourier transform of the linear response function, $K(t)$, can be identified as the susceptibility, $\chi(f)$. The assumption to describe the dependence of input and output by a linear relation constitutes a strong approximation (although eq.(4.7) captures an important part of the full dynamics).

In the following, regardless of the statistics of the prescribed spike train or the stimulus, we use the susceptibility, χ_0, (eq.(4.2)) that is measured under white noise stimulation at the respective reference point (μ_0, σ_0). With the knowledge of the susceptibility, we can use eq.(4.7) to calculate the stimulus $\tilde{s}_\dagger(f)$ that evokes the output $\tilde{x}_\dagger(f)$:

$$\tilde{s}_\dagger(f) = \frac{\tilde{x}_\dagger(f)}{\chi_0(f)}. \tag{4.8}$$

The usage of $\chi_0(f)$ independent of the actual values, μ, σ, of the input current and regardless of the CV and firing rate of the prescribed spike train is again an approximation. Also, the stimulus in eq.(4.8) is colored noise which can affect the susceptibility [see e.g. (Fourcaud-Trocmé et al., 2003)].

The equation eq.(4.8) provides us with a stimulus in the Fourier-domain that delivers the prescribed stimulus, $s(t)$, as time series by applying inverse Fourier transformation. However, because $x_\dagger(t)$ is a train of δ-pulses, eq.(4.8) will not fulfill all our constraints of Gaussianity, given mean and variance, and finite cutoff frequency at the same time. To impose these restrictions, we further process $s_\dagger(t)$.

In a first step we apply a static nonlinear transformation, $F(s, \mu, \sigma)$, to the stimulus in the time domain

$$s_{\dagger,\mathrm{G}}(t) = F(s_\dagger(t), \mu, \sigma^2), \tag{4.9}$$

which provides us with a stimulus $s_{\dagger,G}(t)$ that has the histogram distribution of a Gaussian with mean μ and variance σ^2.

Using cumulative probability distributions, $P_y(x) = \mathrm{Prob}(x < s_y)$, the nonlinearity F can be expressed by the cumulative probability distribution of the actual stimulus, $P_\dagger$, and the inverse cumulative probability distribution of a Gaussian signal, P_G^{-1} (the inverse

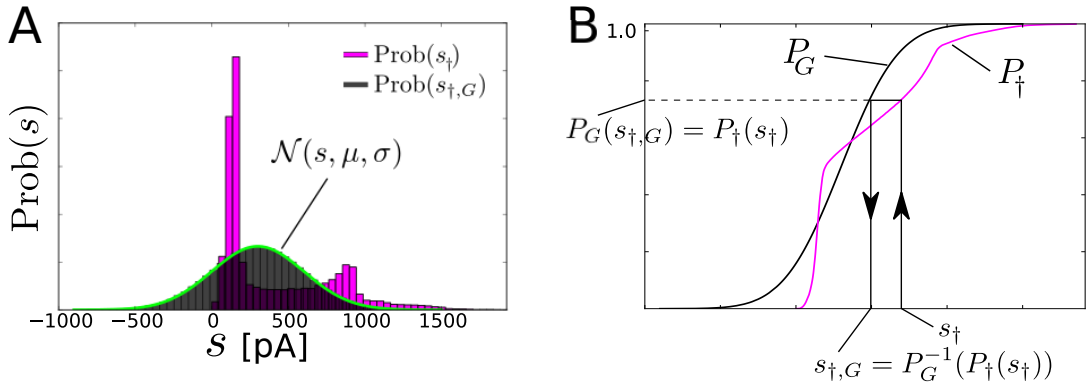

Figure 4.2.: Illustration of the nonlinear transformation of a non-Gaussian variable into a Gaussian variable. A) The histograms of the probability distributions of the actual (pink) and the transformed (transparent black) stimuli $s_\dagger(t)$ and $s_{\dagger,G}(t)$. The green curve that envelops the histogram of $s_{\dagger,G})(t)$ denotes the desired profile, i.e. the normal distribution $\mathcal{N}(s,\mu,\sigma)$. B) The cumulative probability distributions $P_\dagger$ and $P_{\dagger,G}$ of the actual (pink) and the desired Gaussian profile (black) respectively. The arrows indicate how a particular value $s_\dagger$ is transformed into the corresponding value $s_{\dagger,G}$ of the Gaussian signal.

of the prescribed probability distribution)

$$F(x,\mu,\sigma) = P_G^{-1}(P_\dagger(x),\mu,\sigma). \tag{4.10}$$

In Fig.4.2, the nonlinear transformation of a non-Gaussian distribution to the desired Gaussian distribution is illustrated. The histogram distribution of a non-Gaussian and transformed stimulus are plotted in Fig.4.2A. Due to the definition of the nonlinear transformation, the histogram of the transformed stimulus, $s_{\dagger,G}$, perfectly agrees with the desired normal distribution, $\mathcal{N}(s,\mu,\sigma)$ (green line). In Fig.4.2B, the cumulative probability distributions are shown and the transformation, eq.(4.9), is illustrated by arrows that indicate how a particular value of the non-Gaussian stimulus, $s_\dagger$, is transformed into the corresponding value of the Gaussian stimulus, $s_{\dagger,G}$.

The stimulus $s_{\dagger,G}(t)$ that results from this transformation has the desired Gaussian statistics. However, we also have to ensure the constraint of a cutoff frequency at 100 Hz. To this end, a second step in which a lowpass filter is applied sets all Fourier components that belong to frequencies larger than f_c to zero

$$\tilde{s}_{\dagger,f_c}(f) = \tilde{s}_{\dagger,G}(f)\Theta(f_c - f). \tag{4.11}$$

Here, $\Theta(f)$ is the Heaviside-function. This operation is again a nonlinear transformation of the stimulus and in general it is likely that it changes the histogram distribution such that the Gaussian signal becomes again a non-Gaussian signal.

In order to obtain a stimulus, $s_{\dagger,G,f_c}(t)$, that fulfills all constraints at the same time, we iteratively apply eq.(4.9) and eq.(4.11). I.e. we first give the stimulus the desired Gaussian profile, with the right mean and variance, then apply the lowpass filter to ensure the cutoff frequency and iteratively repeat this procedure. To ensure that all Fourier components for frequencies larger than f_c are truly equal to zero at the end of an iteration, we start the iteration with the transformation to Gaussian statistics and apply the frequency cutoff afterwards.

To quantify the convergence of the iterative process, we define a measure, Δ, to test if the statistics of the transformed stimulus are close enough to the desired Gaussian statistics:

$$\Delta = \frac{\int_{-\infty}^{\infty} |P_{\dagger,f_c}(s) - P_G(s)| \, \mathrm{d}s}{\int_{-\infty}^{\infty} |P_{G'}(s) - P_G(s)| \, \mathrm{d}s}. \tag{4.12}$$

Here, as a reference for two distinct cumulative probability distributions, $P_G(s)$ and $P_{G'}(s)$ are calculated from two Gaussian variables that have the same mean value, μ, but slightly differ in their standard deviations, σ and $\sigma' = 1.01\sigma$. Therefore, the denominator of eq.(4.12) normalizes the difference between the actual cumulative probability distribution, $P_{\dagger,f_c}(s)$, and the prescribed one, $P_G(s)$ (numerator), by a this reference value.

As termination criterion for the iteration, we use $\Delta < 0.1$. This means that the cumulative distribution of $s_{\dagger,G,f_c}(t)$ should differ from the desired Gaussian by less than 10% of what would be the deviation between two Gaussians that differ in their standard deviations by one percent. Typically, this criterion is fulfilled after 10-20 iterations such that the procedure returns a stimulus, $s_{\dagger,G,f_c}(t)$, that approximately satisfies all constraints.

To complete the procedure, we still need to decide how μ and σ^2 in eq.(4.9) are chosen. The stimulus variance $\sigma^2 = \sigma_0^2$ was fixed at the reference value variance which is an experimentally motivated constraint that is supposed to ensure the integrity of the stimulated neuron by restricting of the total power that is injected in the cell. Because the mean value of the input strongly affects the firing rate, we let it depend on the prescribed firing rate, $r_\dagger$, via the inverse firing-rate-vs-input-current relation for the white noise driven neuron,

i.e. the inverse of eq.(4.3):

$$\mu_\dagger = f_\mu^{-1}(r_\dagger), \tag{4.13}$$

$$\sigma_\dagger = \sigma_0. \tag{4.14}$$

Using the inverse firing-rate-vs-input-current relation is again an approximation because the calculated stimulus, $s_{\dagger,G,f_c}(t)$, is colored noise and the noise color can affect the firing rate (Brunel and Sergi, 1998). In the following, we will write $s_\dagger(t)$ instead of $s_{\dagger,G,f_c}(t)$ for the converged stimulus, to ease the notation.

Because we derived $s_\dagger(t)$ under strong approximations (eq.(4.8)) and performed some nonlinear transformations (eq.(4.9) and eq.(4.11)) that have been introduced in a very ad hoc way, we need to test to which extend the stimulus is able to evoke the desired spike train $x_\dagger(t)$.

4.5. Evoking a prescribed spike train in vivo

We have tested our procedure to evoke prescribed spike trains in real cortical neurons in vivo. For these experiments we restricted us to the case of prescribed statistics that match the reference statistics, i.e. $C_{V\dagger} = C_{V0}$ and $r_\dagger = r_0$. These values and the dynamic susceptibility χ_0 at the reference point have been estimated from white Gaussian noise stimulations as explained in ch.4.2. To this end, we generated 10 white noise stimuli of which each stimulus has been applied 10 times and lasted for 1 s. Between each stimulus representation a 1s gap was introduced such that the total number of 100 stimulations was applied within less than 4 minutes. From these data, we also calculated the intrinsic reliability, Γ_{ee}^{ref}, of the neuron by averaging the coincidence measure (eq.(1.26)) over pairs of spike trains that belong to the same stimulus. We then applied our procedure and injected the resulting stimulus into the very same neuron. We made recordings of five cells from which two cells have been stimulated with two stimulation intensities. Therefore, in total we generated seven data sets with 50-140 trials.

In Fig.4.3, the basic prescribed statistics, rate and CV, are compared to the statistics of the spike trains that have been evoked by our stimulus. The evoked and the prescribed firing rates are shown in Fig.4.3A. Data points are distributed along the diagonal (which would indicate a perfect agreement between prescribed and evoked rate) and show only minor deviations for most cases. Also for the CV a correlation between prescribed and evoked values can be observed (see Fig.4.3B), but most deviations from the optimal value on the diagonal tend towards larger evoked CVs. However, from our small data set it is

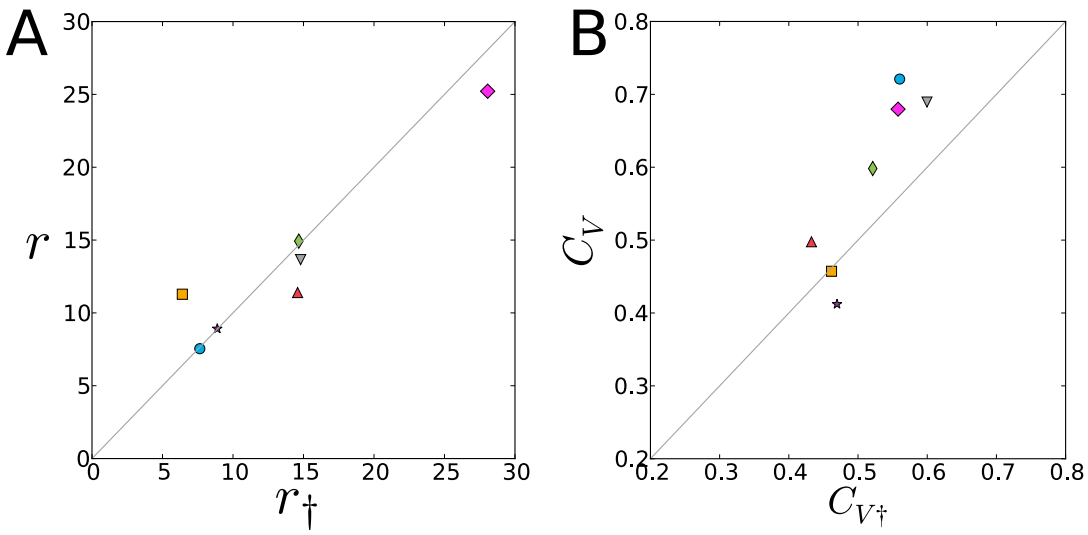

Figure 4.3.: Spike train statistics of the prescribed and the evoked spike trains (experimental data, in vivo). A) Scatter plot of the firing rate. B) Scatter plot of the Coefficient of variation (CV). The same symbol in A and B belong to the same data sets. In total, seven data sets out of 5 different neurons are shown. An optimal agreement would be achieved for values on the diagonal (gray line).

hard to judge whether this bias is a reliable observation.

In Fig.4.4, the coincidence measures are used to quantify to which extent the specific AP timing could be achieved. We compare three different values to each other: $\Gamma_{ee}^{\mathrm{ref}}$, the intrinsic reliability (i.e. the similarity between evoked spike trains) that has been estimated by white noise stimulation at the reference point; Γ_{ee}, the intrinsic reliability resulting from stimulation with the colored noise that comes out of our procedure; and Γ_{de} which is the similarity between prescribed and evoked spike trains.

The intrinsic reliability for the reference stimulation, $\Gamma_{ee}^{\mathrm{ref}}$, is plotted along the x-axis, while Γ_{ee} (blue symbols) and Γ_{de} (red symbols) are given on the y-axis. The first observation that we can make is that all data points are systematically above the diagonal. This means that our colored noise stimulus could generate reproducible spike trains with larger reliability as for the white noise case. The second observation is that the similarity between evoked and prescribed spike train, Γ_{de}, is larger than the intrinsic reliability for the same data set (red symbols are above blue symbols). Note that in this figure different data sets are separated by their intrinsic reliability along the x-axis such that vertically aligned symbols belong to the same data set. Thus, the similarity between the colored noise evoked spike trains and the target spike train was even higher than the similarity within the evoked spike trains. This is the case because the prescribed spike train lacks the

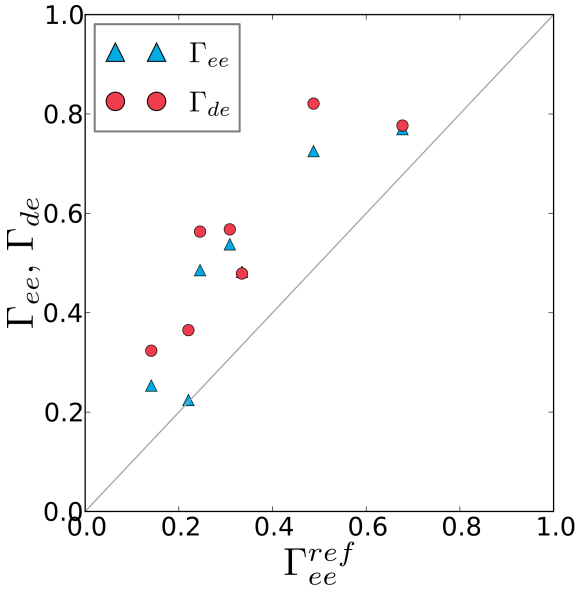

Figure 4.4.: Prescribed spike times can be evoked reliably in vivo. The trial-to-trial reliability in response to the colored noise (Γ_{ee}, blue triangles) and the similarity between prescribed spike trains and evoked trials (Γ_{de}, red circles) are plotted against the trial-to-trial reliability in response to white noise stimulation ($\Gamma_{ee}^{\mathrm{ref}}$). The colored noise evoked spike trains even more reliable than stimulation with white noise. The similarity between trials and desired spike train (Γ_{de}) exceeds the trial-to-trial reliability Γ_{ee}.

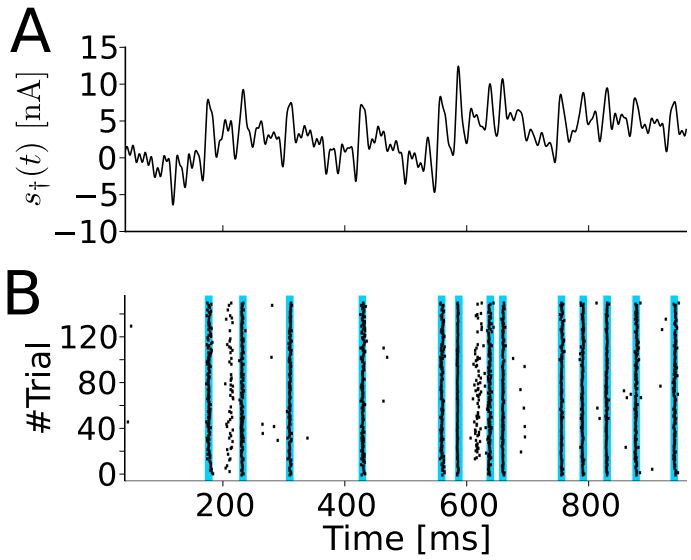

Figure 4.5.: A) Example stimulus calculated to evoke a desired spike train in a particular cell. B) Raster plot of spike trains (black dashes) generated by stimulation with the current shown in A. The desired spike times are marked as blue stripes in the raster plot and mostly agree well with the evoked spike times.

intrinsic noise of the individual trials and the evoked APs are jittered around the desired spike time.

A less abstract example of the performance is given in Fig.4.5. Panel A shows the stimulus and panel B the corresponding raster plot for one example cell, for which the spikes (black dots) appeared with high precision close to the prescribed times (blue lines). However, at around 200 ms and 610 ms the cell systematically generated APs that are not part of the prescribed spike train. It is likely that these systematic outliers are introduced by the constraints that we imposed on the stimulus.

Despite the finite intrinsic reliability and the weak systematic deviations from the prescribed spike train, we can conclude that this method has the ability to evoke prescribed spikes in a precise and reliable manner using juxtacellular stimulation in vivo in cortical neurons.

4.6. Deviations from the reference statistics (simulations)

Here, we test our method for the two neuron models motivated in ch.4.1. For the one-compartment model we analyze two distinct firing regimes, i.e. the suprathreshold (mean-driven) and subthreshold (fluctuations-driven) regime, while results for the two-

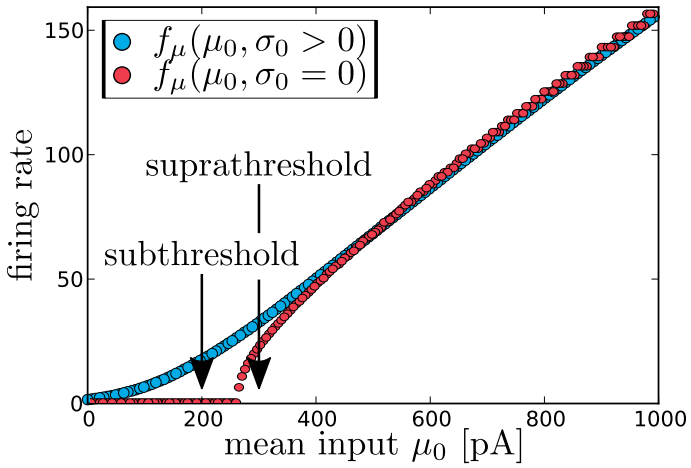

Figure 4.6.: Firing-rate-vs-input-current relation (eq.(4.3)) of the one-compartment model for the case with input noise ($\sigma_0 > 0$, blue) and without input noise ($\sigma_0 = 0$, red). The reference mean-input for the sub- and suprathreshold regime is indicated by the arrows and is given by $\mu_0 = 200\,\mathrm{pA}$ and $\mu_0 = 300\,\mathrm{pA}$ respectively.

compartment model are only given for the suprathreshold regime. The firing rate curve, of the one-compartment model for the case with input noise present ($\sigma_0 > 0$) and without input noise ($\sigma_0 = 0$), is given in Fig.4.6.

The susceptibility that is a central quantity in our procedure is shown in Fig.4.7 for the three cases. Because of the remarkable difference between one-compartment and two-compartment model, that show lowpass and highpass characteristics respectively, the comparison of the method's performance for these two models should give us an impression how robust it is w.r.t. changes in the properties of the neuronal dynamics.

In the simulations presented here, we particularly investigate how well prescribed spike trains with statistics that deviate from the reference values r_0 and $C_{V,0}$ can be evoked. Note that although changes in rate and CV are considered, we still use the susceptibility χ_0 estimated at the reference point to calculate the colored-noise stimulus.

4.6.1. Performance for the one-compartment model

In Fig.4.8, we show the performance of our method for the one-compartment model in the suprathreshold firing regime for the case where either prescribed rate, $r_\dagger$, or coefficient of variation, $C_{V\dagger}$, are varied around the reference values. The dotted lines indicate the reference statistics, r_0 and $C_{V,0}$, and the dashed diagonal line corresponds to an optimal agreement between evoked and prescribed rate (deviations from the diagonal lines quantify the failure in the respective statistics). Fig.4.8A illustrates that for fixed $C_{V\dagger} = C_{V0}$

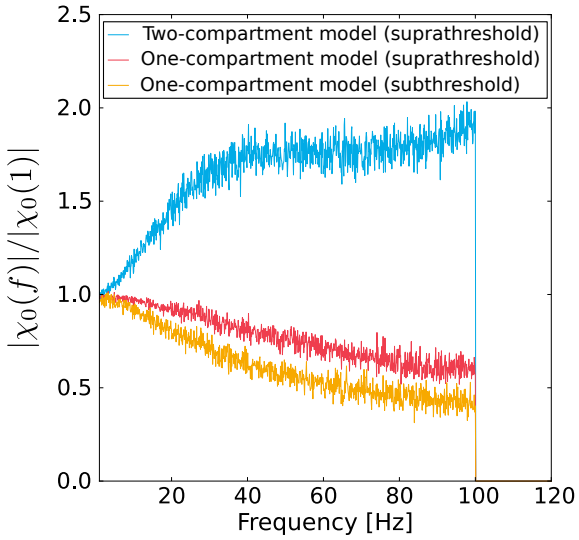

Figure 4.7.: Absolute value of the susceptibility for the three analyzed cases: i) Two-compartment model in the suprathreshold regime (blue), ii) one-compartment model in suprathreshold regime (red), iii) one-compartment model in subthreshold regime (yellow). In contrast to the one-compartment model that shows a lowpass characteristic, the two-compartment model has a pronounced highpass shape.

the evoked rate successfully matches the prescribed rate (the evoked rate is close to the diagonal that denotes the identity between evoked and prescribed statistics). A good agreement in the firing rates was to expect because we use the inverse firing-rate-vs-input current relation (eq.(4.13)) to define the mean input of the stimulus, i.e. the value of μ that evokes the prescribed firing rate in an IF model with bandpass-limited white noise. In principle, the noise color could induce deviations between prescribed and evoked rate, however, here this effect seems to be small.

In contrast to the firing rate, the CV is close to the prescribed value only for CVs smaller or equal to $C_{V,0}$, as we can see in Fig.4.8B (for this figure the mean input and the firing rate are fixed). Therefore, with our method it seems to be possible to reduce the variability of firing by changing the noise color, while it is more difficult to increase the variability (at least in comparison to the case of bandpass-limited white noise). It is likely that the problem of evoking spike trains with larger CVs is caused by our constraint of a fixed variance σ^2. However, by relaxing this constraint we would increase the total injected power, and thus risk a damage of the neuron.

Because Fig.4.8A revealed that the evoked firing rate matches the prescribed rate for all values of $r_\dagger$, it is reasonable to calculate spike-train similarity in terms of the coincidence

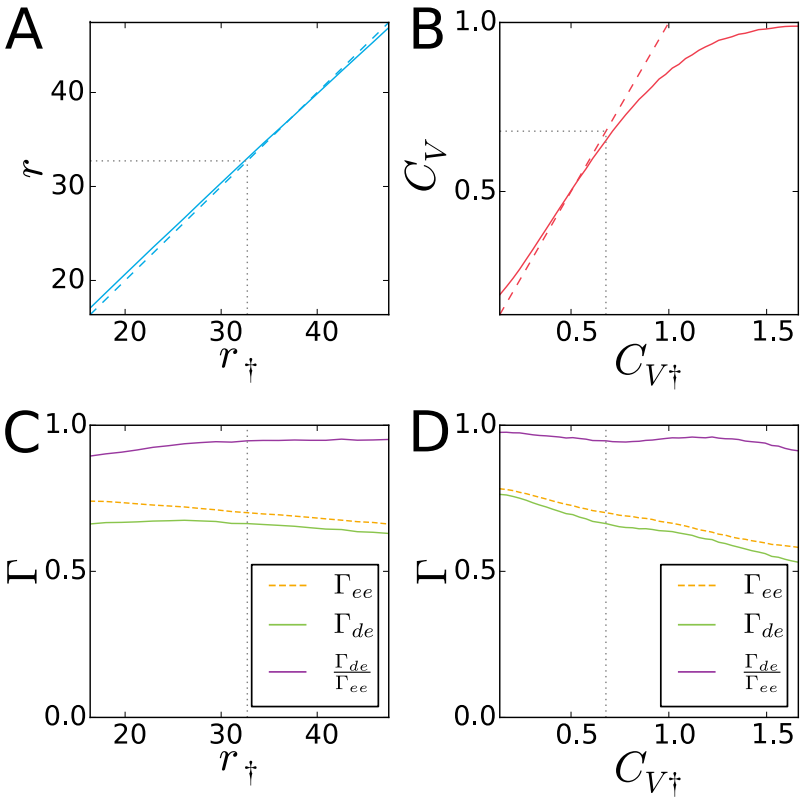

Figure 4.8.: One-compartment model; suprathreshold regime: Performance of the method in capturing the prescribed statistics and spike times: A) evoked rate r over the prescribed rate $r_\dagger$; B) evoked C_V over the prescribed $C_{V\dagger}$; C) intrinsic reliability, Γ_{ee} (middle, dashed curve), the similarity between evoked and prescribed spike trains, Γ_{de} (lower curve), and the ratio of both (upper curve) as functions of the prescribed firing rate $r_\dagger$; D) same as in C but versus prescribed $C_{V\dagger}$.

factor between different evoked spike trains, Γ_{ee}, and between evoked and prescribed spike trains, Γ_{de}. These measures and the ratio Γ_{de}/Γ_{ee} are shown in Fig.4.8C and D for variations in $r_\dagger$ and $C_{V\dagger}$ respectively. Over the whole range of firing rates (Fig.4.8C) both measures reveal $\Gamma_{ee} > \Gamma_{de} > 0.6$ and thus show a large intrinsic reliability and a large similarity between evoked and prescribed spike times. Furthermore, the evoked spike trains are roughly as similar to the prescribed spike train as they are similar to each other. This can be concluded from the observation that Γ_{de}/Γ_{ee} is close to one. Hence, our method appears to work equally well for a whole range of firing rates. In Fig.4.8D, the dependence of the similarity measures on the prescribed CV is plotted. As we can expect from the above considerations, the similarity decreases for a prescribed spike train with higher variability. In Fig.4.8, we only varied one statistic of the prescribed spike train at a time, either $r_\dagger$ or $C_{V\dagger}$, while the respective other parameter was kept at its reference value.

In Fig.4.9, output rate, CV, and the coincidence measures are shown as functions of both, $r_\dagger$ and $C_{V\dagger}$. To generate this figure, many numerical simulations have been performed: at each of the 920 prescribed parameter values (20 points on the $r_\dagger$-axis and 46 points on the $C_{V\dagger}$-axis) we generated 150 realizations of prescribed spike trains and applied the iterative scheme to each of those, yielding in total 138000 stimuli $s_\dagger(t)$. In this figure, we compare the results for the suprathreshold (left column) and the suprathreshold (right column) firing regime.

We find that for both firing regimes the prescribed rate is well matched by the simulations (Fig.4.9A1, A2), independent of the value of $C_{V\dagger}$. In contrast, the prescribed $C_{V\dagger}$ (Fig.4.9B1, B2) is achieved only for values that are close to or smaller than $C_{V,0}$. For larger prescribed values, $C_{V\dagger} > C_{V,0}$, we find for both firing regimes that the evoked CV is always smaller than the prescribed one and that these deviations are larger for large values of the prescribed firing rate, $r_\dagger$. In Fig.4.9C1, C2 and D1, D2, we plotted the similarity between evoked and prescribed spike trains, Γ_{de}, and the ratio of this similarity and the intrinsic reliability, Γ_{ee}, for the suprathreshold and subthreshold firing regime respectively. In both regimes the method performs reasonable well with $\Gamma_{sd} > 0.5$ for all regions in which the prescribed $C_{V\dagger}$ was successfully generated (Fig.4.9C1, C2). In the suprathreshold firing regime, the similarity between evoked and prescribed spike trains decreases for larger prescribed $C_{V\dagger}$ and $r_\dagger$ (Fig.4.9C1), while in the subthreshold case it shows a decrease at small values of $C_{V\dagger}$. For the suprathreshold regime, the ratio, Γ_{de}/Γ_{ee}, attains values close to one for the whole region under investigation (Fig.4.9D). In the subthreshold regime we observe a decrease of Γ_{de}/Γ_{ee} at small values of the CV (Fig.4.9D2), which is related to the decrease of Γ_{de} in Fig.4.9C2.

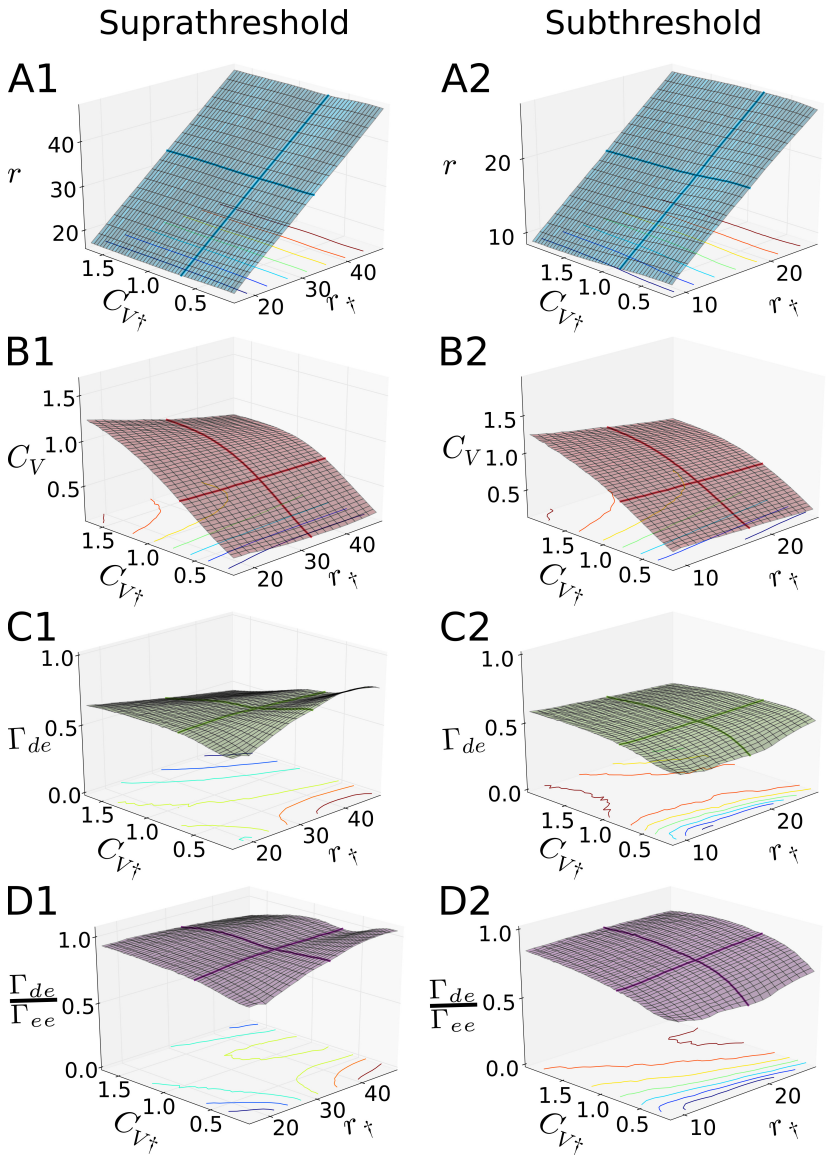

Figure 4.9.: One-compartment model; suprathreshold regime (left column); subthreshold regime (right column): Comparison between prescribed and evoked rate and coefficient of variation (A1, A2, B1, B2) and between prescribed and evoked spike times (C1, C2, D1, D2). Thick lines within the surfaces indicate either $r_\dagger = r_0$ or $C_{V\dagger} = C_{V,0}$ and the intersection point corresponds to the reference statistics r_0, $C_{V,0}$. A1,2) The evoked firing rate in the plane of prescribed rate $r_\dagger$ and $C_{V\dagger}$. B1,2) Same as A but with evoked C_V on the z-axis. C1,2) Same as A but with the similarity between prescribed and evoked spike trains Γ_{de} on the z-axis. D1,2) Same as A but the ratio of similarity and intrinsic reliability Γ_{de}/Γ_{ee} on the z-axis.

Besides the comparison of evoked and prescribed spike train characteristics, we can analyze the statistics of the stimulus that is generated by our method. In contrast to the commonly studied situation, that is to analyze the neuronal response to stochastic stimuli with given statistics, our approach is somehow the reverse situation: The output statistics are fixed and the corresponding input current is computed under the constraints of finite cutoff, Gaussianity, given mean and fixed variance. This latter constraint imposes a constant area under the power spectrum up to f_c. However, the distribution of power, i.e. the noise color, is allowed to evolve freely.

In Fig.4.10, the power spectra, $S_{s_\dagger s_\dagger}(f)$, for stimuli that correspond to different prescribed $r_\dagger$ and $C_{V\dagger}$ are shown. Here, we only present spectra that correspond to cases in which the prescribed and the evoked CV match well ($C_V \approx C_{V\dagger} \leq C_{V,0}$).

For neurons that fire more regularly (with a low CV), the power spectra have a sharp peak around the respective firing rate (Fig.4.10A1, A2). Therefore, a regular firing seems to be supported best if the noise power is distributed such that the main power is located around the firing rate. Because the mean input μ_0 is larger for the suprathreshold regime, in this case also the firing rate is larger (see Fig.4.7 blue curve, i.e. the mean-dependent firing rate with input noise present). Therefore, the peaks of the suprathreshold spectra (Fig.4.10A1) are at larger frequencies than this is the case for the subthresold case (Fig.4.10A2).

With increasing irregularity (higher CV) these peaks decrease and broaden and the power spectra become more similar for different values of the prescribed firing rate. For this model, the stimulus power spectra are reduced at low frequencies and this is stronger in the case of the subthreshold regime. One reason for this reduction of the power spectra is the different shape of the susceptibility (Fig.4.7) that shows a more pronounced lowpass characteristic for the subthreshold case. Due to the appearance of the susceptibility in eq.(4.8), the power spectrum of our first guess for the colored stimulus is strongly affected by this quantity.

In eq.(4.8), the division by χ_0, i.e. a lowpass function, amplifies the Fourier components of the stimulus at higher frequencies. For stronger decreasing χ_0 this effect is more pronounced. However, due to the iterative steps that impose the constraints of Gaussian statistics and finite-cutoff frequency, the final stimulus is a nonlinearly transformed variant of eq.(4.8), and therefore the above line of arguments is certainly not strict.

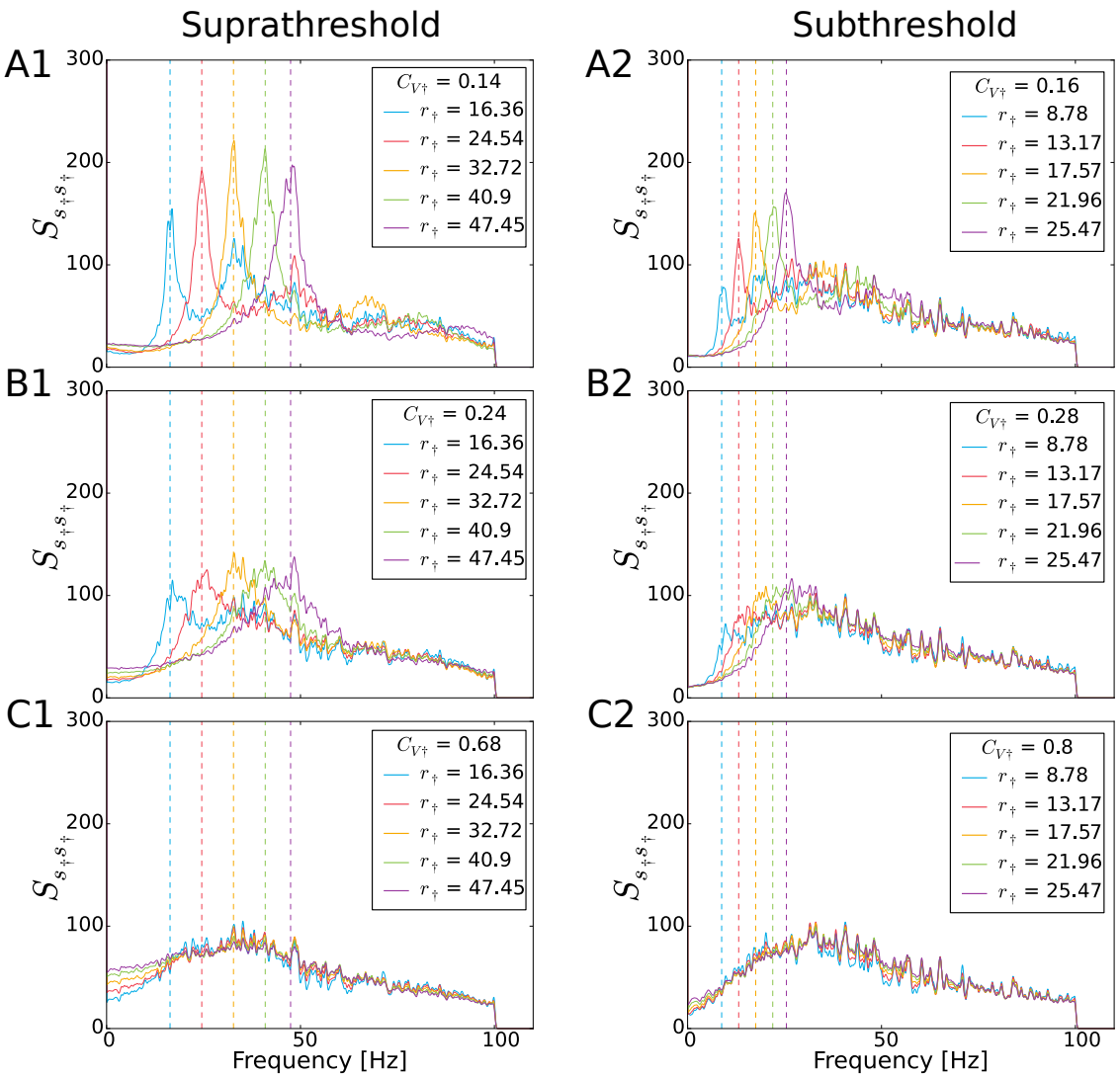

Figure 4.10.: One-compartment model; suprathreshold regime (left column); subthreshold regime (right column): Power spectra of the evoked stimuli for different values of $r_\dagger$ and $C_{V\dagger}$ as indicated. Different rates are color-coded and marked by the vertical dashed lines at the respective frequency values.

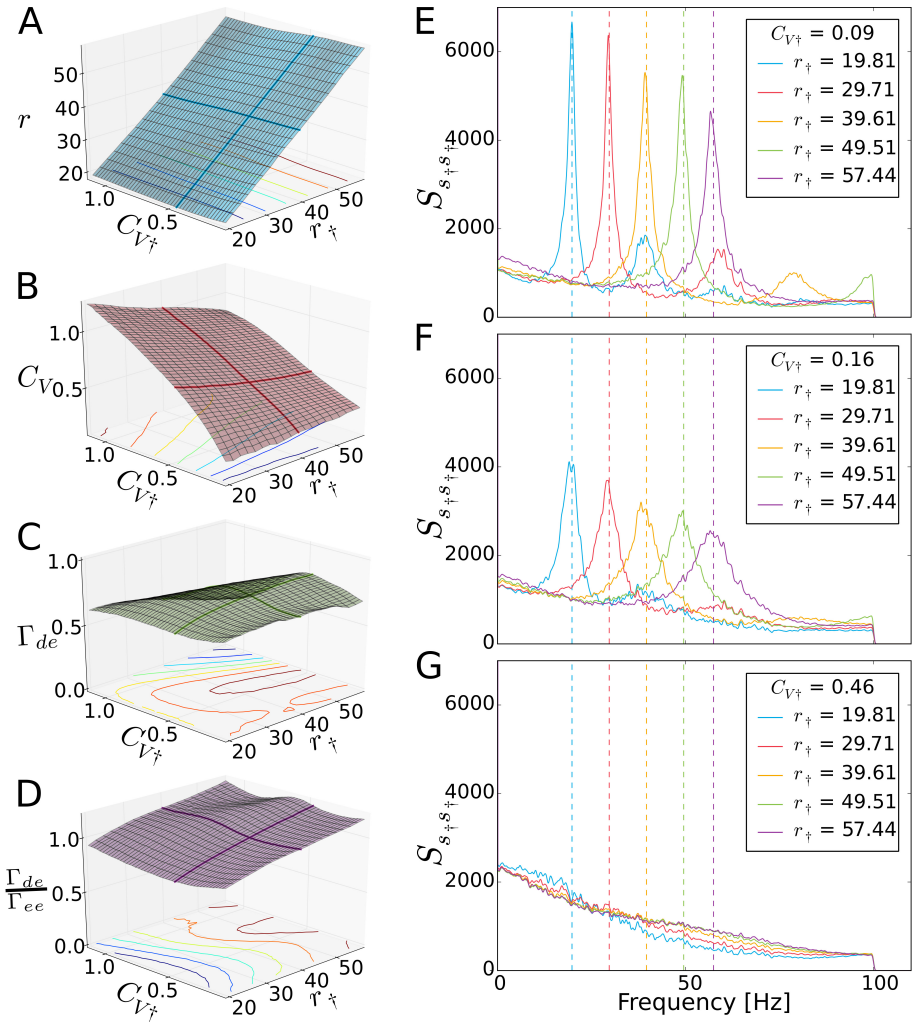

Figure 4.11.: Two-compartment model; suprathreshold regime: The performance of the two-compartment EIF model plotted in the ($r_\dagger$, $C_{V\dagger}$)-plane (A-D). The lines on the ground denote contour lines of equal height, the thick lines within the surfaces mark the cases where either $r_\dagger = r_0$ or $C_{V\dagger} = C_{V,0}$. A) The evoked firing rate in the plane of prescribed rate $r_\dagger$ and $C_{V\dagger}$. B) Same as A but C_V on the z-axis. C) Same as A but Γ_{de} on the z-axis. D) Same as A but Γ_{de}/Γ_{ee} on the z-axis. E)- G) The power spectra of the stimuli for different $r_\dagger$ and $C_{V\dagger}$. Different rates are color-coded and marked by the vertical dashed lines at the respective frequency values.

4.6.2. Performance for the two-compartment model

From Fig.4.7 can be seen that the susceptibilities of one- and two-compartment model reveal qualitatively different dynamics. We therefore use the comparison of the performance of our method for the two models is an indicator for the robustness of the method.

The same analysis as for the one-compartment model in ch.4.6.1 can been done for the two-compartment model and is summarized in Fig.4.11. Because this model consists of two compartments, has different transfer properties, and the stimulus is stronger (because it reflects the juxtacellular situation), we find quantitative differences in all statistical measures. However, in comparison to the one-compartment model the qualitative overall appearance is quite similar and reveals a good agreement between prescribed and evoked spike trains. This is reflected by the observations that the prescribed firing rate is well matched for all parameters (Fig.4.11A) while the CV can be matched only for firing that is more or equally regular to that at the reference value (Fig.4.11B). For all parameter values with a good match of the basic spike train statistics, a significant similarity between prescribed spike train and output spike train, $\Gamma_{de} > 0.5$, is obtained (Fig.4.11C). The ratio Γ_{de}/Γ_{ee} (Fig.4.11D) is close to one (or even larger than one) which means that on average the evoked spike train is more similar to the prescribed spike train than it is to a spike train evoked in another trial.

As for regular firing (small $C_{V\dagger}$) in the one-compartment model, the power spectra of the stimuli show pronounced peaks at the prescribed firing rates (Fig.4.11E). With increasing $C_{V\dagger}$ these peaks decrease, broaden, and vanish for large CVs such that the spectra become similar for different $r_\dagger$ (Fig.4.11F, G). In contrast to the one-compartment model, the power spectra continuously decrease with increasing frequency. By means of the same arguments that we used in the discussion of the reduced power spectra at low-frequencies for the one-compartment model, this can be explained by the shape of the susceptibility which is highpass for this model (see Fig.4.7). The highpass shape of the susceptibility (Fig.4.7) is turned into a lowpass shape in the power spectrum of the stimulus (Fig.4.11G) by the division with χ_0 in eq.(4.8). Again this argument is not rigorous because, in order to impose our constraints, the stimulus is nonlinearly transformed afterwards.

4.7. Summary

In this chapter, we addressed the question how to compute a Gaussian colored noise stimulus that evokes a prescribed spike train in a particular neuron. Because of the experimentally motivated problem to ensure reliable spike extraction and the integrity of

the neuron, we imposed certain constraints on this stimulus: i) a finite cutoff frequency of 100 Hz, ii) a given mean and variance, iii) Gaussianity.

We first determined reference statistics (i.e. the firing rate, CV, susceptibility and the firing-rate-vs-current relation) of the particular neuron by stimulation with bandpass-limited white Gaussian noise. Then, we simulated a PIF model to define a prescribed spike train with a rate and CV that is derived from the reference values. Using a linear-response ansatz, we computed a first guess of a stimulus that is supposed to evoke the prescribed spike train. This was done by means of the Fourier transform of this spike train and the susceptibility of the neuron. Subsequently, this stimulus was nonlinearly transformed by an iterative scheme to impose our constraints.

We tested the performance of this procedure for real neurons in vivo and for simulations of different neuron models and firing regimes. For most values of rate, CV, and a reasonable agreement between prescribed spike trains and those that are evoked by the colored noise stimuli could be achieved.

We also calculated the power spectra of the stimuli and made several observations: i) For regular firing (low values of the CV) the power spectra are peaked around the firing rate. For a given area under the power spectrum, this distribution of noise power seems to be the best choice to decrease the ISI variability. ii) At more irregular firing (high CV) the power spectra for different values of the prescribed firing rate become more and more similar and converge to a shape that seems to be strongly influenced by the neurons susceptibility. Because in general it is difficult to predict how the noise color will affect the firing statistics, these are interesting results that are worth to be further explored.

Chapter 5.

Concluding remarks

The intersection between theoretical investigations and new experimental methods is a fertile ground for gaining new insights into the functioning of the nervous system. Juxtacellular stimulation is a comparable simple technique to stimulate individual neurons in vivo, and therefore it is of broad interest to infer its advantages and limitations. In this thesis, we have studied the dynamics of cortical neurons that have been stimulated with juxtacellularly applied stimuli and discussed from the theoretical point of view how the obtained results can be explained by means of physiological properties of the investigated cells (this has been done by using simple neuron models). In order to contribute to the development of advantages of juxtacellular stimulation, we extended its scope of application by proposing a method to evoke prescribed spike trains in cortical neurons in vivo.

In Chapter 2, we showed that applying a filter on the juxtacellular raw-voltage, to remove the frequency components of the input stimulus, enabled us to reliably extract spike times by application of a threshold criterion. To this end, it is important that the frequency band of the stimulus and that of the APs do not infer too much. We demonstrated that stimulation with bandpass-limited noise with a cutoff frequency up to 200 Hz and harmonic stimuli with arbitrary oscillation frequency could successfully be filtered out. We showed that stimulation with bandpass-limited white frozen Gaussian-noise stimuli could reliably evoke reproducible spike trains with APs timed with ms precision. The analysis of the data revealed that the investigated neurons show a surprisingly strong support of high-frequent stimulus components. For many cells the input-output cross-spectrum even increased with frequency, which was also observed for the vector strength for some cells. Besides this strong support of the high frequent stimulus power, we found a sustained broadband coding of information that is indicated by a flat shape of the spectral coherence.

In Chapter 3, we used simple IF neuron models in order to quantitatively reproduce all spike-train and input-output statistics as well as the precise times of APs that have been observed in the experiment. We considered a one-compartment and a two-compartment

EIF model (with additional white noise to account for synaptic input in vivo) in which the stimulus was applied to the somatic compartment. We showed that including the spatial structure by the additional dendritic compartment enhanced the high-frequency transfer of the neuron model in the subthreshold regime, and can be sufficient to closely match the subthreshold dynamics of compartment models that describe the dendritic tree in more detail. In contrast, the simpler one-compartment model was not able to match the shape of the subthreshold dynamics. By parameter optimization, we could achieve a remarkably agreement between two-compartment model and experiment that could not be achieved for the one-compartment model. In particular, the two-compartment model was able to match many independent statistics as well as the intrinsic reliability and the precise AP times. We could show that the dendritic compartment enabled the two-compartment model to account for the broadband shape of the coherence, which is qualitatively different from the lowpass characteristic that was observed for the one-compartment model.

In Chapter 4, we extended the approach of evoking reliable but random spike trains (as in Chapter 2). Here, we defined a prescribed spike train in advance and then computed the corresponding stimulus that is supposed to evoke this particular train. To this end, we did not restricted us to the case of white noise but allowed the power spectrum of the stimulus to evolve freely within our method. However, we adhered to the constraints of Gaussianity (with particular mean and variance) and finite cutoff frequency. It was shown in experiments and simulations that the prescribed spike train could be evoked with high accuracy if it had a rate and CV that agreed with the reference values that have been estimated under white noise stimulation. In simulations, we also showed that prescribed spike trains with firing statistics that deviate from these reference values could be evoked. In particular, deviations in the firing rate could be accounted for by adapting the mean of the stimulus. However, deviations in the CV where matched well only for CVs smaller or equal to the prescribed one which is likely due to the constraint of a fixed variance of the stimulus. Interestingly we observed that the distribution of stimulus power (noise color) for low CVs is peaked around the firing rate, while it seems to be almost independent of the firing rate for more irregular firing.

Appendix A.

Parameter values from the two-compartment model fit

The parameter values of the two-compartment model that resulted from the optimization in ch.3. Cell IDs correspond to the labels used in Fig.3.9:

dimensionless parameter:

Cell ID	$\alpha g_s \Delta_T$	τ_s[ms]	τ_d[ms]	$\frac{V_{Th}}{\Delta_T}$	$\frac{g_c}{g_s}$	$\frac{g_c}{g_d}$	$\frac{\alpha^2 D_s}{(g_s \Delta_T)^2}$[ms]	$\frac{D_d}{(g_d \Delta_T)^2}$[ms]	$\frac{\mu_d}{g_d \Delta_T}$
1	25.0	94.0	30.1	72.5	51.6	3.6	27.0	818.6	65.9
2	12.5	74.9	14.1	72.4	56.2	3.9	239.1	443.7	62.0
3	42.3	99.3	45.2	61.3	94.6	2.7	46.6	0.8	66.4
4	30.2	69.3	12.7	67.2	101.0	1.1	48.0	32.2	66.3
5	39.8	87.2	23.2	63.9	65.4	1.4	27.8	58.3	65.5
6	14.1	86.0	9.4	68.8	76.4	1.6	219.9	61.9	66.4
7	8.4	86.7	83.3	76.1	97.1	6.1	35.0	4235.6	64.2
8	17.5	80.6	28.4	74.7	17.9	0.9	877.3	4354.2	57.0
9	13.0	43.4	25.2	71.1	42.1	0.8	42.2	72.8	66.0
10	18.7	55.8	84.3	75.3	32.1	9.9	79.5	19993.6	59.3

biophysical parameter:

These parameter values have been calculated for $\Delta_T = 0.5\,\mathrm{mV}$.

Cell	g_s[nS]	τ_s[ms]	τ_d[ms]	V_{Th}[mV]	g_d[nS]	g_c[nS]	D_s[pA^{2}s]	D_d[pA^{2}s]	μ_d[pA]	α
1	1.8	94.0	30.1	36.2	26.2	93.0	0.02	140.1	862.2	27.8
2	1.8	74.9	14.1	36.2	25.7	100.1	0.2	73.2	795.8	14.1
3	0.8	99.3	45.2	30.7	29.3	79.5	0.008	0.16	970.3	100.7
4	0.45	69.3	12.7	33.6	41.2	46.1	0.002	13.7	1366.9	132.3
5	0.78	87.2	23.2	31.9	37.0	51.0	0.004	20.0	1211.3	102.03
6	0.74	86.0	9.4	34.4	34.5	56.8	0.03	18.5	1146.8	37.8
7	1.5	86.7	83.3	38.1	24.1	147.4	0.02	614.5	773.4	11.1
8	2.1	80.6	28.4	37.3	43.4	37.5	1.0	2046.3	1236.5	16.6
9	0.9	43.4	25.2	35.4	46.7	39.1	0.009	39.7	1541.2	27.8
10	5.6	55.8	84.3	37.7	18.3	180.6	0.6	1669.4	542.2	6.6

Appendix B.

Pseudo-algorithm

A pseudo-algorithm is given to illustrate the procedure to calculate $s_\dagger(t)$ in a more compact way and to support people that want to reproduce our results.

procedure CALCULATE STIMULUS
- define neuron model / prepare a real neuron ▷ eq.(3.1), eq.(3.2) and eq.(3.3)
- set μ_0 and σ_0 to suitable values
- ▷ determination of the reference statistics
- **for** η in reasonable set of realizations **do**
  - $s_0(t) = \mu_0 + \sigma_0\eta(t)$ ▷ eq.(4.1)
  - stimulate neuron with $s_0(t)$
  - measure output spike trains
  - estimate r_0, $C_{V,0}$ and $\chi_0(f)$
- **end for**
- ▷ estimate firing-rate vs input-current relation
- **for** μ in plausible range around μ_0 **do**
  - **for** s_0 in reasonable set of realizations **do**
    - stimulate neuron with $s_0(t) - \mu_0 + \mu$
    - measure output firing-rate $f_\mu(\mu, \sigma^2)$
  - **end for**
- **end for**
- set $r_\dagger$ and $C_{V\dagger}$ in a range around r_0 and $C_{V,0}$
- $\alpha = r_\dagger$ ▷ eq.(4.5)
- $D = \frac{r_\dagger C_{V\dagger}^2}{2}$ ▷ eq.(4.5)
- stimulate PIF with $\alpha + \sqrt{2D}\xi(t)$ ▷ eq.(4.4)
- $\rightarrow x_\dagger(t)$
- $\tilde{x}_\dagger(f) = \mathcal{F}(x_\dagger)$ ▷ Fourier transform
- $\tilde{s}_\dagger(f) = \tilde{x}_\dagger/\chi_0$ ▷ eq.(4.8)

$s_\dagger(t) = \mathcal{F}^{-1}(\tilde{s}_\dagger(f))$ ▷ Inverse Fourier transform
$\mu_\dagger = f_\mu^{-1}(r_\dagger, \sigma_0)$ ▷ eq.(4.13)
while $\Delta > 0.1$ **do**
$s_\dagger(t) \to P_\dagger(s_\dagger)$ ▷ estimating cumulative prob.
$s_{\dagger,G}(t) = P_G^{-1}(P_\dagger(s_\dagger(t)), \mu_\dagger, \sigma_0^2)$ ▷ eq.(4.9)
$\tilde{s}_{\dagger,f_c}(f) = \mathcal{F}(s_{\dagger,G}(t))\Theta(f_c - f)$ ▷ eq.(4.11)
$s_\dagger(t) = \mathcal{F}^{-1}(\tilde{s}_{\dagger,f_c}(f))$
calculate $\Delta(s_\dagger(t))$ ▷ eq.(4.12)
end while
return $s_\dagger(t)$
end procedure

Bibliography

Abbott, L. F. Lapicque's introduction of the integrate-and-fire model neuron (1907). *Brain Res Bull*, 50(5-6):303, 1999.

Antic, S. Action potentials in basal and oblique dendrites of rat neocortical pyramidal neurons. *J Physiol*, 550(1):35, 2003.

Auger, A., Hansen, N., Zerpa, J. P., Ros, R., and Schoenauer, M. Experimental comparisons of derivative free optimization algorithms. In Vahrenhold, J., editor, *Experimental Algorithms*, volume 5526 of *Lecture Notes in Computer Science*, page 3. Springer Berlin Heidelberg, 2009.

Badel, L., Lefort, S., Brette, R., Petersen, C. C. H., Gerstner, W., and Richardson, M. J. E. Dynamic I-V curves are reliable predictors of naturalistic pyramidal-neuron voltage traces. *J. Neurophysiol.*, 99:656, 2008.

Barnett, A. and Weaver, J. C. Electroporation: a unified, quantitative theory of reversible electrical breakdown and mechanical rupture in artificial planar bilayer membranes. *J. Efectruanol. Chem.. and constituting*, 320:163, 1991.

Bauermeister, C., Schwalger, T., Russell, D., Neiman, A. B., and Lindner, B. Characteristic effects of stochastic oscillatory forcing on neural firing: Analytical theory and comparison to paddlefish electroreceptor data. *PLoS Comput. Biol.*, 9:e1003170, 2013.

Bekkers, J. M. Changes in dendritic axial resistance alter synaptic integration in cerebellar purkinje cells. *Biophys J*, 100(5):1198, 2011.

Benedetti, B. L., Takashima, Y., Wen, J. A., Urban-Ciecko, J., and Barth, A. L. Differential wiring of layer 2/3 neurons drives sparse and reliable firing during neocortical development. *Cereb Cortex*, 23(11):2690, 2013.

Benz, R., Beckers, F., and Zimmermann, U. Reversible electrical breakdown of lipid bilayer membranes: a charge-pulse relaxation study. *J Membr Biol*, 48(2):181, 1979.

Bernardi, D. and Lindner, B. A frequency-resolved mutual information rate and its application to neural systems. *J. Neurophysiol.*, 113:1342, 2015.

Borst, A. and Theunissen, F. Information theory and neural coding. *Nat. Neurosci.*, 2: 947, 1999.

Boucsein, C., Tetzlaff, T., Meier, R., Aertsen, A., and Naundorf, B. Dynamical response properties of neocortical neuron ensembles: Multiplicative versus additive noise. *J. Neurosci.*, 29:1006, 2009.

Brecht, M., Schneider, M., Sakmann, B., and Margrie, T. W. Whisker movements evoked by stimulation of single pyramidal cells in rat motor cortex. *Nature*, 427:704, 2004.

Brette, R. Generation of correlated spike trains. *Neural Comput.*, 02:188, 2009.

Brette, R. and Gerstner, W. Adaptive exponential integrate-and-fire model as an effective description of neuronal activity. *J. Neurophysiol.*, 94:3637, 2005.

Brunel, N. and Sergi, S. Firing frequency of leaky integrate-and-fire neurons with synaptic current dynamics. *J. Theor. Biol.*, 195:87, 1998.

Brunel, N., Chance, F. S., Fourcaud, N., and Abbott, L. F. Effects of synaptic noise and filtering on the frequency response of spiking neurons. *Phys. Rev. Lett.*, 86:2186, 2001.

Chotard, A., Auger, A., and Hansen, N. Cumulative step-size adaptation on linear functions. In Coello, C. A., Cutello, V., Deb, K., Forrest, S., Nicosia, G., and Pavone, M., editors, *Parallel Problem Solving from Nature - PPSN XII*, volume 7491 of *Lecture Notes in Computer Science*, page 72. Springer Berlin Heidelberg, 2012.

Clay, J. R. A stochastic analysis of the graded excitatory response of nerve membrane. *J. theor. Biol.*, 59(1):141, 1976.

Clopath, C., Jolivet, R., Rauch, A., Luescher, H.-R., and Gerstner, W. Predicting neuronal activity with simple models of the threshold type: Adaptive Exponential Integrate-and-Fire model with two compartments. *Neurocomputing*, 70:1668, 2007.

Connors, B. W., Gutnick, M. J., and Prince, D. A. Electrophysiological properties of neocortical neurons in vitro. *J Neurophysiol*, 48(6):1302, 1982.

Coombs, J. S., Eccles, J. C., and Fatt, P. Excitatory synaptic action in motoneurones. *J Physiol*, 130:374, 1955.

Cox, D. R. and Lewis, P. A. W. *The Statistical Analysis of Series of Events*. Chapman and Hall, London, 1966.

Dayan, P. and Abbott, L. F. *Theoretical Neuroscience*. MIT Press, Cambridge MA, 2001.

Deneve, S. and Machens, C. K. Efficient codes and balanced networks. *Nat. Neurosci.*, 19:375, 2016.

DeWeese, M. and Bialek, W. Information flow in sensory neurons. *Nuovo cimento D.*, 17: 733, 1995.

Doose, J. and Lindner, B. Evoking prescribed spike times in stochastic neurons. *Phys Rev E*, In press, 2017.

Doose, J., Doron, G., Brecht, M., and Lindner, B. Noisy juxtacellular stimulation in vivo leads to reliable spiking and reveals high-frequency coding in single neurons. *J. Neurosci.*, 36:11120, 2016.

Doron, G. and Brecht, M. What single-cell stimulation has told us about neural coding. *Philosophical Transactions of the Royal Society of London B: Biological Sciences*, 370 (1677), 2015.

Doron, G., Heimendahl, M., Schlattmann, P., Houweling, A., and Brecht, M. Spiking irregularity and frequency modulate the behavioral report of single-neuron stimulation. *Neuron*, 81(3):653, 2017.

Ermentrout, G. B. and Terman, D. H. *Mathematical Foundations of Neuroscience*, chapter Dendrites, page 39. Springer, 2010.

Eyal, G., Mansvelder, H. D., de Kock, C. P. J., and Segev, I. Dendrites impact the encoding capabilities of the axon. *J Neurosci*, 34(24):8063, 2014.

Feldmeyer, D., Lübke, J., Silver, R. A., and Sakmann, B. Synaptic connections between layer 4 spiny neurone-layer 2/3 pyramidal cell pairs in juvenile rat barrel cortex: physiology and anatomy of interlaminar signalling within a cortical column. *J Physiol*, 538 (Pt 3):803, 2002.

Ferster, D. and Jagadeesh, B. Epsp-ipsp interactions in cat visual cortex studied with in vivo whole- cell patch recording. *J. Neurosci.*, 12:1262, 1992.

Fisch, K., Schwalger, T., Lindner, B., Herz, A., and Benda, J. Channel noise from both slow adaptation currents and fast currents is required to explain spike-response variability in a sensory neuron. *J. Neurosci.*, 32:17332, 2012.

Fourcaud, N. and Brunel, N. Dynamics of the firing probability of noisy integrate-and-fire neurons. *Neural Comput.*, 14:2057, 2002.

Fourcaud-Trocmé, N., Hansel, D., van Vreeswijk, C., and Brunel, N. How spike generation mechanisms determine the neuronal response to fluctuating inputs. *J. Neurosci.*, 23: 11628, 2003.

Gabbiani, F. Coding of time-varying signals in spike trains of linear and half-wave rectifying neurons. *Network-Comp. Neural.*, 7:61, 1996.

Gentet, L. J., Stuart, G. J., and Clements, J. D. Direct measurement of specific membrane capacitance in neurons. *Biophys J*, 79(1):314, 2000.

Gerstein, G. L. and Mandelbrot, B. Random walk models for the spike activity of a single neuron. *Biophys J*, 4:41, 1964.

Gerstner, W., Kistler, W., Naud, R., and Paninski, L. *Neuronal Dynamics*. Cambridge University Press, 2014.

Glaser, R. W., Leikin, S. L., Chernomordik, L. V., Pastushenko, V. F., and Sokirko, A. I. Reversible electrical breakdown of lipid bilayers: formation and evolution of pores. *Biochim Biophys Acta*, 940(2):275, 1988.

Gold, C., Henze, D., Koch, C., and Buzsáki, G. On the origin of the extracellular action potential waveform: A modeling study. *J Neurophysiol*, 95(5):3113, 2006.

Goldberg, J. M. and Brown, P. B. Response of binaural neurons of dog superior olivary complex to dichotic tonal stimuli: some physiological mechanisms of sound localization. *J Neurophysiol*, 32(4):613, 1969.

Golding, N., Mickus, T., Katz, Y., Kath, W., and Spruston, N. Factors mediating powerful voltage attenuation along ca1 pyramidal neuron dendrites. *J Physiol*, 568(1):69, 2005.

Gonzalez-Islas, C. and Hablitz, J. J. Dopamine enhances epscs in layer ii-iii pyramidal neurons in rat prefrontal cortex. *J Neurosci*, 23(3):867, 2003.

Hansen, N. *The CMA Evolution Strategy: A Comparing Review*, page 75. Springer Berlin Heidelberg, Berlin, Heidelberg, 2006.

Hansen, N. and Baudis, P. Python module cma, 2008 - 2015. [Online; accessed 5-June-2015].

Hansen, N. and Kern, S. Evaluating the cma evolution strategy on multimodal test functions. In Yao, X., Burke, E. K., Lozano, J. A., Smith, J., Merelo-Guervós, J. J., Bullinaria, J. A., Rowe, J. E., Tiňo, P., Kabán, A., and Schwefel, H.-P., editors, *Parallel Problem Solving from Nature - PPSN VIII*, volume 3242 of *Lecture Notes in Computer Science*, page 282. Springer Berlin Heidelberg, 2004.

Hansen, N. and Ostermeier, A. Adapting arbitrary normal mutation distributions in evolution strategies: The covariance matrix adaptation. page 312. Morgan Kaufmann, 1996.

Hansen, N. and Ostermeier, A. Completely derandomized self-adaptation in evolution strategies. *Evol Comput*, 9(2):159, 2001.

Hansen, N., Müller, S. D., and Koumoutsakos, P. Reducing the time complexity of the derandomized evolution strategy with covariance matrix adaptation (cma-es). *Evol. Comput.*, 11(1):1, 2003.

Harrison, P. M., Badel, L., Wall, M. J., and Richardson, M. J. E. Experimentally verified parameter sets for modelling heterogeneous neocortical pyramidal-cell populations. *PLoS Comput Biol*, 11(8):1004165, 2015.

Heinricher, M. *Microelectrode Recording in Movement Disorder Surgery*, chapter Principles of Extracellular Single-Unit Recording, pages 8–13. Thieme, 2004.

Hertäg, L., Hass, J., Golovko, T., and Durstewitz, D. An approximation to the adaptive exponential integrate-and-fire neuron model allows fast and predictive fitting to physiological data. *Front Comput Neurosci*, 6:62, 2012.

Hestrin, S. Different glutamate receptor channels mediate fast excitatory synaptic currents in inhibitory and excitatory cortical neurons. *Neuron*, 11(6):1083, 1993.

Hestrin, S., Sah, P., and Nicoll, R. A. Mechanisms generating the time course of dual component excitatory synaptic currents recorded in hippocampal slices. *Neuron*, 5(3): 247, 1990.

Holden, A. V. *Models of the Stochastic Activity of Neurones*. Springer-Verlag, Berlin, 1976.

Houweling, A., Doron, G., and Voigt, B. Nanostimulation: manipulation of single neuron activity by juxtacellular current injection. *J. Neurophysiol.*, 103:1696, 2010.

Houweling, A. R. and Brecht, M. Behavioural report of single neuron stimulation in somatosensory cortex. *Nature*, 451:65, 2008.

Ilin, V., Malyshev, A., Wolf, F., and Volgushev, M. Fast computations in cortical ensembles require rapid initiation of action potentials. *J Neurosci*, 33(6):2281, 2013.

Johannesma, P. I. M. Diffusion models of the stochastic activity of neurons. In Caianiello, E. R., editor, *Neural Networks*, page 116. Springer, Berlin, 1968.

Jolivet, R. and Gerstner, W. Predicting spike times of a detailed conductance-based neuron model driven by stochastic spike arrival. *J Physiol*, 98.

Jolivet, R., Kobayashi, R., Rauch, A., Naud, R., Shinomoto, S., and Gerstner, W. A benchmark test for a quantitative assessment of simple neuron models. *J. Neurosci. Meth.*, 169:417, 2008.

Joshi, A., Middleton, J. W., Anderson, C. T., Borges, K., Suter, B. A., Shepherd, G. M. G., and Tzounopoulos, T. Cell-specific activity-dependent fractionation of layer 2/3 to 5b excitatory signaling in mouse auditory cortex. *J Neurosci*, 35(7):3112, 2015.

Kistler, W. M., Gerstner, W., and v. Hemmen, J. L. Reduction of the hodgkin-huxley equations to a single-variable threshold model. *Neural Comput.*, 9(5):1015, 1997.

Knight, B. W. Relationship Between Firing Rate of a Single Neuron and Level of Activity in a Population of Neurons - Experimental Evidence for Resonant Enhancement in Population Response. *J. Gen. Physiol.*, 59:767, 1972.

Koch, C. *Biophysics of Computation - Information Processing in Single Neurons*. Oxford University Press, New York, Oxford, 1999.

Koch, C., Rapp, M., and Segev, I. A brief history of time (constants). *Cereb Cortex*, 6(2): 93, 1996.

Köndgen, H., Giesler, C., Fusi, S., Wang, X.-J., Luescher, H.-R., and Giugliano, M. The dynamical response properties of neocortical neurons to temporally modulated noisy inputs in vitro. *Cereb. Cortex*, 18:2086, 2008.

König, P., Engel, A. K., Roelfsema, P. R., and Singer, W. How precise is neuronal synchronization? *Neural Comput.*, 7:469, 1995.

L. Gomez, R. S., R. Budelli, Stiber, M., and Segundo, J. P. Pooled spike trains of correlated presynaptic inputs as realizations of cluster point processes. *Biol. Cybern.*, 92:110127, 2005.

Lánský, P. and Lánská, V. Diffusion approximation of the neuronal model with synaptic reversal potentials. *Biol. Cybern.*, 56:19, 1987.

Lansky, P. and Rodriguez, R. Two-compartment stochastic model of a neuron. *Physica D: Nonlinear Phenomena*, 132(1):267, 1999.

Lansky, P., Sanda, P., and He, J. The parameters of the stochastic leaky integrate-and-fire neuronal model. *J. Comput. Neurosci.*, 21:211, 2006.

Lapicque, L. Recherches quantitatives sur l'excitation électrique des nerfs traitée comme une polarisation. *J. Physiol. Pathol. Gen.*, 9:620, 1907.

Larkum, M. E., Zhu, J. J., and Sakmann, B. Dendritic mechanisms underlying the coupling of the dendritic with the axonal action potential initiation zone of adult rat layer 5 pyramidal neurons. *The Journal of Physiology*, 533(2):447, 2001.

Li, C. T., Poo, M., and Dan, Y. Burst spiking of a single cortical neuron modifies global brain state. *Science*, 324:643, 2009.

Lindner, B. and Schimansky-Geier, L. Transmission of noise coded versus additive signals through a neuronal ensemble. *Phys. Rev. Lett.*, 86:2934, 2001.

Lindner, B. and Voronenko, S. Lecture notes to 'neural noise and neural signals', 2005.

London, M., Roth, A., Beeren, L., Haeusser, M., and Latham, P. E. Sensitivity to perturbations in vivo implies high noise and suggests rate coding in cortex. *Nature*, 466:123, 2010.

Macke, J. H., Berens, P., Ecker, A. S., Tolias, A. S., and Bethge, M. Generating spike trains with specified correlation coefficients. *Neural Comput.*, 21:397, 2009.

Mainen, Z. F. and Sejnowski, T. J. Reliability of spike timing in neocortical neurons. *Science*, 268:1503, 1995.

Naud, R. and Gerstner, W. *Spike Timing: Mechanisms and Function*, chapter Can we Predict Every Spike?, page 65. CRC Press, 2013.

Naud, R., Bathellier, B., and Gerstner, W. Spike-timing prediction in cortical neurons with active dendrites. *Frontiers in Computational Neuroscience.J*, 8(90).

Naud, R., Marcille, N., Clopath, C., and Gerstner, W. Firing patterns in the adaptive exponential integrate-and-fire model. *Biol. Cybern.*, 99:335, 2008.

Neher, E. and Sakmann, B. Single-channel currents recorded from membrane of denervated frog muscle-fibers. *Nature*, 260:799, 1976.

Nelder, J. A. and Mead, R. A simplex method for function minimization. *The Computer Journal*, 7(4):308, 1965.

Neu, W. K. and Neu, J. Theory of electroporation. In Efimov, I., Kroll, M., and Tchou, P., editors, *Cardiac Bioelectric Therapy: Mechanisms and Practical Implications*, page 133. Springer Science+Business Media, LLC., 2009.

Ogden, D. and Stanfield, P. *Microelectrode Techniques: The Plymouth Workshop Handbook*, chapter Patch clamp techniques for single channel and whole-cell recording, page 53. Company of Biologists, 1994.

Ostermeier, A., Gawelczyk, A., and Hansen, N. Step-size adaptation based on non-local use of selection information. In Davidor, Y., Schwefel, H.-P., and Männer, R., editors, *Parallel Problem Solving from Nature — PPSN III*, volume 866 of *Lecture Notes in Computer Science*, page 189. Springer Berlin Heidelberg, 1994.

Ostojic, S., Brunel, N., and Hakim, V. How connectivity, background activity, and synaptic properties shape the cross-correlation between spike trains. *J. Neurosci.*, 29:10234, 2009.

Ostojic, S., Szapiro, G., Schwartz, E., Barbour, B., Brunel, N., and Hakim, V. Neuronal Morphology Generates High-Frequency Firing Resonance. *J. Neurosci.*, 35:7056, 2015.

Paninskia, L., Pillow, J., and Simoncelli, E. Comparing integrate-and-fire models estimated using intracellular and extracellular data. *Biophys J*, 65(66):379, 2005.

Pinault, D. A novel single-cell staining procedure performed in vivo under electrophysiological control: morpho-functional features of juxtacellularly labeled thalamic cells and other central neurons with biocytin or neurobiotin. *J Neurosci Methods*, 65(2):113, 1996.

Purves, D., editor. *Neuroscience. 3nd edition.* Sinauer Associates, 2004.

Rall, W. Branching dendritic trees and motoneuron membrane resistivity. *Exp Neurol*, 1: 491, 1959.

Rall, W. Theory of physiological properties of dendrites. *Annals of the New York Academy of Sciences*, 96(4):1071, 1962a.

Rall, W. Electrophysiology of a dendritic neuron model. *Biophys J*, 2(2):145, 1962b.

Rall, W. Time constants and electrotonic length of membrane cylinders and neurons. *Biophys J*, 9(12):1483, 1969.

Rall, W. *Core Conductor Theory and Cable Properties of Neurons*. John Wiley & Sons, Inc., 2011.

Rall, W. *Handbook of Physiology, The Nervous System, Cellular Biology of Neurons*, volume 1, chapter Core Conductor Theory and Cable Properties of Neurons, page 39. 1977.

Ricciardi, L. M. *Diffusion Processes and Related Topics on Biology*. Springer-Verlag, Berlin, 1977.

Richardson, M. J. E. Firing-rate response of linear and nonlinear integrate-and-fire neurons to modulated current-based and conductance-based synaptic drive. *Phys. Rev. E.*, 76: 021919, 2007.

Richardson, M. J. E. and Gerstner, W. Synaptic shot noise and conductance fluctuations affect the membrane voltage with equal significance. *Neural Comput*, 17(4):923, 2005.

Rieke, F., Warland, D., de Ruyter van Steveninck, R., and Bialek, W. *Spikes: Exploring the neural code*. MIT Press, Cambridge, Massachusetts, 1996.

Shadlen, M. and Newsome, W. Noise, neural codes and cortical organization. *Curr. Opin. Neurobiol.*, 4:569, 1994.

Shannon, C. E. A mathematical theory of communication. *Bell. Syst. Tech. J.*, 27:379, 1948.

Shannon, C. E. Communication in the presence of noise. *P. Ire.*, 37:10, 1949.

Silver, R. A., Traynelis, S. F., and Cull-Candy, S. G. Rapid-time-course miniature and evoked excitatory currents at cerebellar synapses in situ. *Nature*, 355(6356):163, 1992.

Softky, W. R. and Koch, C. The highly irregular firing of cortical cells is inconsistent with temporal integration of random EPSPs. *J. Neurosci.*, 13:334, 1993.

Solsona, C., Innocenti, B., and Fernández, J. M. Regulation of exocytotic fusion by cell inflation. *Biophys J*, 74(2 Pt 1):1061, 1998.

Stein, R. B. A theoretical analysis of neuronal variability. *Biophys. J.*, 5:173, 1965.

Stein, R. B., French, A. S., and Holden, A. V. The frequency response, coherence, and information capacity of two neuronal models. *Biophys. J.*, 12:295, 1972.

Strong, S. P., Koberle, R., van Steveninck, R. R. D., and Bialek, W. Entropy and information in neural spike trains. *Phys. Rev. Lett.*, 80:197, 1998.

Stuart, G. and Spruston, N. Determinants of voltage attenuation in neocortical pyramidal neuron dendrites. *Journal of Neuroscience*, 18(10):3501, 1998.

Stüttgen, M., Lourens, N., Geis, H., P.H., Tiesinga, P., and Houweling, A. Temporally precise control of single-neuron spiking by juxtacellular nanostimulation. *J. Neurophysiol.*, 117(3):1363, 2017.

Takahashi, T. The minimal inhibitory synaptic currents evoked in neonatal rat motoneurones. *J Physiol*, 450:593, 1992.

Tchumatchenko, T., Malyshev, A., Wolf, F., and Volgushev, M. Ultrafast population encoding by cortical neurons. *J. Neurosci.*, 31:12171, 2011.

Vilela, R. D. and Lindner, B. Are the input parameters of white-noise-driven integrate & fire neurons uniquely determined by rate and CV? *J. Theor. Biol.*, 257:90, 2009a.

Vilela, R. D. and Lindner, B. A comparative study of three different integrate-and-fire neurons: spontaneous activity, dynamical response, and stimulus-induced correlation. *Phys. Rev. E.*, 80:031909, 2009b.

Voroneko, S., Stannat, W., and Lindner, B. Shifting spike times or adding and deleting spikes - how different types of noise shape signal transmission in neural populations. *J. Math. Neurosci.*, 5:1, 2015.

Yu, X. L. and Lewis, E. R. Studies with spike initiators: linearization by noise allows continuous signal modulation in neural networks. *IEEE Trans Biomed Eng*, 36(1):36, 1989.

Danksagung

Ich möchte mich ausdrücklich bei meinem Betreuer Prof. Dr. Benjamin Lindner bedanken. Mit nicht enden wollendem Engagement hat er durch sein permanentes konstruktives Feedback und seine intensive Betreuung enorm dazu beigetragen, dass diese Arbeit entstehen konnte. Neben seiner fachlichen Kompetenz profitiere ich auch jetzt noch insbesondere von den Einblicken in seine Art und Weise des systematischen und wissenschaftlichen Arbeitens.

Einen weiteren großen Dank spreche ich meinen Kollegen aus der Arbeitsgruppe "Theorie komplexer Systeme und Neurophysik" aus. Durch den freundlichen und hilfsbereiten Umgang, der während der gesamten gemeinsamen Zeit geherrscht hat, ist eine angenehme und konstruktive Arbeitsatmosphäre entstanden. Besonderer Dank gilt hier Rinaldo Betkiewicz, Davide Bernardi, Sven Blankenburg, Felix Droste, Alexandra Kruscha und Sergej Voronenko, die stets ein offenes Ohr und hilfreiche Tipps für fachliche und technische Probleme hatten. Für die wunderbare Unterstützung bei allem Organisatorischen und ihre hilfsbereite Art, möchte ich mich auch ausdrücklich bei Nikola Schrenk bedanken.

Für die reibungslose und außerordentlich freundliche Zusammenarbeit mit Guy Doron, der mir bei allen biologischen Fragen stets hilfsbereit und kompetent zur Seite stand, bin ich ebenfalls sehr dankbar und zolle ihm dafür ganz besonderen Respekt. Durch unsere gemeinsame Arbeit konnte ich über meinen Tellerrand hinaus blicken und funktionierendes interdisziplinäres Arbeiten erfahren. An dieser Stelle sollen auch die unfreiwilligen Helfer, mit denen experimentell die Daten erhoben wurden, Erwähnung finden, da sie den größten Teil dazu beigetragen haben, diese Arbeit zu ermöglichen.

Eine tiefgreifende Dankbarkeit empfinde ich für meine Eltern Harry und Jutta sowie für meinen Bruder Niels. Von ihnen habe ich stets Verständnis erfahren und durch ihre permanente Unterstützung gelernt und vorgelebt bekommen, aus eigenem Antrieb heraus eigene Wege zu gehen.

Den vielen lieben Menschen aus meinem privatem Umfeld möchte ich dafür danken, dass sie mir stets motivierend beiseitestanden und mir die Möglichkeit gegeben, haben außerhalb der Arbeit die nötige Kraft zu tanken. Ein ganz außerordentlicher Dank gilt hierbei Isabel Heck, die mit ihrer liebevollen Unterstützung einen Raum geschaffen hat, der die Basis gebildet hat, um dieses Projekt zu bewältigen.

Selbstständigkeitserklärung

Ich erkläre, dass ich die vorliegende Arbeit selbstständig und nur unter Verwendung der angegebenen Literaur und Hilfsmittel angefertigt habe.

Berlin, den 22.08.2017 Jens Doose